

Spring 5-1-2015

Mechanochemical Investigation of a Glassy Epoxy-Amine Thermoset Subjected to Fatigue

Stephen Finley Foster
University of Southern Mississippi

Follow this and additional works at: <https://aquila.usm.edu/dissertations>

 Part of the [Polymer Chemistry Commons](#)

Recommended Citation

Foster, Stephen Finley, "Mechanochemical Investigation of a Glassy Epoxy-Amine Thermoset Subjected to Fatigue" (2015). *Dissertations*. 50.

<https://aquila.usm.edu/dissertations/50>

This Dissertation is brought to you for free and open access by The Aquila Digital Community. It has been accepted for inclusion in Dissertations by an authorized administrator of The Aquila Digital Community. For more information, please contact Joshua.Cromwell@usm.edu.

The University of Southern Mississippi

MECHANOCHEMICAL INVESTIGATION OF A GLASSY EPOXY-AMINE
THERMOSET SUBJECTED TO FATIGUE

by

Stephen Finley Foster

Abstract of a Dissertation
Submitted to the Graduate School
of The University of Southern Mississippi
in Partial Fulfillment of the Requirements
for the Degree of Doctor of Philosophy

May 2015

ABSTRACT

MECHANOCHEMICAL INVESTIGATION OF A GLASSY EPOXY-AMINE THERMOSET SUBJECTED TO FATIGUE

by Stephen Finley Foster

May 2015

Covalent bonds in organic molecules can be produced, altered, and broken through various sources of energy and processes. These include photochemical, thermochemical, chemical, and mechanochemical processes. Polymeric materials derive their physical properties from the time scale of motion, summation of intermolecular forces, and number of chain entanglements and crosslinks. Glassy thermoset polymers experience mechanical fatigue during dynamic stress loading and properties diminish with inevitable material failure at stress levels below the ultimate tensile strength (UTS). Damage modeling has been successful in predicting the number of cycles required to induce failure in a specimen due to stress. However, it does not directly provide an explanation of the origin of fatigue in polymers. It is hypothesized herein that mechanical failure at stress levels below the ultimate strength property is due to the accumulation of mechanically induced homolytic chain scission events throughout the glassy thermoset network. The goal of this research will be to quantify homolytic chain scission events with fatigue cycles with the ultimate goal of correlating mechanical property loss with degradation of covalent network structure.

To accomplish this goal, stable free nitroxyl radicals were incorporated into an epoxy-amine matrix to detect homolytic chain scission resulting from fatigue. Chapter II discusses a successful synthesis and characterization of the nitroxyl radical molecule, a

product of 4-hydroxy-2,2,5,5-tetramethylpiperdin-1-yl-oxyl (TEMPO) and isophorone diisocyanate designated as BT-IPDI. In Chapter III, the epoxy-amine reaction was determined to be unaffected by incorporation of up to 5 wt% of BT-IPDI. Although 50% UTS fatigue studies produced property degradation and fatigue failure as shown in Chapter IV, analysis of BT-IPDI through EPR did not detect homolytic chain scission. Chapter V reveals that mechano-radicals were produced from cryo-grinding the glassy epoxy-amine thermoset, and although the mechano-radicals reacted through recombination at elevated temperatures, the reaction between mechano-radicals and the BT-IPDI was not detected to occur within the glassy state.

During mechanical testing, observations of unusual tensile yield behavior were coupled with production of atypical fracture surfaces. In Chapter VI, physical aging was used as an investigative tool to verify that viscous deformation (plastic flow) was required to produce the atypical fracture surfaces. Atomic force microscopy and scanning electron microscopy of the fracture surface both revealed a tendril nodule morphology. It is our hypothesis that this morphology produces the unusual mechanical behavior. In Chapter VII, NIR, AFM, and SEM were used to measure the conversion and morphology of the epoxy-amine thermoset correlated with mechanical properties. The thermal cure profile of the epoxy-amine thermoset affects the size and formation of the nodular nanostructure. Eliminating vitrification during thermoset polymerization forms a more continuous phase, reduction in size of the nodules, and eliminates the capacity of the material to yield in plastic flow. Specific findings of this research reveal that morphology control through thermal cure design may indicate a route in which thermoplastic type failure mechanisms can be incorporated into glassy epoxy thermosets.

COPYRIGHT BY
STEPHEN FINLEY FOSTER
2015

The University of Southern Mississippi

MECHANOCHEMICAL INVESTIGATION OF A GLASSY EPOXY-AMINE
THERMOSET SUBJECTED TO FATIGUE

by

Stephen Finley Foster

A Dissertation
Submitted to the Graduate School
of The University of Southern Mississippi
in Partial Fulfillment of the Requirements
for the Degree of Doctor of Philosophy

Approved:

Dr. James Rawlins
Committee Chair

Dr. Jeffrey Wiggins

Dr. Sergei Nazarenko

Dr. William Jarrett

Dr. Derek Patton

Dr. Karen Coats
Dean of the Graduate School

May 2015

ACKNOWLEDGMENTS

I would like to acknowledge everyone that has had such a significant impact in my life for me to reach this point. My parents, in my opinion, performed the most miraculous achievement; a child diagnosed with ADD gets his Ph.D. (eventually). It has taken a lot of time to get to this point, which I blame on distractions. In all seriousness, my parents are of excellent character, and so is my wife, and if not for them, well, who knows?

Dr. James Rawlins is my graduate advisor, and on several occasions has not let me give up when I thought that I should. He has kept his door open for me probably even when he should not have done so. I would also like to thank the additional members of my committee Dr. Jeffrey Wiggins, Dr. Sergei Nazarenko, Dr. Derek Patton and of course, Dr. William Jarrett. I want to thank each of my committee members for graciously volunteering their labs and equipment for necessary experiments, specifically ARAMIS, PVT and AFM work.

A former member of my committee, Dr. Alvin A. Holder, has accepted a research position at Old Dominion University, and while currently not on my committee, his insights and teaching on EPR were invaluable. Dr. Robert Lochhead took a chance on a young man with an undergrad Polymer Science B.S. degree, who was delivering pizza as a career choice, to manage his academic laboratory. After two years of full time research, I decided that attending and completing graduate school was a possibility and enrolled at USM in the fall of 2008.

I would also like to acknowledge special graduate students that have helped me in my Ph.D. journey. Firstly, Brandon Achord, for without his help and teaching, I quite

possibly could still be in undergrad. Also, without his “help and teaching”, I would not have been responsible for maintaining and fixing the lab GPC. So, double edge sword there. David Krzminski and Nadine Lippa, all though they may think of themselves from time to time as engineers (not that there is anything wrong with that), they are both wonderful scientists, and outstanding writers and presenters.

I would finally like to acknowledge my former undergrad worker and future Louisiana State University Ph.D. graduate, Kylee Fazende. Countless hours spent making samples and designing injection molding equipment cannot be overlooked. Her work and help were invaluable to this research. Finally, to all of my group members and graduate colleagues, thank you for your time and effort. There are literally too many of you to list.

TABLE OF CONTENTS

ABSTRACT.....	ii
ACKNOWLEDGMENTS	iv
LIST OF TABLES	ix
LIST OF ILLUSTRATIONS	xi
LIST OF EQUATIONS	xix
LIST OF SCHEMES.....	xviii
CHAPTER	
I. INTRODUCTION	1
Research Motives	
What is Fatigue?	
Fatigue Behaviour of Glassy Epoxy Thermosets	
Mechanically Induced Chain Scission	
Characterization of Mechanical Activation for Covalent Bonds	
Considerations on Bond Strengths - Theoretical vs. Actual	
How EPR Works	
Nitroxyl Radicals for Homolytic Chain Scission Detection	
Hypothesis	
Objectives	
Challenges	
Concluding Remarks	
References	
II. MATERIALS AND EXPERIMENTAL DETAILS.....	20
Introduction	
Epoxy-Amine Thermoset Materials	
Synthesis of Stable Free Nitroxyl Radical Probes	
Characterization of Bis-TEMPO-IPDI	
BT-IPDI Functional Equivalent Weight Titration	
Pressure-Volume-Temperature High Pressure Dilatometry	
References	
III. CHEMO-RHEOLOGICAL CHARACTERIZATION OF EMBEDDED REACTIVE MATERIALS	37

	Introduction	
	Materials	
	Synthesis	
	Sample Preparation	
	Results	
	Conclusions	
	References	
IV.	FATIGUE OF A GLASSY EPOXY THERMOSET WITH HOMOLYTIC CHAIN SCISSION PROBES	51
	Introduction	
	Materials	
	Nitroxyl Loading Justification	
	Sample Preparation	
	Experimental	
	EPR Spectra of Nitroxyl Radicals	
	Experimental Design of 50% UTS Experiments	
	50% UTS Fatigue Trials Results	
	50% UTS Discussion	
	50% UTS Conclusions	
	Experimental Design of 30% UTS Experiments	
	30% UTS Fatigue Trials Results	
	30% UTS Discussion	
	Conclusions	
	References	
V.	CRYO-GRINDING OF EPOXY-AMINE THERMOSETS	103
	Introduction	
	Experimental	
	Results	
	Conclusions	
	References	
VI.	INVESTIGATION OF TENSILE PLASTIC FLOW AND FRACTURE MORPHOLOGY OF A GLASSY EPOXY-AMINE THERMOSET	119
	Introduction	
	Experimental	
	Results	
	Conclusions	
	References	

VII.	CHEMORHEOLOGY INVESTIGATION OF A GLASSY EPOXY THERMOSET ON TENSILE PLASTIC FLOW AND FRACTURE MORPHOLOGY	137
	Introduction	
	Experimental	
	Results and Discussion	
	Controlling Morphology Through Thermal Cure Staging	
	Conclusions	
	References	
VIII.	SUMMARY	173
	Overview	
	Summary of Results	
	Future Research Considerations	
	APPENDIXES	182

LIST OF TABLES

Table

1. PVT Experimental Data and Calculated V_{occ} , V_f , and Bulk Modulus33

2. Calculated Percent Fractional Free Volume at 300 K34

3. Molar Absorptivity Values41

4. Average Pre-vitrification Rates of Epoxide Conversion for DGEBA-2-methyl-1,5-diaminopentane at 30 °C.....46

5. G'/G'' Crossover Time Points in Dynamic Rheology Data at 30 °C.....47

6. G' Plateau Time Points in Dynamic Rheology Data at 30 °C47

7. Mechanical Properties of 50% UTS Control60

8. Trial One Residual Strength Properties at 50% UTS 10,000 Cycles.....63

9. Trial Two Residual Strength Properties at 50% UTS 10,000 Cycles65

10. Trial Three Residual Strength Properties at 50% UTS 10,000 Cycles67

11. Trial Four Residual Strength Properties at 50% UTS 10,000 Cycles.....69

12. Mechanical Properties of 30% UTS Controls.....74

13. Trial One Residual Strength Properties at 30% UTS 1,000,000 Cycles.....79

14. Trial Two Residual Strength Properties at 30% UTS 1,000,000 Cycles82

15. Trial Three Residual Strength Properties at 30% UTS 1,000,000 Cycles85

16. Trial Four Residual Strength Properties at 30% UTS 1,000,000 Cycles.....88

17. Trial Five Residual Strength Properties at 30% UTS 1,000,000 Cycles91

18.	Trial Six Residual Strength Properties at 30% UTS 1,000,000 Cycles	94
19.	Cryo-ground Particle Size Analysis.....	115
20.	DMA Mechanical Thermal Transitions for Figure 85	127
21.	Molar Absorptivities	147
22.	NIR Epoxide Conversion with Thermal Cure Profiles and Measured T_g	152
23.	Thermal Cure Profiles and Mechanical Properties	162

LIST OF ILLUSTRATIONS

Figure

1.	Modulus of an Epoxy Thermoset During Strain-Controlled Fully Reversed Uniaxial Fatigue Tests	4
2.	Hysteresis Loops of the Strain-Range Controlled Fully Reversed Uniaxial Fatigue Tests	5
3.	Concentration of Free Radicals and Uniaxial Stress in Step-Temperature Test as a Function of Temperature and Time for Polycaprolactam Fibers.....	8
4.	Brittle Strength vs. Number of Backbone Bonds.....	10
5.	Illustrating the Zeeman Effect on the Spin States of Paramagnetic Electrons	11
6.	Stable Free Radical Nitroxide Molecules	12
7.	Illustration Depicting Chain Scission Resulting from Force	13
8.	GPC Spectrum of BT-IPDI Product	23
9.	Illustration of BT-IPDI Titration Serial Dilution Experiment	25
10.	Integral Area of EPR Signal Versus Calculated Concentration Of Nitroxyl Radicals Assuming 100% Conversion.....	26
11.	Integral Area of EPR Signal Versus Functional Ratio Predicted Concentration of Nitroxyl Radicals Assuming 100% Conversion	26
12.	Mathematical Simulations Of Various Starting Concentrations of BT-IPDI for the Volumetric Titration Experiment.....	27
13.	Thermal Cycle to Remove Aging Prior to PVT Analysis.....	28
14.	PVT Of DGEBA – 2-Methyl-1,5-Diaminopentane at Various Temperatures and Pressures	29

15.	Fitting SS-EOS to PVT of DGEBA – 2-methyl-1,5-diaminopentane	31
16.	Specific Volume (V), Specific Occupied Volume (V_{occ}), and Specific Free Volume (V_f) Calculated from PVT.....	32
17.	Bulk Modulus Versus Temperature of DGEBA - 2-Methyl-1,5-Diaminopentane	33
18.	Blocked Isocyanate Additive Structures with Core Comprising Isophorone Diisocyanate.....	39
19.	Thermoset Epoxy-Amine Comprised of (A) DGEBA and (B) 2-methyl-1,5-diaminopentane	39
20.	Wavenumber Regions Monitored for Primary+Secondary Amine, Primary Amine, and Epoxide Absorption Bands	41
21.	Chemorheological Characterization of DGEBA and 2-methyl-1,5-diaminopentane Epoxy-Amine Reaction at 30 °C.....	44
22.	Chemorheological Characterization of DGEBA and 2-methyl-1,5-diaminopentane Epoxy-Amine Reaction in the Presence Of 5 Wt% Bis-TEMPO-IPDI at 30 °C ..	45
23.	Chemorheological Characterization of DGEBA and 2-methyl-1,5-diaminopentane Epoxy-Amine Reaction in the Presence of 10 Wt% E-Cap-B-IPDI At 30 °C	45
24.	Chemorheological Characterization of DGEBA and 2-methyl-1,5-diaminopentane Epoxy-Amine Reaction in the Presence of 10 Wt% NMA-B-IPDI at 30 °C	46
25.	Illustration Depicting Chain Scission Resulting from Force	52
26.	Reaction Injection Molding Setup for Sample Casting	54
27.	Sample Injection Depiction and Mold Layout.....	55
28.	Thermal Annealing Temperature Ramps for Samples.....	56
29.	Examples of EPR Spectra of Nitroxyl Radicals in Solution and Solid State	59
30.	50% UTS Experimental Design Depiction.....	61

31.	Trial One EPR Intensity Measurements for Control and Fatigue Conditions Before and After Treatment	62
32.	Trial Two EPR Intensity Measurements for Control and Fatigue Conditions Before and After Treatment	64
33.	Trial Three EPR Intensity Measurements for Control and Fatigue Conditions Before and After Treatment	66
34.	Trial Four EPR Intensity Measurements for Control and Fatigue Conditions Before and After Treatment	68
35.	EPR Intensity of Control Samples from Trials 1-4 Before and After Fatigue Time Allotment Normalized to Q-Value.....	70
36.	EPR Intensity of Fatigue Samples from Trials 1-4 Before and After Fatigue Treatment Normalized to Weight and Q-Value.....	70
37.	Average EPR Intensity of Control and Fatigue Samples from Trials 1-4 Before and After Fatigue Treatment Normalized to Weight and Q-Value.....	71
38.	Δ EPR Intensity Values of Control and Fatigue Samples from Trials 1-4 Before and After Fatigue Treatment Normalized to Weight and Q-Value.....	72
39.	30% UTS Experimental Design Depiction	75
40.	Trial One EPR Intensity Measurements for Control and Fatigue Conditions Before and After Treatment	77
41.	Trial One NIR Spectra of Fatigue Sample Before and After Treatment	77
42.	Trial One ATR-FTIR Spectra of Fatigue Sample Before and After Treatment	78
43.	Stress-Strain Curves of Trial One	79
44.	Trial Two EPR Intensity Measurements for Control and Fatigue Conditions Before and After Treatment	80
45.	Trial Two NIR Spectra of Fatigue Sample Before and After Treatment.....	80
46.	Trial Two ATR-FTIR Spectra of Fatigue Sample Before and After Treatment....	81

47.	Stress-Strain Curves of Trial Two	82
48.	Trial Three EPR Intensity Measurements for Control and Fatigue Conditions Before and After Treatment	83
49.	Trial Three NIR Spectra of Fatigue Sample Before and After Treatment.....	83
50.	Trial Three ATR-FTIR Spectra of Fatigue Sample Before and After Treatment..	84
51.	Stress-Strain Curves of Trial Three	85
52.	Trial Four EPR Intensity Measurements for Control and Fatigue Conditions Before and After Treatment	86
53.	Trial Four NIR Spectra of Fatigue Sample Before and After Treatment	86
54.	Trial Four ATR-FTIR Spectra of Fatigue Sample Before and After Treatment ...	87
55.	Stress-Strain Curves of Trial Four	88
56.	Trial Five EPR Intensity Measurements for Control and Fatigue Conditions Before and After Treatment	89
57.	Trial Five NIR Spectra of Fatigue Sample Before and After Treatment.....	89
58.	Trial Five ATR-FTIR Spectra of Fatigue Sample Before and After Treatment....	90
59.	Stress-Strain Curves of Trial Five.....	91
60.	Trial Six EPR Intensity Measurements for Control and Fatigue Conditions Before and After Treatment	92
61.	Trial Six NIR Spectra of Fatigue Sample Before and After Treatment.....	92
62.	Trial Six ATR-FTIR Spectra of Fatigue Sample Before and After Treatment.....	93
63.	Stress-Strain Curves of Trial Six	94
64.	EPR Intensity Values of Control Samples from Trials 1-6 Before and After Time Allotment Normalized to Q-Value.....	95

65.	EPR Intensity Values of Fatigue Samples from Trials 1-6 Before and After Fatigue Treatment Normalized to Q-Value	96
66.	EPR Intensity Average Values of Control and Fatigue Samples from Trials 1-6 Before and After Fatigue Treatment Normalized to Q-Value	98
67.	Δ EPR Intensity Normalized to Q-Value for Control and Fatigue Conditions Post Treatment	99
68.	Cryo-Grinding Experimental Procedure	106
69.	VT-EPR Spectra of Cryo-Ground SC-15	107
70.	SC-15 Cryo-Ground EPR Integral Areas Compared to Boltzmann Statistics Calculation for Decreasing Differences in Quantum States with Increasing Temperature	109
71.	VT-EPR of Cryo-Ground SC-15 with 0.1 Wt% BT-IPDI.....	110
72.	VT-EPR of SC-15 / 0.1 Wt% BT-IPDI Cryo-Ground EPR Integral Areas Compared to Boltzmann Statistics Calculation for Decreasing Differences in Quantum States with Increasing Temperature.....	110
73.	VT-EPR Spectra of Cryo-Ground DGEBA and 2-methyl-1,5-diaminopentane .	111
74.	VT-EPR: DGEBA and 2-methyl-1,5-diaminopentane Cryo-Ground EPR Integral Areas Compared to Boltzmann Statistics Calculation for Decreasing Differences in Quantum States with Increasing Temperature.....	111
75.	EPR Overlay of the Nitroxyl Radical and Mechano-Radical Spectrums	113
76.	Modulated VT-EPR for Cryo-Ground DGEBA and 2-Methyl-1,5-Diaminopentane Containing 0.005 Wt% BT-IPDI.....	114
77.	Tensile Stress-Strain Curve of DGEBA-2-Methyl-1,5-Diaminopentane Type V Dogbones	119
78.	Stress-Strain Terminology	120
79.	Mirror-Mist-Hackle Topography	121

80.	Physical Aging Resulting in Simultaneous Decreases in Specific Volume and Excess Enthalpy	122
81.	DSC Isothermal Scan of DGEBA and 2-methyl-1,5-diaminopentane Cure Temperatures Followed by Temperature Sweep to 180 °C	124
82.	TGA Thermal Sweep of DGEBA-2-methyl-1,5-diaminopentane	125
83.	First Heating Cycles of Aged Samples Showing Increasing Enthalpic Recovery with Aging Time	126
84.	Second Heating Cycles of Aged Samples Revealing Increasing T_g from Physical Aging Treatment	127
85.	DMA Thermal Sweeps of Non-Aged and Aged-10 Days Samples.....	128
86.	Tensile Stress-Strain Curves of Type V ASTM D638 Dogbones	130
87.	Non-Aged Fracture Surfaces Correlated to the Yield Region in Figure 86.....	130
88.	Non-Aged Fracture Surfaces Correlated to the Plastic Flow Region in Figure 86	130
89.	Aged-10 Days Fracture Surfaces Correlated to the Yield Region in Figure 86 ..	131
90.	AFM Images of DGEBA – 2-methyl-1,5-diaminopentane Resulting from Tensile Fracture	134
91.	SEM Images of DGEBA / 2-methyl-1,5-diaminopentane Resulting from Tensile Fracture	134
92.	Functional Group Concentrations Measured by Transmission NIR of the DGEBA - 2-Methyl-1,5-Diaminopentane Epoxy-Amine Reaction	146
93.	Rheology Profile of DGEBA - 2 Methyl-1,5-Diaminopentane Epoxy-Amine Reaction	148
94.	Dynamic Rheology Thermal Sweep from High Temperature to Low Temperature of the Same Experiment as Figure 93	149
95.	Storage Modulus vs. Temperature of Various Cure Profiles	151

96.	Tan δ vs. Temperature of Various Cure Profiles	151
97.	Weight Fraction of Finite Species Calculated by Flory's Statistical Equations ..	154
98.	AFM Images of DGEBA – 2-methyl-1,5-diaminopentane Resulting from Cure Profiles α and β with Conversion Values Listed.....	155
99.	AFM Images of DGEBA – 2-methyl-1,5-diaminopentane Resulting from Cure Profiles γ and δ with Conversion Values Listed	156
100.	SEM Images of DGEBA / 2-methyl-1,5-diaminopentane Resulting from Cure Profiles α and β	158
101.	SEM Images of DGEBA / 2 Methyl-1,5-Diaminopentane Resulting from Cure Profiles γ and δ	158
102.	Tensile Stress-Strain Curves of DGEBA – 2-methyl-1,5-diaminopentane at Various Stages of Cure	159
103.	Tensile Stress-Strain Curves of DGEBA – 2-methyl-1,5-diaminopentane at Various Stages of Cure for Digital Image Correlation	160
104.	Strain Map of Sample Surface Calculated Through Digital Image Correlation..	161
105.	Microscopy Images of Pull-To-Break Fracture Surfaces of Type V ASTM D-638 Dogbone Samples	163
106.	Depiction of Isothermal Phase Transition from Liquid State to Vitrified Glass for a Step-Growth Thermoset	165
107.	Rheology Profile of the DGEBA – 2-methyl-1,5-diaminopentane Epoxy-Amine Reaction	165
108.	Tensile Stress-Strain Curves of DGEBA – 2-methyl-1,5-diaminopentane with Staged Thermal Cure (NV) to Avoid Vitrification During Polymerization	166
109.	AFM Images of DGEBA – 2-methyl-1,5-diaminopentane Resulting from Non-Vitrification Cure Profile, Left Column (Height Image), Right Column (Phase Image)	167
110.	Elastically Active Nitroxyl Probe Created from 4-Hydroxy-TEMPO	180

LIST OF SCHEMES

Scheme

1. Reaction of (A) DGEBA and (B) 2-methyl-1,5-diaminopentane to Form (C) Crosslinked Epoxy-Amine Network.....21
2. Reaction of (A) 4-Hydroxy TEMPO and (B) Isophorone Diisocyanate to Form (C) Bis-TEMPO IPDI (BT-IPDI)22
3. Radical Photoinitiator 2,4,6-Trimethylbenzoyldiphenylphosphine Oxide (TPO) Disassociation Following Exposure to 390 Nm25
4. Reaction of Radical Photoinitiator 2,4,6-Trimethylbenzoyldiphenylphosphine Oxide (TPO) with TEMPO Nitroxyl Radicals.....25
5. Denisov Cycle Demonstrating Major Products of the Reaction of Alkyl, Alkoxy, and Peroxyl Radicals with TEMPO97

LIST OF EQUATIONS

Equation	
1.	Helmholtz Free Energy, F30
2.	Simha-Somcynski Equation of State (SS-EOS)30
3.	Reduced Parameters \tilde{P} , \tilde{T} , and \tilde{V}30
4.	Reduced SS-EOS at Zero Pressure30
5.	Natural Logarithm of Reduced SS-EOS with A_0 and A_1 Values30
6.	Simha-Somcynski Equation of State (SS-EOS) at Zero Pressure31
7.	Occupied Volume (V_{occ}) Calculated from Specific Volume (V) and Fractional Occupied Lattice Site (O)31
8.	Specific Volume (V) as a Sum of Occupied Volume (V_{occ}) and Free Volume (V_f)32
9.	Stress Ratio Equation.....56
10.	Number of Hyperfine Splittings Predicted by the Hartman Equation57
11.	Boltzmann Statistics Equation Calculating the Difference in Quantum States as a Function of Temperature.....108
12.	Crosslink Density Calculation Using Storage Modulus and Density153
13.	Ratio (P) of Non-Branched Units to the Total Units of the Reaction Mixture....153
14.	The Critical Branching Coefficient α as a Function of Conversion (P) and the Ratio of Non-Branched Units to the Total Units of the Mixture (P)153
15.	Weight Fraction of Finite Species.....153

CHAPTER I

INTRODUCTION

Research Motives

Composite materials represent an increasing percentage of structural materials as suitable successors to high strength aluminum within the aerospace industry. For structural materials, criteria such as stiffness, weight, chemical resistance, thermal envelope, and fatigue life performance are highly important. For composite applications, epoxy-amine matrices are an attractive option because they are relatively cheap to manufacture and possess properties such as high modulus, good adhesion, good reactivity, good chemical resistance, and sufficiently high glass transition temperatures (T_g). These characteristics make epoxy-amine thermosets popular as matrix materials for fiber reinforcement composites in applications that require a high strength to weight ratio. Global consumption of epoxy resin materials had an estimated value of USD \$18.6 billion in 2013 and is forecast to rise to USD \$25.8 billion by 2018 and USD \$33.6 billion by 2022 at an annual growth rate of 6.8%, primarily in adhesive and composite markets.¹

While the most common application for epoxy-amine thermosets is wind turbine blades, they are also being used now as primary structures within commercial aircraft such as the Boeing 787 where they offer great possibilities for reducing the aircraft weight. Technology improvements in composite manufacture have led to carbon fiber reinforced polymers (CFRPs) being used to the extent of 50% by weight in current commercial Boeing 787s.² This figure will continue to rise as the benefits of mechanical performance to weight ratio of fiber reinforced composites enable greater fuel savings for

commercial aircraft. Private aircraft manufacturers have pushed for higher percentage weight of composites being able to manufacture even 100% of the airframe from composite materials.^{3,4}

What is Fatigue?

Within structural load applications, fatigue is an important criterion in designing parts for end use performance. Brittle materials, such as epoxies, eventually fail under repetitive stresses with little to no warning.⁵ Current non-critical industry methodology is to over engineer a part with a safety factor between 3 to 5.⁶ Safety factor, defined as the ultimate property divided by the expected design load, is the degree to which a part has been over engineered relative to the expected stress load. For spaceflight systems, NASA directs that design components with respect to CFRP be engineered to safety factors of 1.5 to 2.0 for non-pressure vessel applications.⁷ As weight becomes a more critical issue, the safety factors are lowered (compared to other industries) to allow for lighter components. With lower safety factors, the components become increasingly more scrutinized to ensure consistency of manufacture and accurate predictions of expected load. Regarding fatigue and creep, NASA demands that spaceflight structures meet at minimum a service life factor of 4, i.e., all parts and components must be able to withstand four times the number of expected stress cycles of intended use.⁷ In practice, fatigue causes degradation and failure of polymeric materials when cycled at or above approximately 30% of the UTS.⁸ Polymer failure has been measured at approximately 20% of the UTS. However, the number of cycles required to reach failure becomes experimentally inconvenient. In some cases, the 10^7 - 10^9 cycles needed to collect a single

data point can exceed one year of testing at appropriate frequency ranges to avoid self-heating or other anomalies during testing.^{9,10}

Manufacturers and engineers are fully capable of designing structures with regards to the anticipated loads so that sufficient safety and lifetime performance of the structure is met. Current damage models exist for a wide variety of applications. A simple model would be the Palmgren-Miner, which assumes a linear correlation of damage (cycle number) with remaining life (cycle to failure) at a constant sinusoidal amplitude of stress or strain. There are more complex stress waveforms that can be used, varying the waveform from sinusoidal to square or triangle. These models enable manufacturers to produce a part which can meet the in use performance requirements demanded by application. These predictive models are excellent at meeting the performance needs for aerospace, automobile, and engineering structures. However, the models are unable to provide the understanding of why the material fails under repetitive stress and lack the capability to provide data for intelligent design of future materials.

Fatigue Behaviour of Glassy Epoxy Thermosets

This research project focuses solely on investigating an epoxy matrix when subjected to fatigue. The literature is sparse in examples in which the epoxy thermoset alone has been subject to fatigue testing, although there are plenty of studies discussing thermoset composites reinforced with carbon fiber, graphite/graphene, rubber toughened, and silicate dispersions. Xia published an in-depth study of epoxy thermoset systems via mechanical characterization and modelling that focused on multiple cyclic fatigue approaches such as biaxial,¹¹ uniaxial tension/compression,^{12,13} and cyclic shear loading¹⁴ as well as mean stress/strain effects¹⁵ and the accumulation of stress/strain throughout

fatigue tests.¹⁶ These studies measured deterioration of the *in situ* mechanical properties throughout the cyclic testing.

Figure 1 depicts the *in situ* modulus of a crosslinked epoxy network subject to uniaxial tension/compression strain-controlled cycles of various strains. Fatigue cycling at low strain causes the *in situ* modulus to decrease and then plateau into an induction period in which there is little to no change in value until catastrophic failure.¹² Increasing strain aggravates this behaviour causing increasing property loss until failure. The loss of modulus cannot solely be the cause of failure; multiple strain experiments do not diminish in modulus to the same numerical value prior to failure.

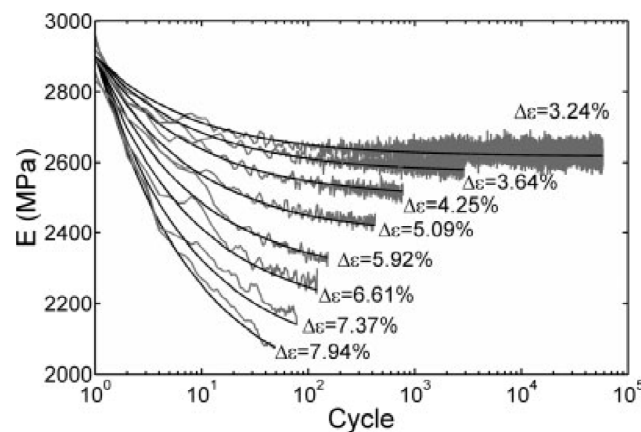


Figure 1. Modulus of an epoxy thermoset during strain-controlled fully reversed uniaxial fatigue tests. Fitted lines are simulations. An experimental study of uniaxial fatigue behavior of an epoxy resin by a new noncontact real-time strain measurement and control system, by G. Tao and Z. Xia, 2007, *Polymer Engineering & Science*, volume 47, p. 784. Reprinted with permission from the publisher.¹²

Xia measured *in situ* changes in properties, viscous and elastic components, and energy absorption characteristics but did not propose a causality mechanism relating to the structure, either molecular or macroscopic.¹¹⁻¹⁶ Xia developed accurate fatigue models to predict the lifetime of the pure epoxy, but a hypothesis to the origin of the

diminishment of properties was not posited. Of the models used to predict lifetime, the author noted that strain-energy based approaches were the most accurate and consistent.

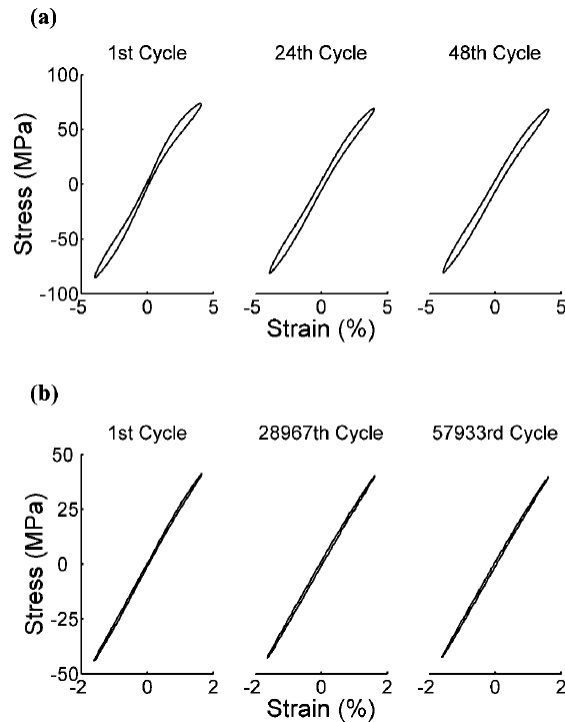


Figure 2. Hysteresis loops of the strain-range controlled fully reversed uniaxial fatigue tests. (a) Hysteresis loops of the first cycle, the mid-life cycle, and the last cycle from the test with the highest strain range level. (b) Hysteresis loops of the first cycle, the mid-life cycle, and the last cycle from the test with the lowest strain range level. An experimental study of uniaxial fatigue behavior of an epoxy resin by a new noncontact real-time strain measurement and control system, by G. Tao and Z. Xia, 2007, *Polymer Engineering & Science*, volume 47, p. 783. Reprinted with permission from the publisher.¹²

Using a non-contact strain gauge, Xia measured full hysteresis loops of the material, observing increases in the area of the hysteresis loop with fatigue cycle for large strains and minimal increases for fatigue cycles at low strains (Figure 2).¹² Decreases in the *in situ* modulus and the anelastic range were observed with increasing fatigue cycles.¹² We hypothesize that the change in properties and eventual failure of the material result from accumulated chain scission events caused by mechanical force.

Mechanically Induced Chain Scission

Mechanically induced chain scission was first reported by researchers in the 1930s who measured and characterized viscosity decreases in polymer solutions that were repeatedly subjected to high shear rates.¹⁷⁻²⁰ Mechanically induced chain scission has also been observed under certain ultrasonic frequencies and intensities.^{17,21-24} Statistically, the force vectors (sonication, high shear rates, mastication, shear-strain yield) diverge at the center of the polymer chain causing the center to be the most probable location of bond scission in solution and solid state.^{9,17,18,25,26} As the rate of strain or shear increases, the scission points for polymer chains become increasingly random.^{17,18}

Sperling *et al.* investigated anionically synthesized polystyrene latexes and quantified the number of chain scissions resulting from grinding based on time dependency and number of entanglements.²⁷ Using a strain-controlled dental burr, Sperling was able to quantify the mechanical energy of fracture and correlate it to the fracture surface. Analyzing the ground powder through gel permeation chromatography (GPC), the authors noted that only ~ 10% of the chains fractured through chain scission, and the resulting energy was dissipated through chain pull out and crazing mechanisms. Sperling extended his technique for evaluating linear polystyrene to measure changes in crosslinked polystyrene and polymethyl methacrylate. The experiments were performed by digesting the ester crosslinks after grinding and determining the concentration of chain scissions, molecular weight changes, and energy of fracture per scission event.²⁸

Backman and Devries constructed a microtome capable of cutting thin slices of polymer under nitrogen atmosphere at various temperatures, rapidly quenching the

samples in liquid nitrogen and quantifying the radical concentration per fracture area.²⁹ In polyethylene samples, chain scission in the presence of oxygen was initiated via cyclic stress at 80% UTS (35 MPa at 0.01 and 0.002 Hz) and evaluated by monitoring the increase in aldehyde functionality through radical scavenging of oxygen molecules.^{30,31} The by-products of grinding and stress-strain fracture of crosslinked epoxy samples showed the formation of radicals and unique chemical species analyzed by electron paramagnetic resonance (EPR) and matrix assisted laser deionization-time of flight (MALDI-TOF), respectively.^{32,33}

Profluorescent nitroxyl (PFN) radicals are fluorescing molecules selective to alkyl carbon centered radicals.³⁴ Blinco *et al.* incorporated 0.05 wt% PFN (Appendix Figure 1) into crosslinked isocyanate coatings and then fractured the surface via known impact energy from falling weights. After heating the sample to approximately 150 °C, the damaged area visually fluoresced under examination with a black light but was not further characterized for spatial or intensity quantification.^{35,36}

Polymer chains have been shown to mechanically fracture in the solid state by both homolytic and heterolytic chain scission.^{29,37-41} In the case of homolytic scission, the formation of conjugated end-groups from disproportionation leads to branching and crosslinking as radical migration from primary end-groups favor secondary and tertiary carbons. Disproportionation or radical trapping results in molecular weight reduction while other radical abstraction processes lead to linear, branched, or crosslinked polymers.¹⁷

Characterization of Mechanical Activation for Covalent Bonds

Electron paramagnetic resonance (EPR) techniques have been employed to monitor radical formation in grinding polymers as well as *in situ* for polymer fibers during stepwise strain events.⁹ Zhurkov *et al.* proposed that both mechanical stress and temperature add an energy contribution to the Arrhenius relationship to overcome the energy of activation barrier.⁹ Based on this concept, a pivotal experiment (Figure 3) was performed by Becht, Johnsen, and Klinkenberg. Caprolactam-based polyamide fibers were cooled to 200 K, strained to 14.2%, and the temperature was increased in stepwise increments while monitoring radical formation *in situ* as the contribution of mechanical and thermal energy both exceeded E_a (188 kJ/mol) for bond disassociation.⁹

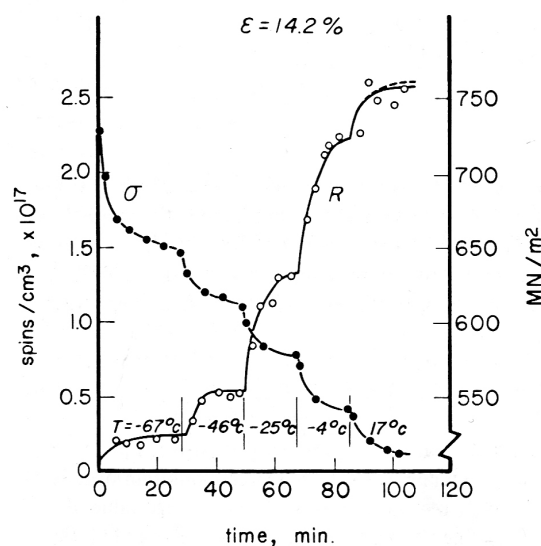


Figure 3. Concentration of free radicals and uniaxial stress in step-temperature test as a function of temperature and time for polycaprolactam fibers. ESR-Messung von Kettenbrüchen in mechanisch beanspruchtem Polyamid, by U. Johnsen and D. Klinkenberg, 1973, *Kolloid-Zeitschrift und Zeitschrift für Polymere*, volume 251, p. 848. Reprinted with permission from the publisher.⁴²

Considerations on Bond Strengths - Theoretical vs. Actual

Ultimate tensile strength of ultra-high molecular weight (UHMW) polyethylene has been theoretically determined to vary from 13.5 GPa to 60 GPa by various methods.⁴³⁻⁴⁵ However, in practice, the actual tensile strength for UHMW polyethylene is 7.2 - 9.9 GPa.⁴⁵ Theoretical estimations from models vary on the bond energy value used in calculating the force to rupture. In reported literature, researchers use the full C-C bond energy of 80 kcal/mol^{9,43,46} as well as reduced bond energies such as 26 kcal/mol for UHMWPE.⁴⁷ Previous researchers also used the energy of activation for bond disassociation such as 188 kJ/mol reported for caprolactam-based polyamide,⁸ which, based on experimental data, appears to be a valid assumption.⁹ It must be noted that macroscopic force and molecular localized pressure can be two different values entirely. Force is transferred through the repulsion of electrons and distributed throughout polymer networks based on the connected morphology. The influence of force distribution on chain scission and mechanical properties is illustrated quite clearly in the strained polyamide fibers experiment cited above. Molecular mobility of a network is key in distributing force across as many bonds as possible.^{43,48}

The force to break a C-C bond is estimated to be $3 - 6 \times 10^{-9}$ N.^{9,25,49,50} Seitz and Vincent examined the brittle fracture of approximately 18 different thermoplastics at temperatures below the beta transition.^{43,51} At these temperatures, crazing does not occur and the fracture is assumed to actually cleave through bonds. Seitz normalized the brittle stress to the number of backbone segments the crack passed through and found that each of the 18 thermoplastics required 0.038×10^{-9} N per bond (Figure 4).⁴³ This strongly

supports two possibilities: 1) only approximately 1% of the polymer chains are rupturing, or 2) there is a common local force multiplier of two orders of magnitude.⁴³

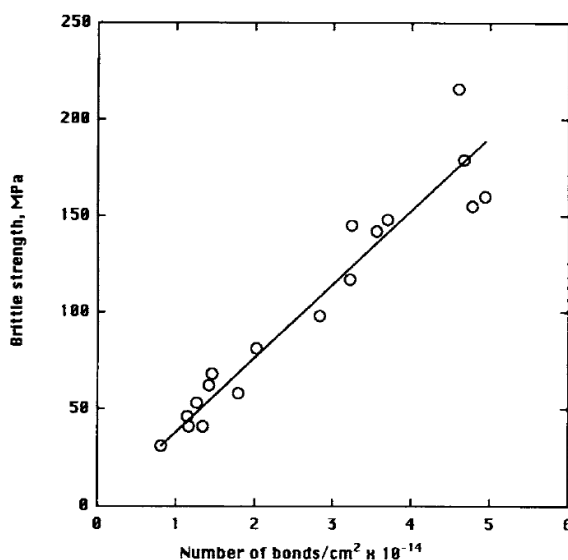


Figure 4. Brittle strength vs. number of backbone bonds. The estimation of mechanical properties of polymers from molecular structure, by J.T. Seitz, 1993, Journal of Applied Polymer Science, volume 49, p. 1346. Reprinted with permission from the publisher.⁴³

How EPR Works

One of the primary detection methods employed in this research is EPR spectroscopy. The method is similar to ¹H nuclear magnetic resonance (NMR) spectroscopy. However, instead of observing coupling between a proton and connecting nuclei, coupling is observed between a radical and an adjacent nuclei. The resulting spectra are dependent on the spin state of the adjacent nuclei, and the intensity is based on the concentration of radical species. The principle of EPR is based on the Zeeman effect (Figure 5), which states that an electron spin in the β state in a magnetic field can be promoted to the α state by the absorption of electromagnetic energy (microwaves) provided that the radiation energy is equal to the energy difference between α and β .⁵² Figure 5 depicts the relative energy levels of the spin states in the presence and absence

of a magnetic field. Unlike NMR, the radio frequency (RF) emission is fixed and the magnetic field is varied until the magnetic field and the fixed frequency are in “resonance” with the promotion of a given radical to higher spin states resulting in absorption.

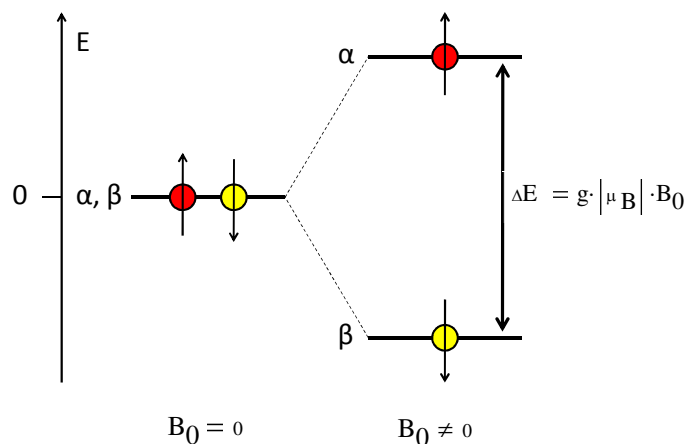


Figure 5. Illustrating the Zeeman effect on the spin states of paramagnetic electrons.

Nitroxyl Radicals for Homolytic Chain Scission Detection

Stable free radicals, specifically nitroxyl radicals, possess three key aspects that are advantageous in detecting carbon radicals. First, as the name implies, they are chemically stable under ambient and elevated temperatures.³⁴ Nitroxyl radicals are used in controlled nitroxide mediated polymerizations at temperatures of 130 °C.⁵³ Secondly, the nitroxyl radical does not form a stable bond with oxygen radicals, thus making the nitroxyl radical insensitive to oxygen.³⁴ Nitroxyl radicals can react with C, N, and P radicals³⁴ and do so at diffusion limited rates.

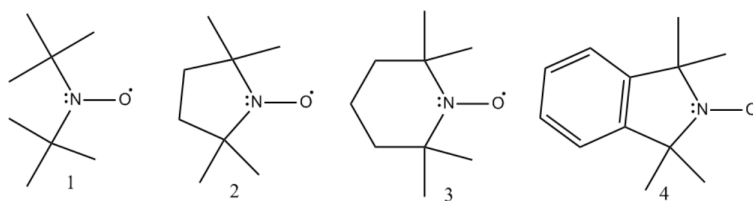


Figure 6. Stable free radical nitroxide molecules. (1) non-cyclic di-tertbutylnitroxide. (2) 2,2,5,5-tetramethylpyrrolidin-1-yloxy. (3) 2,2,5,5-tetramethylpiperdin-1-yl-oxy (TEMPO). (4) 1,1,3,3-tetramethylisoindoline-2-yloxy. Preparation and detection of degradation and chain scission events in epoxy-amine networks using a profluorescent nitroxide probe, by K.F. Fazende, 2013, The University of Southern Mississippi, p. 3. Reprinted with permission from the author.⁵⁴

Finally, nitroxyl radicals have distinct EPR spectra due to the quantum number of ^{14}N , and their concentration can be monitored in the solid state. Therefore, with the two criteria of selectivity and stability, a reduction in concentration of nitroxyls in comparison to a control can accurately be assumed to directly correlate to the production and scavenging of homolytic chain scission by-products. The advantage of this technique approach is that EPR is a sensitive spectroscopic technique with an experimental detection limit in the range of 7.5×10^{12} spins of paramagnetic species in the X-band.^{9,55,56}

Hypothesis

We hypothesize that the degradation of mechanical performance and subsequent failure of glassy thermoset polymers originates from the accumulation of chain scission events. This event occurs below the UTS of the material and results in mostly homolytic products (radicals). To test this hypothesis, nitroxyl radicals will be incorporated within glassy epoxy-amine matrices to react with homolytic byproducts of chain scission events. The concentration of nitroxyl radicals will be monitored as a function of fatigue using

EPR spectroscopy and the loss of signal compared to controls will quantify homolytic chain scission events (Figure 7).

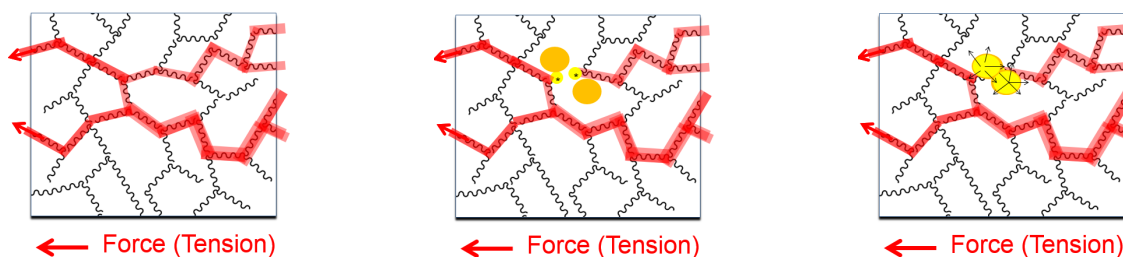


Figure 7. Illustration depicting chain scission resulting from force. Figure A depicts the force distribution throughout the thermoset polymer chains. Figure B depicts the homolytic cleavage of a bond near two nitroxyl probes represented by orange circles. Figure C depicts the reaction of the nitroxyl probes with the chain scission radicals and producing a detectable signal.

Objectives

- 1) To successfully incorporate a nitroxyl radical probe molecule within an epoxy-amine thermoset and verify that the epoxy-amine reaction chemistry is not adversely affected by such incorporation
- 2) To subject nitroxyl radical loaded epoxy-amine thermosets to varying levels of fatigue and analyze the samples via EPR to detect loss of nitroxyl radicals and, therefore, chain scission events.

Challenges

The creation of a primary radical chain end can immediately lead to a series of beta hydrogen abstractions to reduce the high potential energy of the primary radical to a lower potential energy state of a secondary or tertiary radical. This radical “migration” along the polymer backbone increases the difficulty of identifying primary scission events.^{17,18} Recombination with another radical species can result in branching, crosslinking, or scavenging of oxygen atoms. Spectroscopically, a branch site does not represent a substantial functional group change from the initial structure, and radical

lifetimes can be short due to recombination. Capturing these events and limiting their recombination is difficult while the prevention of beta hydrogen abstraction at ambient temperatures is impossible.^{17,18}

A potentially significant challenge is the mobility of the glassy state. The glassy state is an extremely viscous material with viscosities greater than 10^{13} Pa sec.⁵⁰ This strongly impedes the diffusion and mobility of the probe molecule to diffuse and react with a fractured chain segment. Literature research into diffusion and mobility of individual molecules within a glassy matrix under repetitive cycles of strain bore no answers. Radicals can migrate based on hydrogen abstraction as mentioned previously, based on chemical mobility of the radical and the potential mobility enhancement of strain. We acknowledge these challenges at the outset as we begin to test our hypothesis.

Concluding Remarks

The goal of this research is to determine if chain scission events play a significant role in the fatigue lifetime of thermoset polymeric materials. Understanding the degree and significance of chain scission will enable intelligent choices and design for future thermoset polymers.

REFERENCES

1. *Market Report: World Epoxy Resin Market*. (Acmite Market Intelligence, 2014).
2. Boeing. *787 Dreamliner Program Fact Sheet*.
<<http://www.boeing.com/boeing/commercial/787family/programfacts.page>>
(2007).
3. A. Weber. *Cirrus Soars With Composites*.
<<http://www.assemblymag.com/articles/85800-cirrus-soars-with-composites>>
(2008).
4. Cirrus-Aircraft. *Integrity in Engineering: Structure*.
<<http://whycirrus.com/engineering/structural-testing.aspx>> (2014).
5. A.J. Kinloch & R.J. Young. *Fracture Behaviour of Polymers*. (Applied Science Publishers, 1983).
6. C. Kong, J. Bang & Y. Sugiyama. Structural investigation of composite wind turbine blade considering various load cases and fatigue life. *Energy* **30**, 2101-14, (2005).
7. NASA. Structural design and test factors of safety for spaceflight hardware. NASA-STD-5001B. Washington, DC. 2014.
8. D.W. Van Krevelen & K. Te Nijenhuis. *Properties of Polymers: Their correlation with chemical structure; Their numerical estimation and prediction from additive group contributions*. (Elsevier, 2009).
9. H.-H. Kausch. *Polymer Fracture*. (Springer-Verlag, 1987).
10. S. Rabinowitz, A.R. Krause & P. Beardmore. *Materials Science* **8**, 11-22, (1973).
11. G. Tao & Z. Xia. Biaxial fatigue behavior of an epoxy polymer with mean stress effect. *International Journal of Fatigue* **31**, 678-85, (2009).
12. G. Tao & Z. Xia. An experimental study of uniaxial fatigue behavior of an epoxy resin by a new noncontact real-time strain measurement and control system. *Polymer Engineering & Science* **47**, 780-88, (2007).
13. G. Tao & Z. Xia. A non-contact real-time strain measurement and control system for multiaxial cyclic/fatigue tests of polymer materials by digital image correlation method. *Polymer Testing* **24**, 844-55, (2005).
14. G. Tao & Z. Xia. Fatigue behavior of an epoxy polymer subjected to cyclic shear loading. *Materials Science and Engineering: A* **486**, 38-44, (2008).

15. G. Tao & Z. Xia. Mean stress/strain effect on fatigue behavior of an epoxy resin. *International Journal of Fatigue* **29**, 2180-90, (2007).
16. G. Tao & Z. Xia. Ratcheting behavior of an epoxy polymer and its effect on fatigue life. *Polymer Testing* **26**, 451-60, (2007).
17. R. Porter & A. Casale. *Polymer Stress Reactions Volume 1: Introduction*. (Academic Press, 1978).
18. R. Porter & A. Casale. *Polymer Stress Reactions Volume 2: Experiments*. (Academic Press, 1979).
19. A.B. Bestul. Composition of apparent shearing forces during shear degradation of polymers. *Journal of Applied Physics* **25**, 1069-74, (1954).
20. A. Ram & A. Kadim. Shear degradation of polymer solutions. *Journal of Applied Polymer Science* **14**, 2145-56, (1970).
21. J.M. Paulusse & R.P. Sijbesma. Ultrasound in polymer chemistry: Revival of an established technique. *Journal of Polymer Science: Part A: Polymer Chemistry* **44**, 5445-53, (2006).
22. A. Piermattei, S. Karthikeyan & R.P. Sijbesma. Activating catalysts with mechanical force. *Nature Chemistry* **1**, 133-37, (2009).
23. M.M. Caruso, D.A. Davis, Q. Shen, S.A. Odom, N.R. Sottos, S.R. White & J.S. Moore. Mechanically-induced chemical changes in polymeric materials. *Chemical Reviews* **109**, 5755-98, (2009).
24. C.R. Hickenboth, J.S. Moore, S.R. White, N.R. Sottos, J. Baudry & S.R. Wilson. Biasing reaction pathways with mechanical force. *Nature (London, U. K.)* **446**, 423-27, (2007).
25. M.K. Beyer & H. Clausen-Schaumann. Mechanochemistry: □ The Mechanical Activation of Covalent Bonds. *Chemical Reviews* **105**, 2921-48, (2005).
26. D.A. Davis, A. Hamilton, J. Yang, L.D. Cremer, D. Van Gough, S.L. Potsek, M.T. Ong, P.V. Braun, T.J. Martinez, S.R. White & N.R. Sottos. Force-induced activation of covalent bonds in mechanoresponsive polymeric materials. *Nature* **459**, 68-72, (2009).
27. N. Mohammadi, A. Klein & L.H. Sperling. Polymer chain rupture and the fracture of glassy polystyrene. *Macromolecules* **26**, 1019-26, (1993).

28. M. Sambasivam, A. Klein & L.H. Sperling. The molecular basis of fracture in crosslinked glassy polymers. *Journal of Applied Polymer Science* **65**, 1001-11, (1998).
29. D.K. Backman & K.L. Devries. Formation of free radicals during machining and fracture of polymer. *Journal of Polymer Science (Part A-1)* **7**, 2125-34, (1969).
30. B.M. Fanconi. Chain scission and mechanical failure of polyethylene. *Journal of Applied Physics* **54**, 5577-82, (1983).
31. A. Acharya & B.C. Syrett. *Corrosion and Degradation of Implant Materials*. (American Society for Testing and Materials, 1979).
32. M.A. Grayson & C.J. Wolf. Mechanochemical reactions in an epoxy resin system. *Journal of Polymer Science: Polymer Physics Edition* **23**, 1087-97, (1985).
33. M.G. Panek, G.M. Villacorta, W.H. Starnes & I.M. Plitz. Fracture-induced free radicals in amine-cured epoxy resins. *Macromolecules* **18**, 1041-43, (1985).
34. J.P. Blinco. *The Synthesis and Application of Novel Profluorescent Nitroxides as Probes for Polymer Degradation*. Queensland University of Technology. (2008).
35. K.E. Fairfull-Smith & S.E. Bottle. The Synthesis and Physical Properties of Novel Polyaromatic Profluorescent Isoindoline Nitroxide Probes. *European Journal of Chemistry*, 5391-400, (2008).
36. S.E. Bottle, J.P. Blinco, J.M. Colwell, G.A. George & J.R. Walker. The Development of Novel Nitroxide Additives to Protect Against Free Radical Damage, Indicate Lifetime and Signal Damage Levels in Polymers and Coatings in *Department of Defense Corrosion Conference*. (August 10-14, 2009). Gaylord National, Washington DC.
37. A. Peterlin. Chain scission and plastic deformation in the strained crystalline polymer. *Journal of Polymer Science (Part C)* **32**, 297-317, (1971).
38. M. Sakaguchi, H. Kinpara, Y. Hori, S. Shimada & H. Kashiwabara. Mechano ions produced by mechanical fracture of solid polymer. 5. Cationic polymerization of isobutyl vinyl ether initiated by the mechano cation of poly(vinylidene fluoride). *Macromolecules* **22**, 1277-80, (1989).
39. M. Sakaguchi, H. Kinpara, Y. Hori, S. Shimada & H. Kashiwabara. Ionic products from the mechanical fracture of solid polypropylene. *Polymer* **25**, 944-46, (1984).

40. M. Sakaguchi, Y. Miwa, S. Hara, Y. Sugino, K. Yamamoto & S. Shimada. Triboelectricity in polymers: effects of the ionic nature of carbon-carbon bonds in the polymer main chain on charge due to yield of mechanoanions produced by heterogenous scission of the carbon-carbon bond by mechanical fracture. *Journal of Electrostatics* **62**, 35-50, (2004).
41. M. Sakaguchi & J. Sohma. ESR evidence for main-chain scission produced by mechanical fracture of polymers at low temperature. *Journal of Polymer Science Part B: Polymer Physics Edition*. **13**, 1233-45, (1975).
42. U. Johnsen & D. Klinkenberg. ESR-Messung von Kettenbrüchen in mechanisch beanspruchtem Polyamid. *Kolloid-Zeitschrift und Zeitschrift für Polymere* **251**, 843-49, (1973).
43. J.T. Seitz. The estimation of mechanical properties of polymers from molecular structure. *Journal of Applied Polymer Science* **49**, 1331-51, (1993).
44. Y. Termonia, P. Meakin & P. Smith. The theoretical study of the influence of the molecular weight on the maximum tensile strength of polymer fibers. *Macromolecules* **18**, 2246-52, (1985).
45. M.J.N. Jacobs. *Creep of Gel-Spun Polyethylene Fibres: Improvements by Impregnation and Crosslinking*. (Eindhoven University of Technology, 1999).
46. M.B. Smith & M. Jerry. *March's Advanced Organic Chemistry: Reactions, Mechanisms, and Structure*. (John Wiley and Sons, Inc, 2007).
47. J. Wang & K.J. Smith Jr. The breaking strength of ultra-high molecular weight polyethylene fibers. *Polymer* **40**, 7261-74, (1999).
48. H.E.H. Meijer & L.E. Govaert. Mechanical performance of polymer systems: The relationship between structure and properties. *Progress in Polymer Science* **30**, 915-38, (2005).
49. A. Kelly. *Strong Solids*. (Clarendon Press, 1966).
50. L.H. Sperling. *Introduction to Physical Polymer Science*. (John Wiley and Sons, 2006).
51. P.I. Vincent. Correlation between critical tensile strength and polymer cross-sectional area. *Polymer* **13**, 558-60, (1972).
52. *Electron Paramagnetic Resonance: A Practitioner's Toolkit*. (John Wiley & Sons, Inc, 2009).

53. C.J. Hawker, A.W. Bosman & E. Harth. New Polymer Synthesis by Nitroxide Mediated Living Radical Polymerizations. *Chem. Rev. (Washington, D. C.)* **101**, 3661-88, (2001).
54. K.F. Fazende. *Preparation and detection of degradation and chain scission events in epoxy-amine networks using a profluorescent nitroxide probe*. The University of Southern Mississippi. (2013).
55. *Bruker Biospin*. <<http://www.bruker-biospin.com/cwperformance-sense.html>> (2014).
56. G.R. Eaton, S.S. Eaton, D.P. Barr & R.T. Weber. *Quantitative EPR*. (Springer, 2010).

CHAPTER II

MATERIALS AND EXPERIMENTAL DETAILS

Introduction

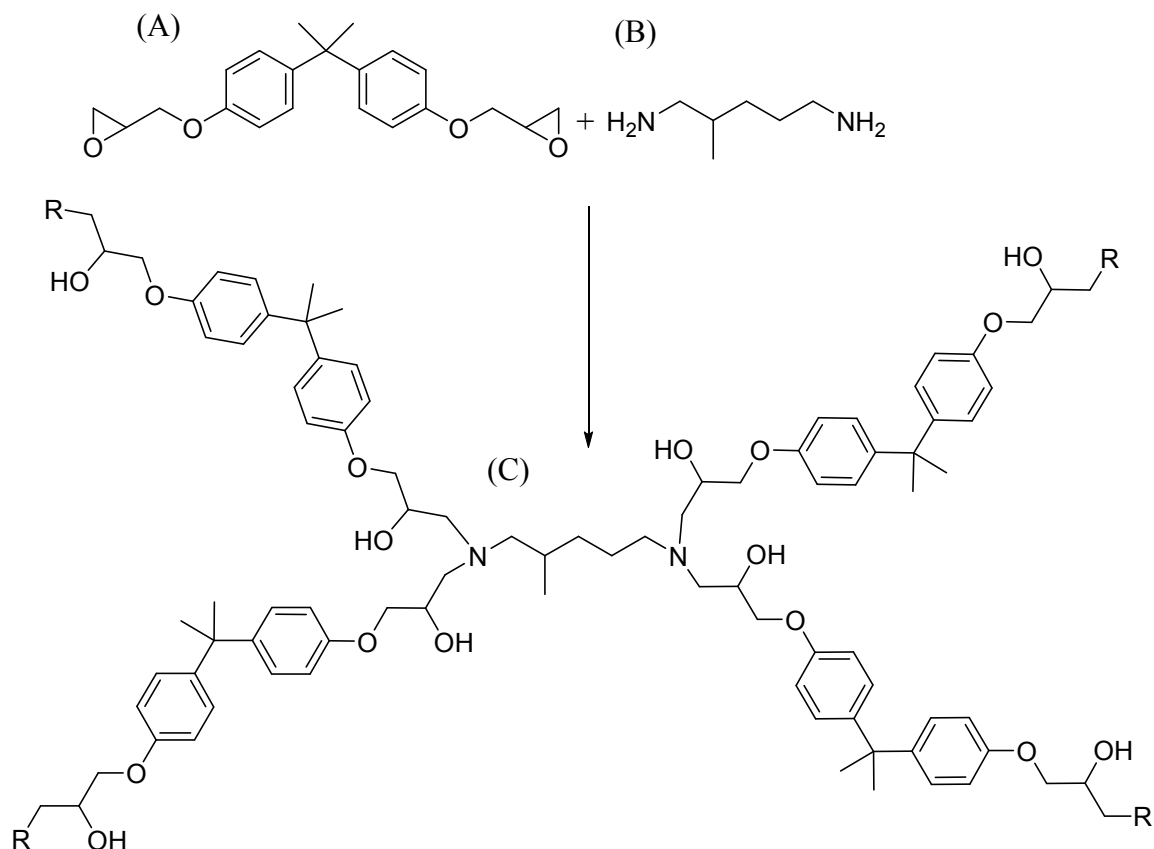
The studies throughout this research into epoxy-amine thermosets use specific materials selected for their chemistry type and thermal considerations. Their structures are reported in Scheme 1. Diglycidyl ether of bisphenol-A (DGEBA) is an epoxy monomer commonly used in research and industry. Epon[®] 828 (Hexion Chemicals) is primarily DGEBA, with ~ 10% of the molecules being extended by one repeat unit to inhibit crystallization.

Amine selection was predicated on the T_g of the final material being conducive to thermal characterization. Previous thermogravimetric analysis (TGA) indicated the homolytic chain scission probes degraded at ~ 145 °C. Therefore, a T_g of ~ 100 °C was considered appropriate to allow complete thermal cure without degrading the nitroxyl radicals. Aliphatic amines were favored as their primary amine overtone would not overlap with the epoxy overtone during NIR analysis. The amine employed in this research was 2-methyl-1,5-diaminopentane and purchased (> 99% pure) from TCI America. The nitroxyl based molecule 4-hydroxy-TEMPO was donated by Evonik and used as received. Isophorone diisocyanate (IPDI) was purchased from Bayer[®] and used as received.

Epoxy-Amine Thermoset Materials

Purity and equivalence of DGEBA was confirmed by quantitative ¹H NMR and ¹³C NMR analysis as well as epoxide functional equivalent weight titrations following ASTM D 1652. The purity and equivalence of 2-methyl-1,5-diaminopentane was

confirmed through quantitative ^1H NMR and ^{13}C NMR spectroscopy. Total amine functional equivalent weight was determined via ASTM D 2073 methods. Thermoset matrices were synthesized by mixing DGEBA and 2-methyl-1,5-diaminopentane in 1:1 stoichiometric ratios (Scheme 2). Cure schedules and conditions will be reported in their respective chapters and sections.

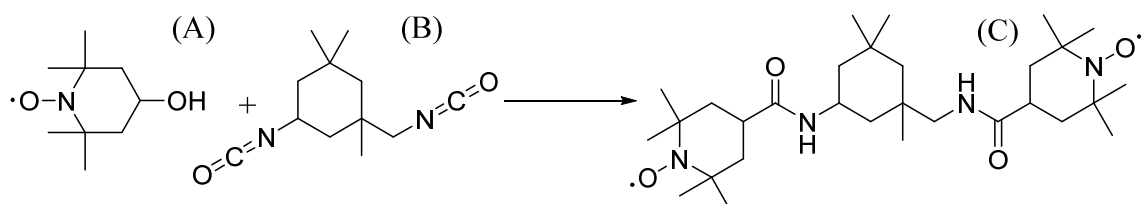


Scheme 1. Reaction of (A) DGEBA and (B) 2-methyl-1,5-diaminopentane to form (C) crosslinked epoxy-amine network. R notation is an infinite continuation of the network. Theoretical crosslink density is 436 g/mol based on a 1:1 stoichiometric ratio.

Synthesis of Stable Free Nitroxyl Radical Probes

The low molecular weight TEMPO and 4-hydroxy-TEMPO volatilize at approximately 110 °C based on TGA data. To increase thermal stability for epoxy-amine polymerization temperatures, 4-hydroxy-TEMPO was reacted with IPDI to form the

product bis-TEMPO-IPDI (BT-IPDI) as shown in Scheme 2. The thermal stability of BT-IPDI extends to 150 °C as measured via TGA, approximately 50 °C higher than the original TEMPO materials. Isophorone diisocyanate (IPDI) was purchased from Bayer® and used as received.



Scheme 2. Reaction of (A) 4-hydroxy TEMPO and (B) isophorone diisocyanate to form (C) bis-TEMPO IPDI (BT-IPDI).

BT-IPDI was synthesized at 80 °C under dry nitrogen using chloroform as the solvent and dibutyltin dilaurate as catalyst. A 2.01:1 molar ratio of 4-hydroxy TEMPO to isophorone diisocyanate was used to ensure that all the NCO groups were reacted. The isocyanate was added drop wise to the reaction mixture over a two hour period, and the reaction was continued until the NCO stretching absorption band (2263 cm^{-1}) could no longer be detected in the FTIR spectrum. The product was concentrated under reduced pressure, and the final traces of solvent were removed in a vacuum oven at 60 °C. The resulting product was a red crystalline powder.

Characterization of Bis-TEMPO-IPDI

Gel Permeation Chromatography

Gel permeation chromatography was performed using a Varian PL GPC-50 equipped with dual angle light scattering, differential pressure, refractive index detectors, a series of three Polymer Laboratory columns (two polypore and one 5 Å PLGel column), and the eluent, tetrahydrofuran (THF), flow rate was 0.5 mL/min at 40 °C. An internal standard was used with fixed volume quantities of toluene as a flow rate marker.

Polystyrene standards were used to calibrate the detectors. The GPC trace in Figure 8 shows a large single peak (50 min) with a slight shoulder that corresponds to over indexed IPDI that has advanced one repeat unit by reacting with trace amounts of water.

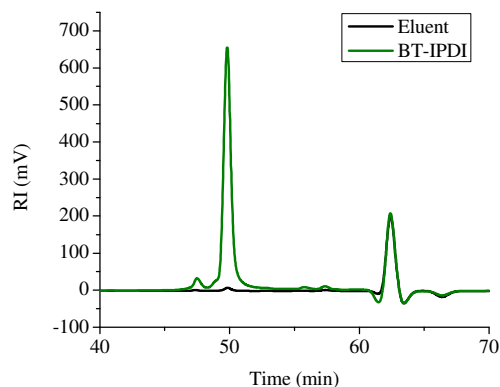


Figure 8. GPC spectrum of BT-IPDI product. Peak at 64 min is toluene, the flow rate marker.

BT-IPDI Functional Equivalent Weight Titration

EPR Spectroscopy

Quantitative EPR spectroscopy was performed using a Bruker EMX^{Micro} X-band spectrometer using quartz tubes of approximately 3 mm outer diameter at ambient temperature. Capillary inserts were used to reduce volume within the cavity due to the high dielectric constant of acetonitrile. The following EPR instrumental settings were used to acquire each spectrum: a microwave power of 0.597 mW, receiver gain of 5020, frequency of 9.87 GHz, modulation amplitude of 2 gauss, modulation frequency of 100 KHz, conversion time of 20.48 msec, time constant of 20.48 msec, and signal averaging of 4 scans.

Active nitroxyl radicals cannot be characterized via NMR methods due to the paramagnetic nature of a free radical. Characterization through MALDI-TOF analysis was attempted, but the results were unsatisfactory. The functional equivalent weight of

the active nitroxyl radicals was determined by titrating BT-IPDI using the radical photoinitiator 2,4,6-trimethylbenzoyldiphenylphosphine oxide (TPO). Quantitative reaction of nitroxyl radicals and TPO have been reported in literature.¹ Experimental procedures were carefully selected to prevent side reactions from occurring. This was achieved through selection of a solvent with hydrogens that are not susceptible to abstraction and the removal of oxygen from the reaction solution. Acetonitrile was selected as a suitable solvent, with the reaction performed under a nitrogen atmosphere in a dry box. The molar ratio of the photo-initiator to nitroxyl was kept in excess to favor reaction between the high potential energy radical initiator and the stable nitroxyl radical.

Oxygen was removed from acetonitrile through a series of three freeze-pump-thaw cycles. The reaction was performed under dry box and darkroom conditions. The light source was a 395 nm wavelength LED, and samples were irradiated for approximately one minute. Because the intensity and wavelength distribution of the photo-source is unknown, lengthy exposure times to small concentrations were utilized to ensure complete reaction of the photo-initiator. The initial BT-IPDI and TPO concentration were 1.5 mg/mL and 0.1 mg/mL respectively. Serial dilution was used to generate three samples with three extractions measured via EPR spectroscopy to yield triplicate results. Double integration was performed to obtain the spectral area. In quantitative EPR analysis, the spectral area is directly proportional to concentration.²

Figure 9 presents a graphical illustration of the experiment. Four vials were prepared, one initial concentration of 1.5 mg/mL BT-IPDI in acetonitrile and three vials of 1 mL solutions of TPO and acetonitrile at a concentration of 0.1 mg/mL. The experiment began by extracting 1 mL of BT-IPDI and mixing it with the first vial of

TPO. Then 1 mL from this solution was extracted and mixed with the second vial. After mixing, all the vials were exposed to the 395 nm wavelength photo-source for one minute then characterized using EPR spectroscopy.

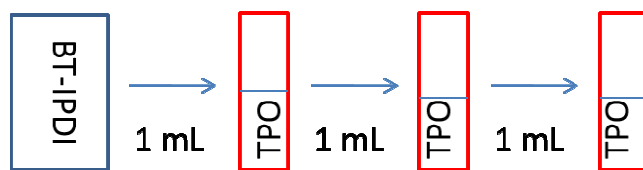
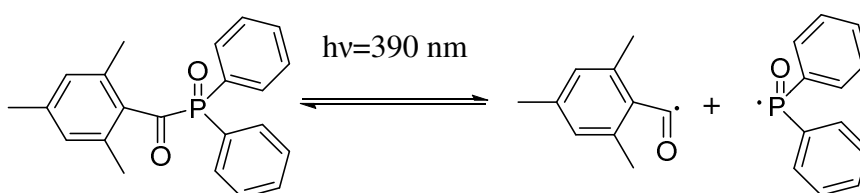
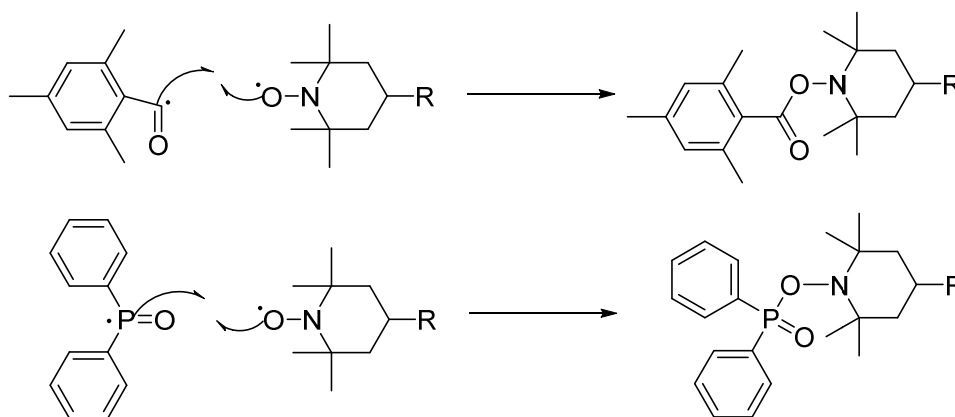


Figure 9. Illustration of BT-IPDI titration serial dilution experiment.



Scheme 3. Radical photoinitiator 2,4,6-trimethylbenzoyldiphenylphosphine oxide (TPO) undergoing disassociation following exposure to 390 nm radiation.¹



Scheme 4. Reaction of radical photoinitiator 2,4,6-trimethylbenzoyldiphenylphosphine oxide (TPO) with TEMPO nitroxyl radicals.¹

In quantitative EPR spectroscopy, the spectral area is directly proportional to concentration.² In Figure 10, extrapolation to approximately zero intensity demonstrates linear dependence of EPR signal to radical concentration.

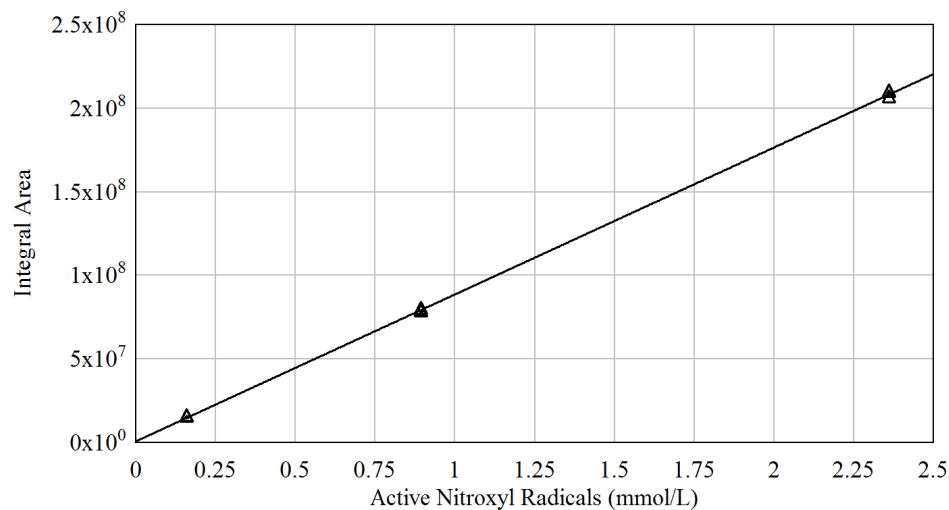


Figure 10. Integral area of EPR signal versus calculated concentration of nitroxyl radicals assuming 100% conversion.

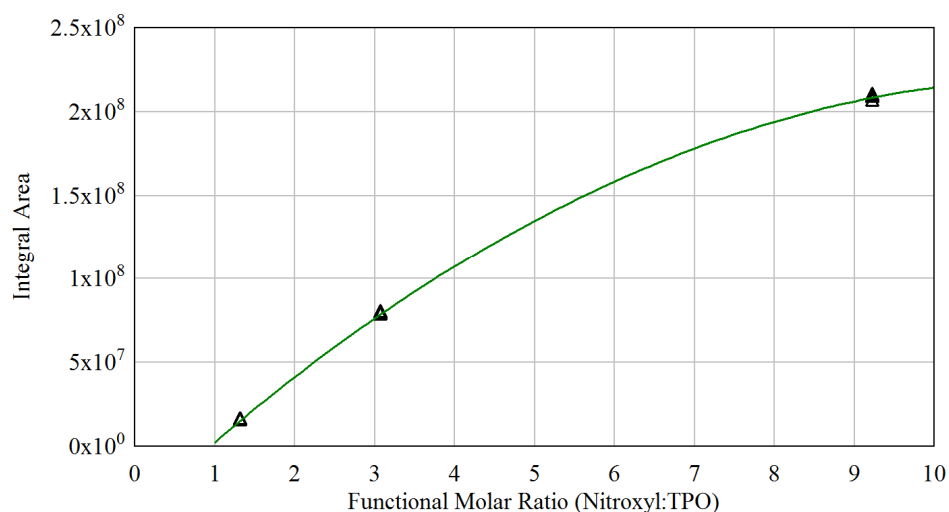


Figure 11. Integral area of EPR signal versus functional ratio predicted concentration of nitroxyl radicals assuming 100% conversion. The line is fitted to predict the x intercept.

In Figure 11, the observed trend to zero intensity at 1:1 molar ratios (Nitroxyl:TPO) confirmed that the reaction was quantitative and validated the functional equivalent weight of BT-IPDI. The non-linear relationship between the integral area and functional molar ratio is due to the integral area of the EPR signal and is dependent upon radical concentration rather than the molar ratio. However, Figure 11 illustrates that at a

1:1 molar ratio, no free radicals are present. The shape of the curve solely depends upon the volumetric dilutions chosen in the experimental procedure. The green line was fitted to confirm extrapolation to the x-axis was equal to one. Figures 10 and 11 complement each other in that Figure 11 confirms the nitroxyl radical functionality while Figure 10 yields the correct slope of EPR signal with concentration. Using the slope of Figure 10, a mathematical simulation of various starting concentrations of BT-IPDI was generated (Figure 12), which confirm that the EPR signal reduces to zero as the molar ratio of nitroxyl radical to TPO approaches unity. The simulation allows confirmation of Figure 10 and 11 without experimentally measuring the reaction at nitroxyl to initiator ratios that would favor unwanted side reactions.

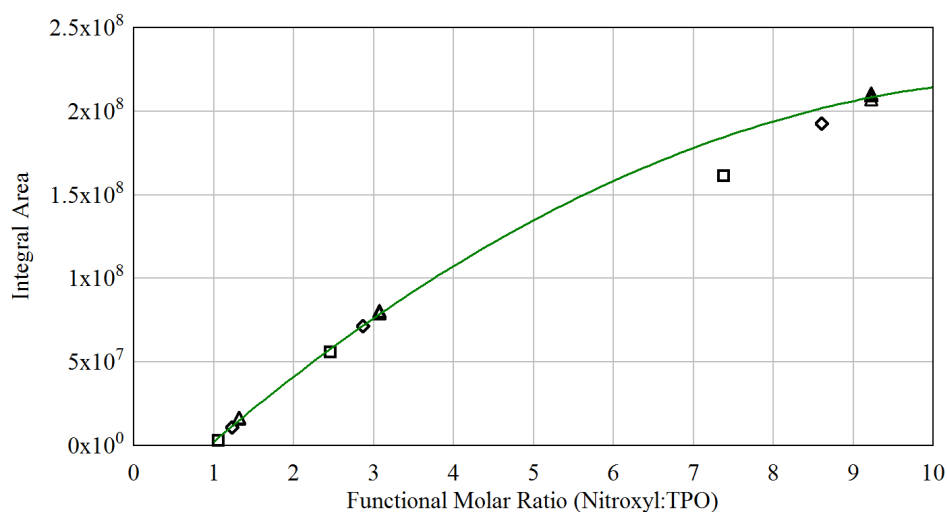


Figure 12. Mathematical simulations of various starting concentrations of BT-IPDI for the volumetric titration experiment. Fitted slope and points are experimental data from Figure 10. \diamond Simulation of starting BT-IPDI concentration of 1.4 mg/mL. \square Simulation of starting BT-IPDI concentration of 1.2 mg/mL.

Pressure-Volume-Temperature High Pressure Dilatometry

Free Volume of DGEBA and 2-methyl-1,5-diaminopentane

Epon 828 (DGEBA) was degassed for six hours under vacuum before being mixed with 2-methyl-1,5-diaminopentane at a 1:1 stoichiometric ratio. The blend was cured at 60 °C for 1.5 hours followed by 120 °C for 1.5 hours under nitrogen atmosphere. Prior to PVT analysis, the sample was thermally treated under nitrogen atmosphere (Figure 13) to ensure complete cure and an exact thermal history to eliminate temporal aging effects.

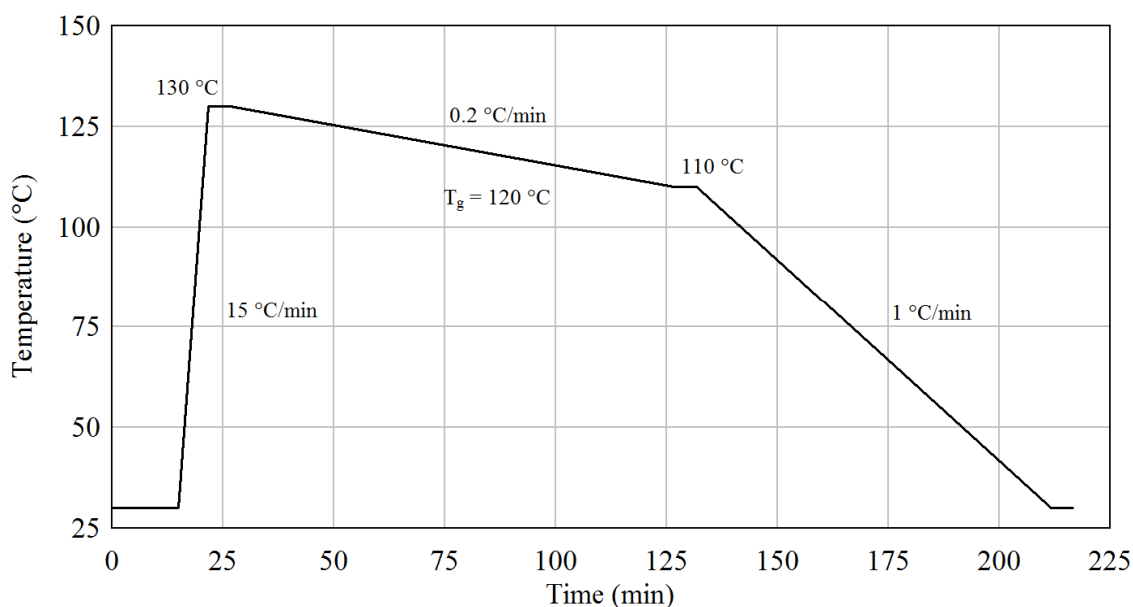


Figure 13. Thermal cycle to remove aging prior to PVT analysis.

Density was measured via an immersion displacement method using a Mettler Toledo XS104 analytical balance equipped with a density determination kit and water as the immersion fluid. Specific volume as a function of temperature and pressure was determined using a Gnomix dilatometer (Gnomix, Boulder, CO) as described by Zoller.³ Dilatometric experiments were conducted using Pressure-Volume-Temperature (PVT) analysis. Figure 14 shows the change in volume with temperature at various pressures.

The data points at zero pressure were extrapolated using Tait equations within the Gnomix software and are accurate to within $\pm 0.00015 \text{ cm}^3/\text{g}$.

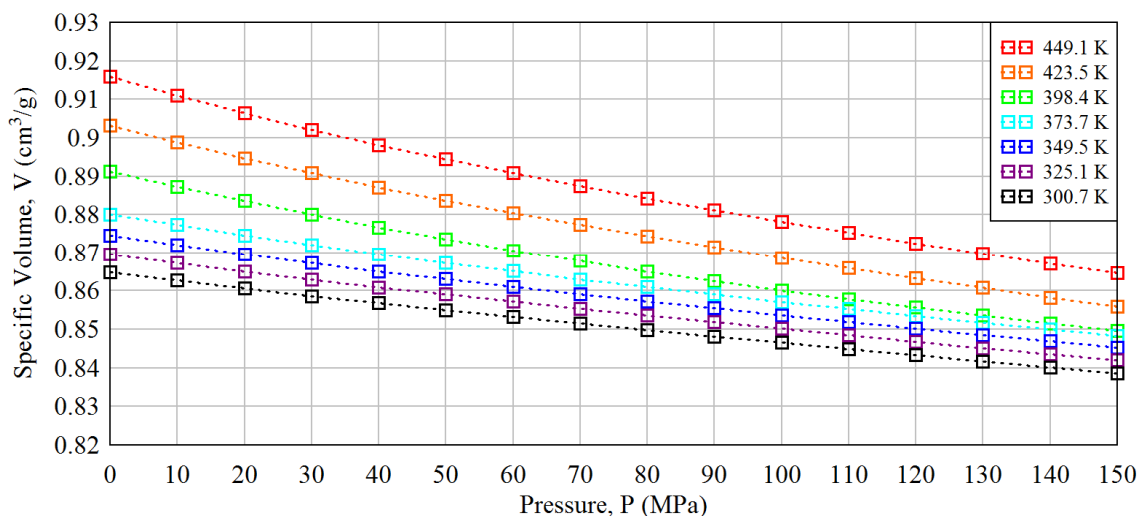


Figure 14. PVT of DGEBA – 2-methyl-1,5-diaminopentane at various temperatures and pressures.

Sample free volume was calculated using the Simha-Somcynsky equation of state (SS-EOS, Equation 1). The SS-EOS was first derived to describe spherical and chain molecule fluids but has since been applied to high molecular weight polymers.⁴ This equation describes free volume using a cell or lattice model and assumes a statistical mixture of occupied (o) and unoccupied cells ($u = 1 - o$) of the same size. The SS-EOS in Equation 2 was derived assuming liquids under thermodynamic equilibrium conditions using the Helmholtz free energy and the partition function Z (Equation 1).⁵ In literature, the fraction of occupied lattice site variable “o” is originally denoted as “y”. However, this equation is solved later using a graphical method by graphing “y” as x and reports the x axis intercept as the solution. Therefore, the variable “y” is renamed to “o” to minimize confusion of the reader.

$$F = -kT \ln Z$$

Equation 1. Helmholtz free energy, F.

$$\frac{\tilde{P}\tilde{V}}{\tilde{T}} = \left[1 - o(2^{\frac{1}{2}}o\tilde{V})^{-\frac{1}{3}}\right]^{-1} + \frac{o}{\tilde{T}} [2.002(o\tilde{V})^{-4} - 2.409(o\tilde{V})^{-2}]$$

Equation 2. Simha-Somcynski Equation of State (SS-EOS).⁵

$$\tilde{P} = \frac{P}{P^*} \quad \tilde{T} = \frac{T}{T^*} \quad \tilde{V} = \frac{V}{V^*}$$

Equation 3. Reduced parameters \tilde{P} , \tilde{T} , and \tilde{V} .⁵

Assuming a pressure of zero, Utracki and Simha simplified the equation of state in the equilibrium melt state to Equation 4, which relates the specific volume V to fit parameters V^* and T^* , as well as constants a_0 and a_1 .⁶

$$V(P, T) = V^* \times \exp \left(a_0 + a_1 \left(\frac{T}{T^*} \right)^{\frac{3}{2}} \right)$$

Equation 4. Reduced SS-EOS at zero pressure.⁶

For PVT analyses of epoxy-amine thermosets, researchers have used the values of $a_0 = -0.1033$ and $a_1 = 23.85$.⁷ Inserting these constants back into the expression and taking the natural logarithm of both sides yields Equation 5.

$$\ln V = \ln V^* - 0.1033 + 23.85 \times T^{\frac{3}{2}} \times \left(\frac{1}{T^*} \right)^{\frac{3}{2}}$$

Equation 5. Natural logarithm of reduced SS-EOS with a_0 and a_1 values.

Fit parameters V^* and T^* will remain constant with changing volume and temperature. After inserting specific volume (V) measurements above the T_g , the equation can be solved to yield a value of 12343.8 K for T^* and 0.86063 for V^* . Inserting these values of V^* and T^* into Equation 4 and graphing $f(T)$ against specific volume, V (Figure 15), indicates the calculated values of V agree well with experimental values for the rubbery state.

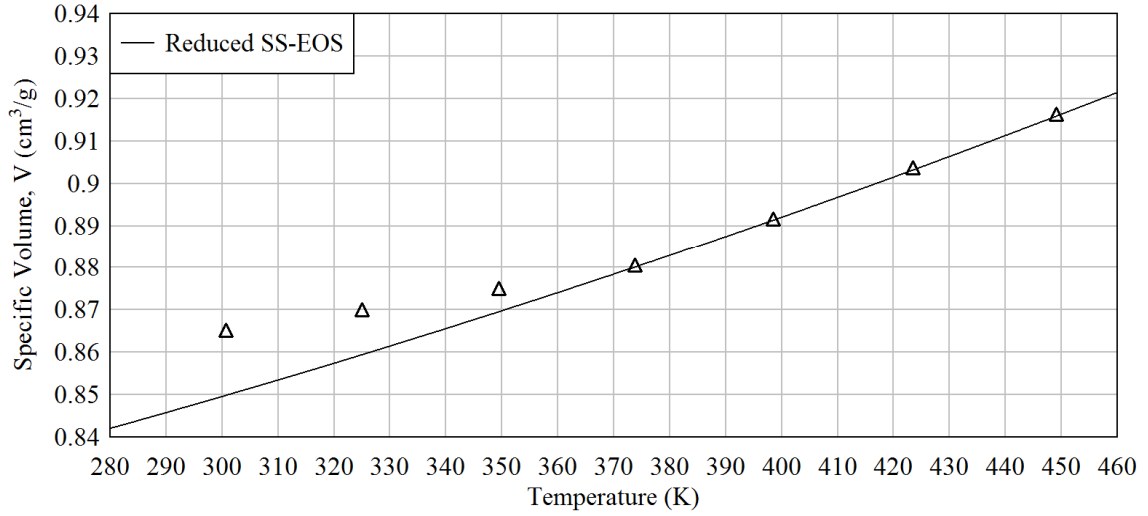


Figure 15. PVT of DGEBA – 2-methyl-1,5-diaminopentane. Fitted line is reduced SS-EOS (Equation 4) using solved V^* (0.86063) and T^* (12343.8 K).

Equation 2 gives the relationship between the reduced parameters \tilde{P} , \tilde{T} , \tilde{V} and o , the fraction of occupied lattice sites. At zero pressure, the left side of the equation becomes zero as shown in Equation 6.

$$0 = \left[1 - o(2^{\frac{1}{2}}o\tilde{V})^{-\frac{1}{3}} \right]^{-1} + \frac{o}{\tilde{T}} [2.002(o\tilde{V})^{-4} - 2.409(o\tilde{V})^{-2}]$$

Equation 6. Simha-Somcynski Equation of State (SS-EOS) at zero pressure.⁵

Reduced parameters \tilde{T} and \tilde{V} can be calculated using the solved fit parameters V^* and T^* at measured specific volume and temperature points from the PVT experimental data. By graphing equation 6 with fractional occupied lattice site variable o as the independent x variable, the x intercept at $y = 0$ solves for o . Equations 7 and 8 relate the calculation of occupied volume and thus free volume using the fractional occupied lattice site variable o .

$$V_{occ} = V \times o$$

Equation 7. Occupied volume (V_{occ}) calculated from specific volume (V) and fractional occupied lattice site (o).

$$V = V_{occ} + V_f$$

Equation 8. Specific volume (V) as a sum of occupied volume (V_{occ}) and free volume (V_f).

Equations 7 and 8 relate the calculation of occupied volume and thus free volume using the fractional occupied lattice site variable ϕ . Figure 16 depicts graphically the calculated values of specific occupied volume (V_{occ}), specific free volume (V_f), and the experimentally measured specific volume (V) as reported in Table 1. Of special importance that will be used in later chapters is the density measurement at 176 °C. This measurement is approximately 50 °C above the glass transition temperature and will be used to calculate crosslink density via the storage modulus obtained through dynamic mechanical analysis (DMA) experiments. Table 1 summarized the experimental data and calculated V_{occ} , V_f , and bulk modulus values from the PVT experiment of DGEBA and 2-methyl-1,5-diaminopentane.

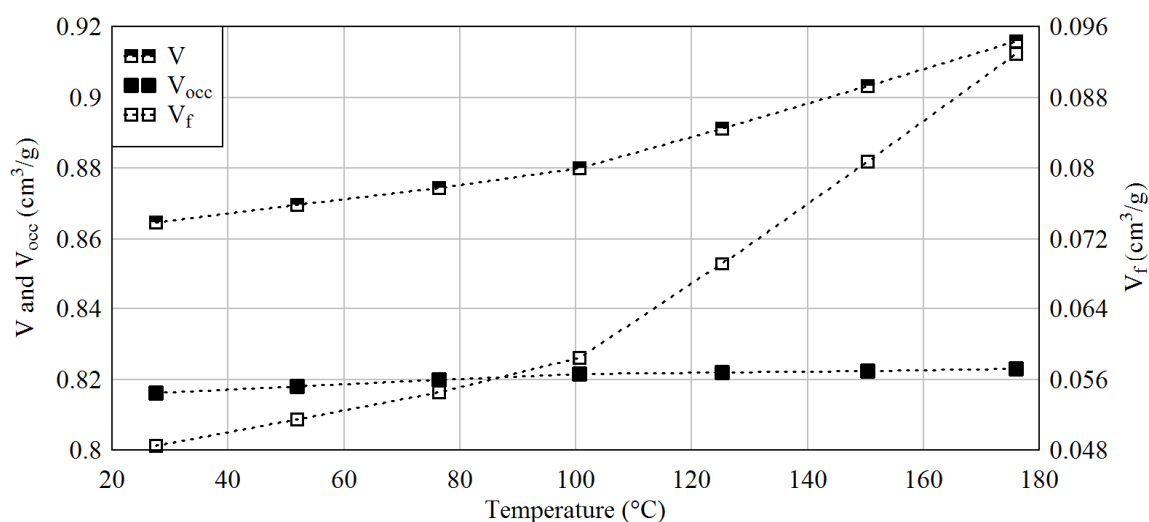


Figure 16. PVT data for DGEBA and 2-methyl-1,5-diaminopentane. Plotted are specific volume (V), specific occupied volume (V_{occ}), and specific free volume (V_f).

Table 1

PVT Experimental Data and Calculated V_{occ} , V_f and Bulk Modulus

T (°C)	ρ (g/cm ³)	V (cm ³ /g)	V_{occ} (cm ³ /g)	V_f (cm ³ /g)	Bulk Modulus (GPa)
27.6	1.1564	0.8647	0.8162	0.0485	4.211
51.9	1.1500	0.8696	0.8181	0.0515	3.867
76.3	1.1435	0.8745	0.8199	0.0546	3.569
100.6	1.1364	0.8800	0.8216	0.0584	3.253
125.3	1.1221	0.8912	0.8220	0.0692	2.338
150.4	1.1072	0.9032	0.8224	0.0807	2.093
176.0	1.0918	0.9159	0.8229	0.0930	1.916

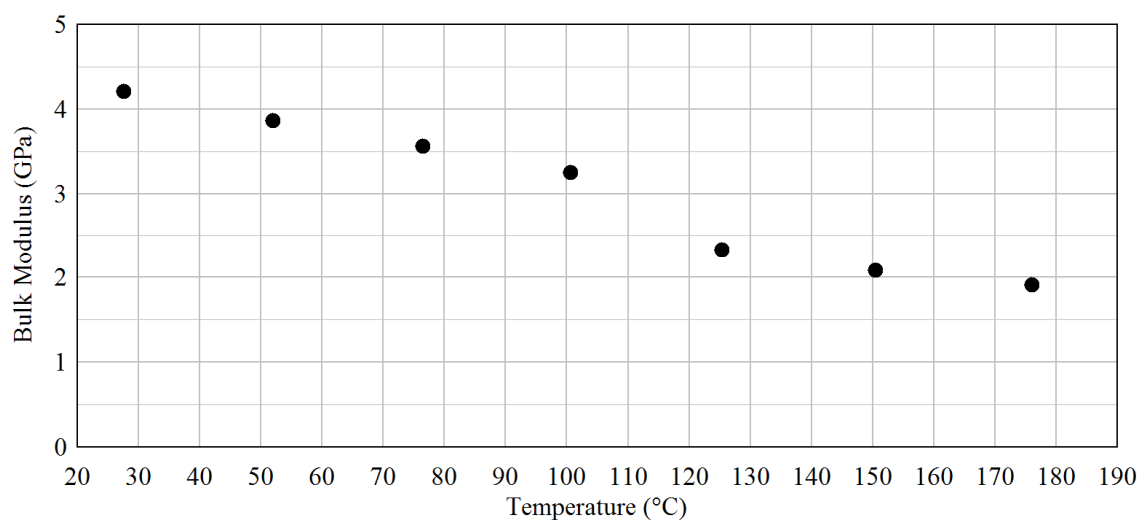


Figure 17. Bulk modulus versus temperature of DGEBA and 2-methyl-1,5-diaminopentane.

Table 2

Calculated Percent Fractional Free Volume at 300 K

Epoxy-(Amine)	% V_f
DGEBA-(2-methyl-1,5-diaminopentane)	5.6
DGEBF-(3'3'-Diaminodiphenyl Sulfone)	4.7 ^a
DGEBF-(4'4'-Diaminodiphenyl Sulfone)	5.2 ^a

Note a: Values calculated from experimental data reported in Figure II-12.⁷

Figure 17 depicts the bulk modulus versus temperature obtained from PVT experiments at variable pressures. The offset in the slopes of the curve reflects the influence of the T_g . The percent free volume relative to specific volume of DGEBA and 2-methyl-1,5-diaminopentane is 5.6% at ambient temperature. Although the fit parameters V^* and T^* were calculated through different methods, the calculated value for the DGEBA-(2-methyl-1,5-diaminopentane) system agrees well with the reported percent fractional free volume of other thermosets as determined by PVT analysis (Table 2).

The data in Table 2 for 3'3'-DDS and 4'4'-DDS were determined using the same PVT instrument reported here. The aliphatic amine should yield higher amounts of free volume as compared with the more dense aromatic structure. It should be noted that other values for free volume of epoxy-amine thermosets have been reported by researchers using PVT and SS-EOS methods⁸. However, no justification was provided for cure temperatures, and the epoxy-amine conversion was not verified. Therefore, the

fractional free volume values obtained remain suspect and are significantly larger than reported here.

REFERENCES

- 1 U. Kolczak, G. Rist, K. Dietliker & J. Wirz. Reaction Mechanism of Monoacyl- and Bisacylphosphine Oxide Photoinitiators Studied by ^{31}P -, ^{13}C -, and ^1H -CIDNP and ESR. *J. Am. Chem. Soc.* **118**, 6477-89, (1996).
- 2 G.R. Eaton, S.S. Eaton, D.P. Barr & R.T. Weber. *Quantitative EPR*. (Springer, 2010).
- 3 P. Zoller, P. Bolli, V. Pahud & H. Ackermann. Apparatus for measuring pressure-volume-temperature relations of polymers to 350 °C and 2200 kg/cm². *Rev. Sci. Instrum.* **47**, 948-52, (1976).
- 4 R. Simha & T. Somcynsky. Statistical thermodynamics of spherical and chain molecule fluid. *Macromolecules* **2**, 342-50, (1969).
- 5 R.E. Robertson, R. Simha & J.G. Curro. Free volume and the kinetics of aging of polymer glasses. *Macromolecules* **17**, 911-19, (1984).
- 6 L.A. Utracki & R. Simha. Analytical representation of solutions to lattice-hole theory. *Macromol. Theory Simul.* **10**, 17-24, (2001).
- 7 M. Kaushik. *Free volume studies of various polymeric systems using positron annihilation and PVT-EOS analyses*. The University of Southern Mississippi, (2011).
- 8 S. Goyanes, W. Salgueiro, A. Somoza, J.A. Ramos & I. Mondragon. Direct relationships between volume variations at macro and nanoscale in epoxy systems. PALS/PVT measurements. *Polymer* **45**, 6691-97, (2004).

CHAPTER III
CHEMO-RHEOLOGICAL CHARACTERIZATION OF EMBEDDED REACTIVE
MATERIALS

Introduction

The objective of this chapter is to establish that the incorporation of nitroxyl radicals and molecules containing urethane groups does not inhibit the reaction or network formation of DGEBA / 2-methyl-1,5-diaminopentane in view of the potential competing mechanisms between the additives and the epoxy and amine functional groups. Blocked isocyanates synthesized by reacting IPDI individually with *N*-methyl aniline, ϵ -caprolactam, and 4-hydroxy TEMPO were embedded into epoxy-amine thermosetting systems. Near infrared spectroscopy and dynamic rheology were employed in combination to quantify the effects of conversion at 30 °C.

Gilbert *et al.* evaluated isocyanates as latent curing agents to affect final material properties such as water absorption characteristics.¹⁻³ Other subsequent studies in blocked diisocyanate modified epoxies focused on spectroscopically identifying the modification mechanisms. When systems containing blocked isocyanates are heated above the deblocking temperature, the deblocked and free isocyanates are capable of reacting into the network causing material property changes. In this study, care was taken to ensure that the blocked isocyanates were chemically compatible and that our characterization quantified whether the premature reactions adversely affect network formation, pot life, or processability. Critical for our long term research goals are to preserve the functional groups throughout polymer synthesis and avoid any epoxy-amine consumption in advance of network formation.

Kinetic studies using FT-IR techniques are well known in the literature⁴ with real time spectroscopic techniques utilized to monitor functional group conversion.⁵ Obtaining quantitative data in the mid-IR range is often challenging due to significant peak overlaps in the fingerprint region. The NIR region contains overtone peaks that allow quantitative analysis of functional groups such as N-H, C-H, and O-H.⁶ Near infrared spectroscopy has been used to study the kinetics of a variety of epoxy systems, including aromatic and aliphatic monomers.⁷⁻⁹

Rheological techniques have been used extensively to probe the viscoelastic response of polymers and monitor a variety of parameters including cure. The combination of spectroscopic data and rheology (chemorheology) has been successfully employed to study polymer systems¹⁰, including epoxy systems.¹¹ Recent studies have incorporated both FT-NIR and rheological techniques to quantitatively elicit chemical and mechanical insight into the curing process.¹²⁻¹⁵

Materials

Dibutyltin dilaurate, *N*-methyl aniline (NMA), ϵ -caprolactam, 1,2-cyclohexane diaminopentane, and 2-methyl-1,5-diaminopentane were purchased from Sigma Aldrich. Chloroform and deuterated chloroform (99.8%+, 0.03 v/v% tetramethyl silane, TMS) were purchased from Fisher Scientific and Acros Organics (a division of Fisher Scientific) respectively. Isophorone diisocyanate, Epon 828 (DGEBA) and 4-hydroxyl-2,2,6,6 tetramethylpiperidine-1-oxyl were generously donated by Bayer MaterialScience, Hexion, and Evonik Industries, respectively. Salt plates (32 mm x 3 mm) and Teflon spacers (0.2 mm) were purchased from Crystal Labs. Bis(2-ethylhexyl) phthalate

(BEHP) was procured from Alfa Aesar. All chemicals were used as received unless otherwise noted.

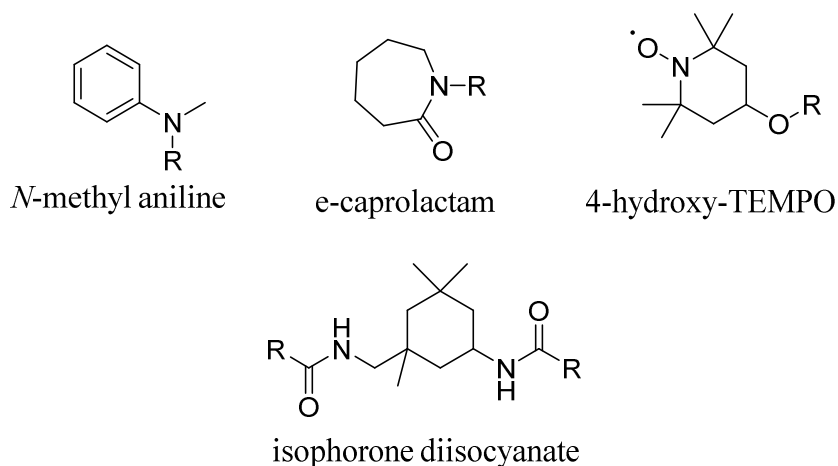


Figure 18. Blocked isocyanate additive structures with core comprising isophorone diisocyanate (IPDI) and R' composed of *N*-methyl aniline, ϵ -caprolactam, or 4-hydroxy-TEMPO.

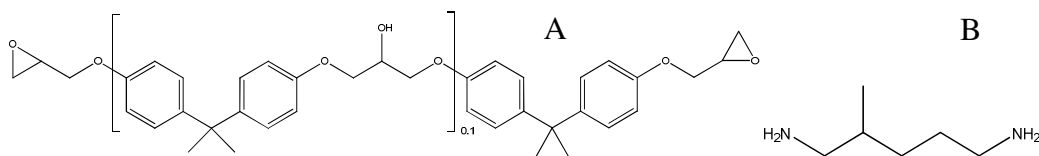


Figure 19. Thermoset epoxy-amine comprised of (A) Epon 828 (DGEBA) and (B) 2-methyl-1,5-diaminopentane.

Synthesis

Blocked isocyanates were synthesized at 80 °C under dry nitrogen using chloroform as a solvent and dibutyltin dilaurate as catalyst. A 2.01:1 molar ratio of blocking agent to isocyanate was used to ensure complete reaction of all the NCO groups. The isocyanate was added drop wise to the reaction mixture over two hours, and the reaction was continued until the -NCO stretching absorption band (2263 cm^{-1}) could no longer be detected in the FT IR spectrum. The product was concentrated under reduced pressure and final traces of the solvent were removed in a vacuum oven at 60 °C.

Sample Preparation

Prior to material blending and cure, Epon 828 was degassed for 24 hours under vacuum at 75 °C. The functional equivalent weight of Epon 828 (DGEBA) was determined using the ASTM D162-97 protocols. Amine equivalent weights were calculated from data provided by the manufacturer. The procedure for blending the blocked isocyanates is as follows: DGEBA, NMA-b-IPDI, and e-cap-b-IPDI were individually heated to 100 °C before mixing with the epoxy resin. The bis-TEMPO-IPDI additive was mixed with the epoxy resin at 50 °C. After blending, all the formulations were degassed again (albeit only briefly) to remove any gases incorporated during mixing. 2-methyl-1,5-diaminopentane was added at a 1:1 functional equivalent ratio to the epoxy-additive blend and mixed briefly but efficiently. The epoxy-amine-blocked isocyanate blend was partitioned for FT NIR and rheology studies. A 25 minute preparation period was allowed for all samples before simultaneously starting the rheology and NIR analysis to provide the same temporal and temperature history of both samples.

Results

Throughout the reaction, functional group concentrations were measured using the principles of Beer-Lambert's law. Using a fixed path length of 0.2 mm, spectra were acquired in the linear region of utilizing Beer-Lambert's law so that the peak area was directly proportional to concentration. Molar absorptivity coefficients were experimentally determined for each functional group via NIR spectroscopic analysis of the monomer at a known path length and concentration. Table 3 lists the molar absorptivity coefficients determined experimentally for the primary + secondary amine,

primary amine, and epoxide absorption bands. Figure 20 shows the time resolved NIR spectra of DGEBA and 2-methyl-1,5-diaminopentane NIR regions for the overlapping primary + secondary amine and single primary amine and epoxide absorption bands.

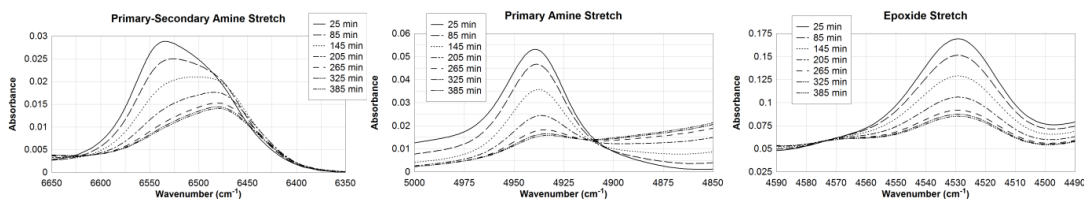


Figure 20. Wavenumber regions monitored for primary+secondary amine, primary amine, and epoxide absorption bands.

Table 3

Molar Absorptivity Values

Absorption Bands	Molar Absorptivity*
Primary + Secondary Amine	1.111
Primary Amine	1.243
Epoxide	0.890

*Units of Molar Absorptivity are $A \cdot \text{kg} \cdot \text{mol}^{-1} \cdot \text{cm}^{-1}$. Variable A is defined as Peak Area.

Experimental procedures were designed to ensure that the temporal and temperature history of the samples in the NIR heat cell and the rheometer forced air convection chamber were identical and that the samples were exposed to 30 °C at the same instant. The first scan was obtained 25 minutes after the reaction was injected into the heat cell. Differences in conversion prior to measurement (Figures 21 – 24) were attributed to the differences in laboratory temperatures during sample preparation. Moreover, the heat cell within the NIR varied in the isothermal temperature by

approximately ± 1 °C throughout the experiment, whereas the rheometer maintained temperature within ± 0.1 °C.

Each of the chemorheological experiments indicated vitrification of the samples prior to infinite molecular weight, expected to occur at $\sim 58\%$ conversion as calculated through Flory's equations.¹ Within this study, it was apparent that two different types of vitrification occurred. Mechanical vitrification occurs at the crossover point between the storage and loss modulus as the elastic nature of the network dominates the rheological properties. However, this condition does not affect the reaction rate with respect to the chain ends because their mobility is not restricted until higher conversions are achieved as evidenced in Figures 21 – 24. Based on these two criteria, we chose to assign vitrification as being achieved when the storage modulus reached its plateau.

Mechanically, there are no further changes in the network. Based on NIR spectroscopy, this point is close to the loss of mobility of the reacting chain ends evidenced by a sharp decrease in epoxide conversion rates. Despite no measurable change in storage modulus, the epoxy-amine reaction continues at lower reaction rates, with crosslink density continuing to increase. It is believed that although chain ends are continuing to react, they are not significant from a force distribution standpoint as the stiffness property is only affected by the lack of cooperative segmental motion at temperatures below the T_g and not the increasing crosslink density. Interestingly, Dean *et al.* reported NIR vitrification data that was consistently lower than rheological values.¹² However, they did not report a correlation between the two vitrification points in their study.

At higher incorporation levels, the blocked isocyanate materials induced plasticization upon network formation and promoted higher degrees of conversion versus

controls at the same time/temperature points as shown in Figures 23 and 24 (conversions ≥ 0.75). The increasing amounts of blocked isocyanates produced a dilution effect on the functional group concentration, resulting in a consistent lower epoxy conversion rate. The data indicates the reactive materials are dormant during these characterization processes and do not affect the epoxy-amine reaction as a competing mechanism (Table 6). This was further supported by a series of stability studies in whereby each additive was combined with DGEBA and held at temperatures of 50 °C and 105 °C for over 24 hours. No conversion of the epoxy groups was detected after 24 hours at elevated temperatures. After several weeks at 105 °C, the DGEBA - NMA-b-IPDI sample had increased in viscosity to the point that the sample could not be placed and measured accurately within the NIR cell. Therefore, at 30 °C, there is very little reaction between the NMA isocyanate derivative and the epoxy resin within the timeframe of the chemorheology study.

Based on NIR stability studies, the single outlier from Figure 22 was questioned and determined to be the result of lower temperature conditions in our NIR heat cell. If the curve is treated as anomalous, the calculated kinetic rate of the remaining curves decreased consistently by $0.0015 \text{ kg mole}^{-1} \text{ min}^{-1}$ for every 5 wt% increase in additive. Thus, incorporating 5 wt% of bis-TEMPO-IPDI decreased the reaction rate by $0.001 \text{ mol kg}^{-1} \text{ min}^{-1}$, whereas 10 wt% of the other two blocked isocyanates decreased the reaction rate by $0.003 \text{ mol kg}^{-1} \text{ min}^{-1}$ in comparison to the control. These reaction rates were calculated using the initial reaction rates in the linear regions of Figures 21-24 prior to vitrification. Compared to the control, the G' and G'' crossover point and times required to reach mechanical plateaus were elongated significantly at increasing blocked-

isocyanate concentrations (Table 5). The results were consistent, and the differences from the controls were attributed to increased plasticization of the epoxy-amine matrix that allowed higher mobility and increased the extent of conversion achievable prior to vitrification.

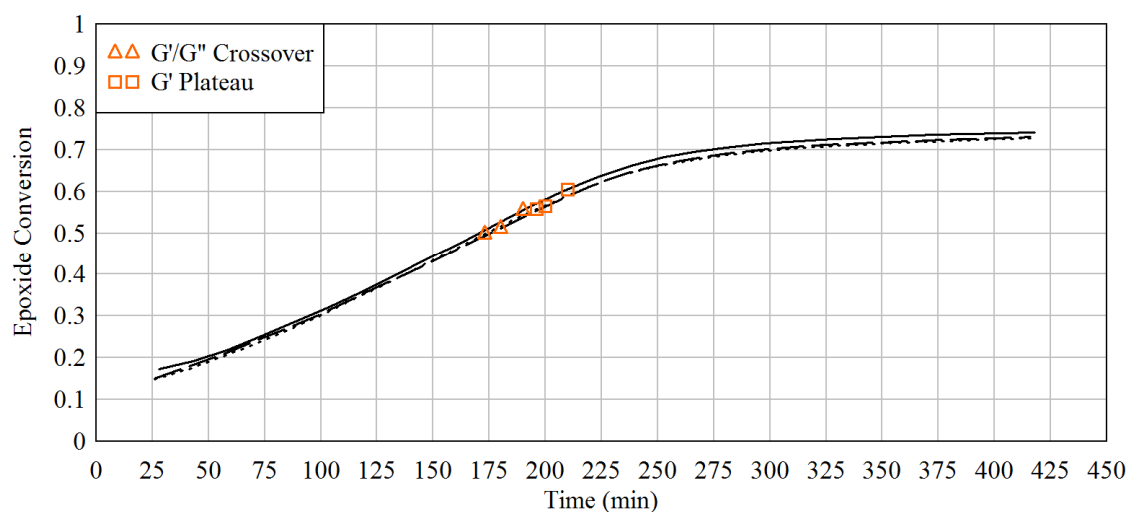


Figure 21. Chemorheological characterization of DGEBA and 2-methyl-1,5-diaminopentane epoxy-amine reaction at 30 °C.

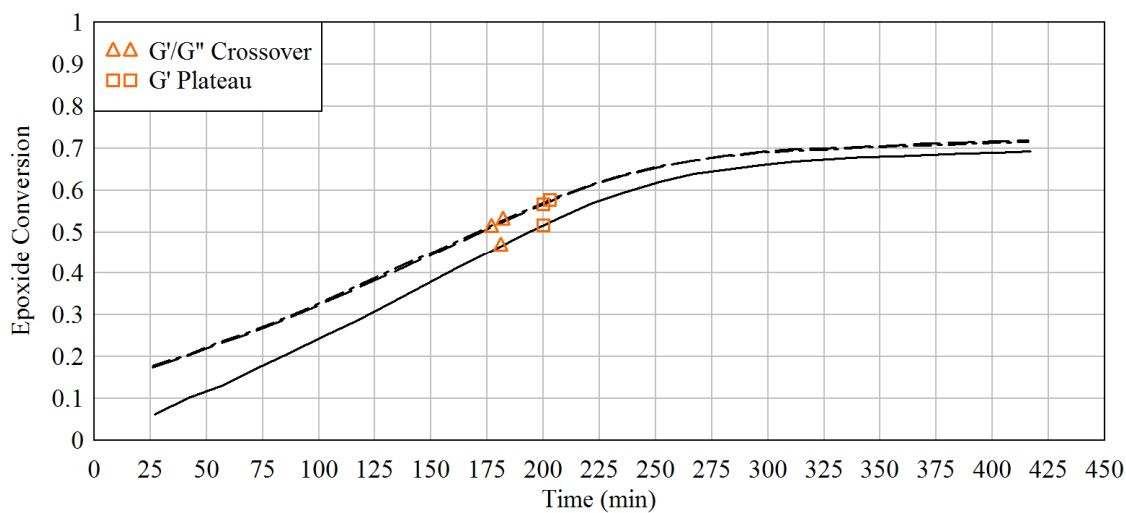


Figure 22. Chemorheological characterization of DGEBA and 2-methyl-1,5-diaminopentane epoxy-amine reaction in the presence of 5 wt% bis-TEMPO-IPDI at 30 °C.

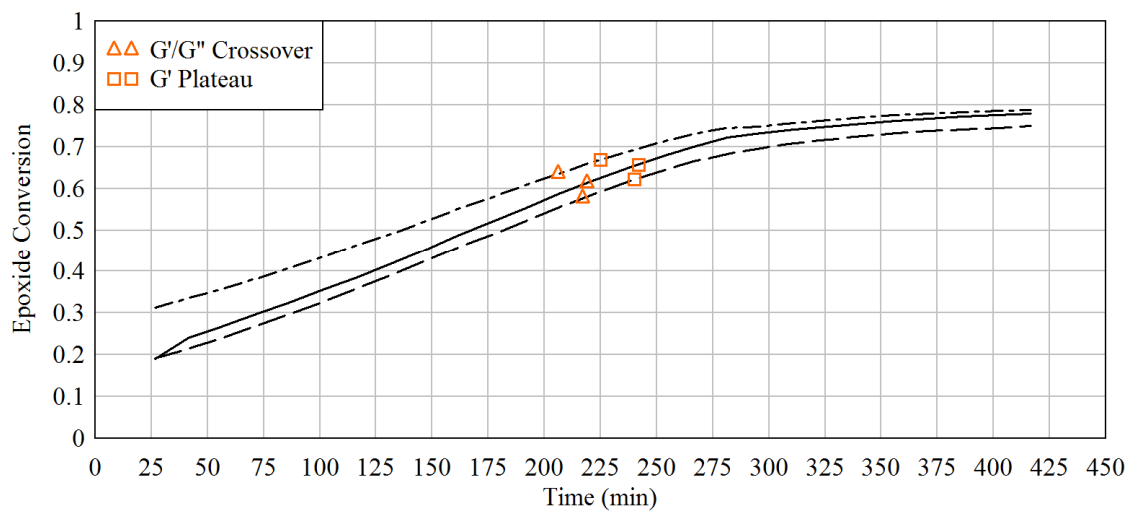


Figure 23. Chemorheological characterization of DGEBA and 2-methyl-1,5-diaminopentane epoxy-amine reaction in the presence of 10 wt% e-cap-b-IPDI at 30 °C.

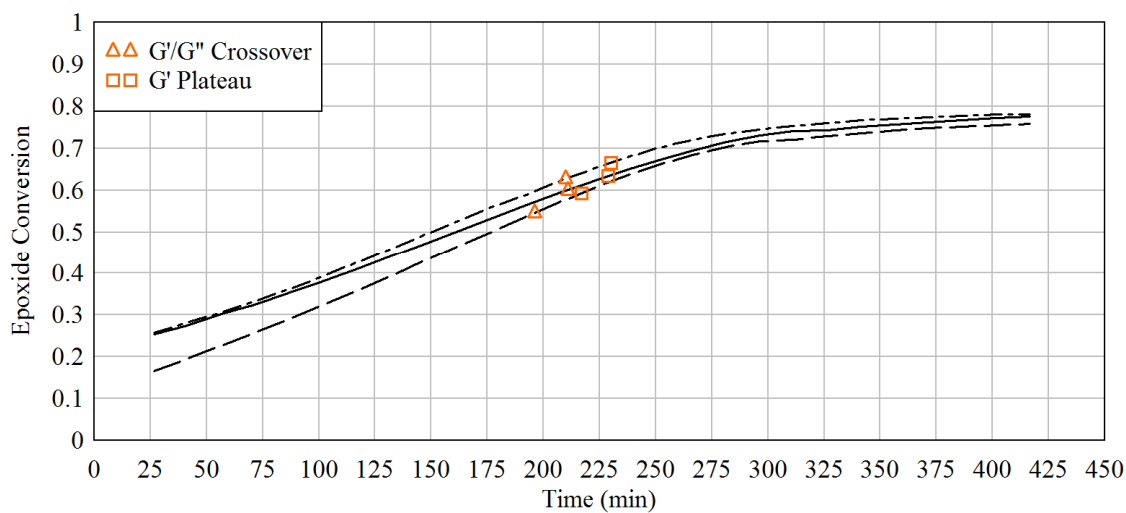


Figure 24. Chemorheological characterization of DGEBA and 2-methyl-1,5-diaminopentane epoxy-amine reaction in the presence of 10 wt% NMA-b-IPDI at 30 °C.

Table 4

Average Pre-vitrification Rates of Epoxide Conversion for DGEBA-2-methyl-1,5-diaminopentane at 30 °C

Material	Rate of Epoxide Reaction ($\text{mol kg}^{-1} \text{min}^{-1}$)
Control	-0.0121 ± 0.0002
5 wt% Bis-TEMPO-IPDI	-0.0110 ± 0.0008
10 wt% e-cap-b-IPDI	-0.0087 ± 0.0006
10 wt% NMA-b-IPDI	-0.0090 ± 0.0007

Note: Control is DGEBA and 2-methyl-1,5-diaminopentane reaction, subsequent entries are wt% added to the reaction mixture.

Table 5

G'/G'' Crossover Time Points in Dynamic Rheology Data at 30 °C

Material	G'/G'' Crossover (min)	Epoxide Conversion
Control	181 ± 9	0.521 ± 0.029
5 wt% Bis-TEMPO-IPDI	180 ± 3	0.502 ± 0.032
10 wt% e-cap-b-IPDI	214 ± 7	0.608 ± 0.030
10 wt% NMA-b-IPDI	206 ± 8	0.591 ± 0.041

Note: Control is DGEBA and 2-methyl-1,5-diaminopentane reaction, subsequent entries are wt% added to the reaction mixture.

Table 6

G' Plateau Time Points in Dynamic Rheology Data at 30 °C

Material	G' Plateau (min)	Epoxide Conversion
Control	202 ± 7	0.575 ± 0.026
5 wt% Bis-TEMPO-IPDI	201 ± 2	0.553 ± 0.033
10 wt% e-cap-b-IPDI	236 ± 9	0.649 ± 0.025
10 wt% NMA-b-IPDI	225 ± 7	0.631 ± 0.036

Note: Control is DGEBA and 2-methyl-1,5-diaminopentane reaction, subsequent entries are wt% added to the reaction mixture.

Conclusions

Compared to the control (no additive), variations in gel points and ultimate epoxy conversion were observed in systems containing blocked isocyanates based on *N*-methyl aniline and e-caprolactam. However, no significant variation was detected with the 4-hydroxy TEMPO blocked isocyanate. The kinetic rate of the epoxy-amine reaction,

measured by NIR spectroscopy, decreased by $0.0015 \text{ mol kg}^{-1} \text{ min}^{-1}$ for every 5 wt% of additive within the matrix.

Chemorheological techniques confirmed the chemical and mechanical compatibility of the epoxy-amine matrix system with blocked isocyanate additives and nitroxyl radicals. Reduction in kinetic rates of the e-cap-b-IPDI and NMA-IPDI formulations are consistent with dilution effects from higher additive loadings. These formulations also exhibited a plasticization effect due to the presence of small molecules not directly participating in network formation. The observed plasticization effects elicited higher levels of conversion (supported by both FT NIR spectroscopic and rheological data) in systems containing NMA-IPDI and e-cap-b-IPDI by postponing vitrification. The system containing bis-TEMPO-IPDI did not display a statistically significant change in gelation time when compared to the control but did exhibit a reduction in kinetic rates in the isothermal regime studies. The consistent loss of reaction rates with increasing additive concentration suggests that the effect on kinetic rate is due to decreasing concentration of reacting functional groups and was not attributed to the presence of a competing mechanism.

REFERENCES

1. H.-P. Hu, R.D. Gilbert & R.E. Fornes. Chemical Modification of Cured MY720/DDS Epoxy Resins Using Fluorinated Aromatic Compounds to Reduce Moisture Sensitivity. *Journal of Polymer Science: Part A: Polymer Chemistry* **25**, 1235-48, (1987).
2. S.S. Sankar, S.V. Lonikar & R.D. Gilbert. Solid-State CPMAS ¹³C-NMR Studies of the Reaction of an Epoxy Resin with Masked Isocyanates. *Journal of Polymer Science: Part B: Polymer Physics* **28**, 293-302, (1990).
3. S.V. Lonikar, N. Rungsimuntakul, R.D. Gilbert & R.E. Fornes. The Effect of Masked Isocyanates on the Moisture Absorption of MY 720/DDS Epoxy Resin. *Journal of Polymer Science: Part A: Polymer Chemistry* **28**, 759-75, (1990).
4. M. Abdalla, D. Dean, P. Robinson & E. Nyairo. Cure behavior of epoxy/MWCNT nanocomposites: The effect of nanotube surface modification. *Polymer* **49**, 3310-17, (2008).
5. C.E. Corcione, M. Frigione, A. Maffezzoli & G. Malucelli. Photo- DSC and real time- FT-IR kinetic study of a UV curable epoxy resin containing o-Boehmites. *European Polymer Journal* **44**, 2010-23, (2010).
6. R. Fernandez, B. Fernandez D'arlas, P.A. Oyanguren & I. Mondragon. Kinetic studies of the polymerization of an epoxy resin modified with rhodamine B. *Thermochimica Acta* **493**, (2009).
7. P. Musto, E. Martuschelli, G. Ragosta, P. Russo & P. Villano. Tetrafunctional Epoxy Resins: Modeling the Curing Kinetics Based on FTIR Spectroscopy Data. *Journal of Applied Polymer Science* **74**, 532-40, (1999).
8. G. Li, Z. Huang, P. Li, C. Xin, X. Jia, B. Wang, Y. He, S. Ryu & X. Yang. Curing kinetics and mechanisms of polysulfone nanofibrous membranes toughened epoxy/amine systems using isothermal DSC and NIR. *Thermochimica Acta* **497**, 27-34, (2010).
9. M. Pramanik, E.W. Fowler & J.W. Rawlins. Cure kinetics of several epoxy-amine systems at ambient and high temperatures. *J. Coat. Technol. Res.* **11**, 143-57, (2014).
10. R. Dhavalikar & M. Xanthos. Monitoring the Evolution of PET Branching Through Chemorheology. *Polymer Engineering and Science* **44**, (2004).
11. J. Mijovic, S. Andjelic, B. Fitz, W. Zurawsky, I. Mondragon, F. Bellucci & L. Nicolais. Impedance Spectroscopy of Reactive Polymers. 3. Correlations Between Dielectric, Spectroscopic, and Rheological Properties During Cure of a

- Trifunctional Epoxy Resin. *Journal of Polymer Science: Part B: Polymer Physics* **34**, 379-88, (1996).
12. K. Dean, W.K. Cook, L. Rey, J. Galy & H. Sautereau. Near-Infrared and Rheological Investigations of Epoxy-Vinyl Ester Interpenetrating Polymer Networks. *Macromolecules* **34**, 6623-30, (2001).
 13. E. Mounif, V. Bellenger, P. Mazabraud, F. Nony & A. Tcharkhtchi. Chemorheological Study of DGEBA/IPD System for Reactive Rotational Molding (RRM). *Journal of Applied Polymer Science* **116**, 969-76, (2010).
 14. C.M. Sahagun. *Molecular Network Development of a Thermosetting Epoxy-Amine Polymer*. The University of Southern Mississippi. (2012).
 15. C.M. Sahagun & S.E. Morgan. Thermal Control of Nanostructure and Molecular Network Development in Epoxy-Amine Thermosets. *ACS Applied Materials & Interfaces* **4**, 564-72, (2012).

CHAPTER IV
FATIGUE OF A GLASSY EPOXY THERMOSET WITH HOMOLYTIC CHAIN
SCISSION PROBES

Introduction

In Chapter II, bis-TEMPO-IPDI was synthesized from 4-hydroxy-TEMPO and isophorone diisocyanate, and the nitroxyl radical functionality was shown to be retained through titration experiments. Thermogravimetric analysis experiments have confirmed that the molecule is thermally stable to 150 °C. In Chapter III, it was demonstrated that BT-IPDI and molecules possessing urethane functional groups could be incorporated without affecting the kinetics of the DGEBA/2-methyl-1,5-diaminopentane epoxy-amine reaction at loading levels exceeding 5 wt%.

Xia measured diminishing properties of glassy epoxy-amine thermosets *in situ* with fatigue studies.¹⁻⁶ However, no studies have reported the underlying cause of property diminishment and subsequent failure with fatigue. The goal of this study is to induce mechanical degradation through fatigue and determine if it is accompanied by molecular degradation. Figure 25 demonstrates graphically the purpose of using nitroxyl radicals and detection by EPR spectroscopy. In this chapter, BT-IPDI was incorporated into DGEBA - 2-methyl-1,5-diaminopentane matrices and subject to fatigue experiments to detect if mechanical forces cause homolytic chain scission.

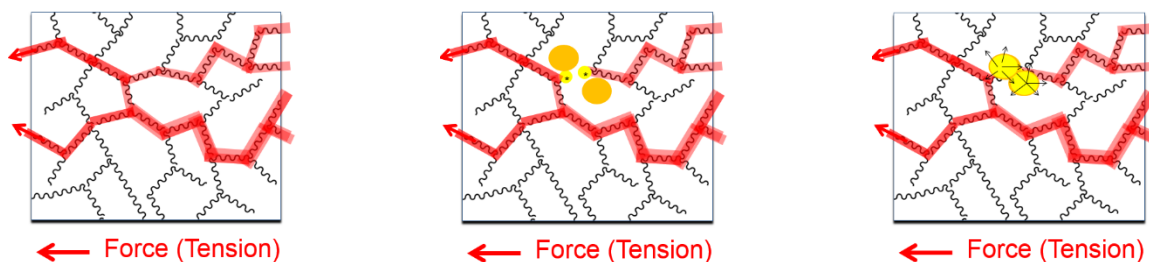


Figure 25. Illustration depicting chain scission resulting from force. The left figure depicts the force distribution throughout the thermoset polymer chains. The central figure depicts the homolytic cleavage of a bond near two nitroxyl probes represented by orange circles. The right figure depicts the reaction of the nitroxyl probes with the chain scission radicals and producing a detectable signal.

Materials

Materials used in this study are DGEBA and 2-methyl-1,5-diaminopentane as shown in Scheme 1 of Chapter II. Epon 828 (DGEBA) was degassed under vacuum for approximately 6 hours prior to introduction of amine. To introduce nitroxyl probes, BT-IPDI was incorporated through volumetric addition of BT-IPDI/acetonitrile solution to the DGEBA at 0.005 wt% loading of final samples. Acetonitrile (boiling point 82 °C) was removed from DGEBA by heating the sample to 80 °C under vacuum overnight. The DGEBA blend was then measured gravimetrically to ensure that the solvent has been removed completely. The DGEBA / BT-IPDI blend and 2-methyl-1,5-diaminopentane were mixed together at a molar ratio of 1:1 based on epoxide to amine hydrogens. After thorough mixing in a non-contact Flacktek[®] mixer, the samples were further degassed via sonication for 10 minutes before being injected into molds as shown in Figures 26 and 27.

Nitroxyl Loading Justification

The method discussed in this paper involves subtraction of the resulting signal from the original signal. Because a low population of chain scission events were

expected, a low nitroxyl concentration was employed to ensure the number of nitroxyls reacting would be a significant fraction of the existing population enabling easy detection of the loss of signal. It could be argued that using such a small concentration would minimize the detection potential. However, it is hypothesized that larger populations of nitroxyl radicals would result in an even smaller chance of successful detection.

Sample Preparation

The dimensions of the EPR solid state tissue holder limited the sample size that could be evaluated. Composed completely of quartz, the holder encases samples measuring approximately 7 mm x 23 mm x 0.5 mm. Molds were designed and used to cast samples having dimensions of 6 mm x 20 mm x 0.5 mm. However, defects in sample shape can exert critical influence at such small dimensions and induce extensive variation in the experimental results. To ensure dimensional consistency, samples for mechanical testing were prepared using reaction injection molding. Machining of samples to the appropriate dimension was avoided as it could interfere with the measurement of chain scission events.

The reaction injection molding setup (Figure 26) was composed of a syringe pump, Tygon[®] tubing, Y splitters, and 18 gauge syringe needles. The needles were inserted into silicone molds and also into the injection port (object 2 in Figure 27). To facilitate release from the silicon molds, a dry film mold release agent was used. After the monomer mixture was degassed via sonication, it was loaded into a syringe and pumped into the silicone mold. The syringe needles were angled downwards into the mold so that any trapped air would be caught at the tubing inverse points. The rate of volume addition was programmed to fill the mold under constant pressure up to the

vitrification time point (3 hours). Pumping through vitrification and overfilling the molds minimized the effects of volume shrinkage from epoxy conversion. This process minimized artifacts such as bubbles and uneven surfaces from meniscus and levelling type effects.

The mold was held together using C-clamps and a specially devised torque wrench that avoided any mold distortion due to over-tightening of the clamps. A torque setting of approximate 5-7 in-lb. was found to be ideal. The mold half was composed completely of silicone resin with a release paper backing that was then held together like a sandwich using flat metal backings and C-clamps (Figure 26).

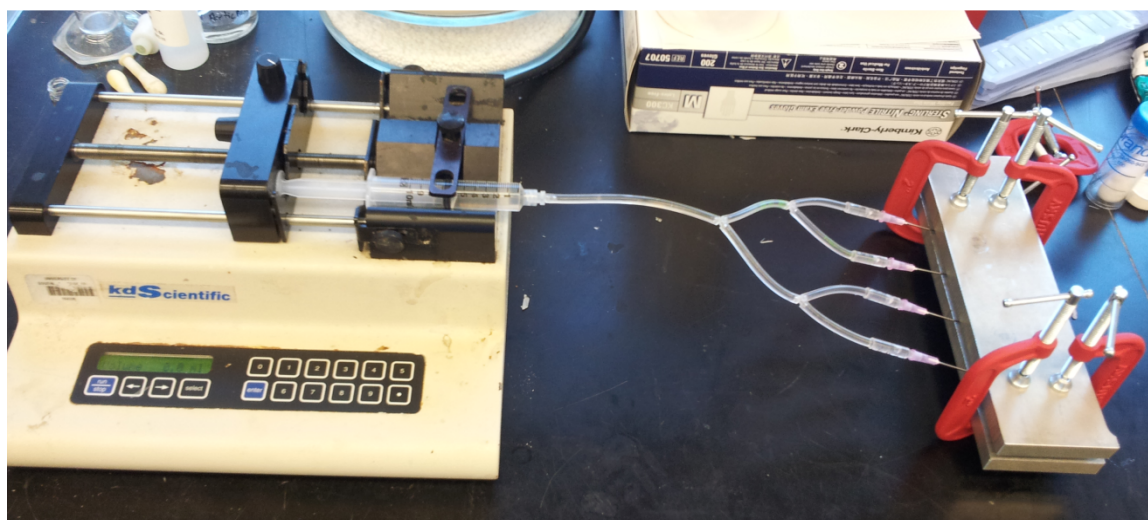


Figure 26. Reaction injection molding setup for sample casting. Preparation and detection of degradation and chain scission events in epoxy-amine networks using a profluorescent nitroxide probe, by K.F. Fazende, 2013, The University of Southern Mississippi, p. 9. Reprinted with permission from the author.⁷

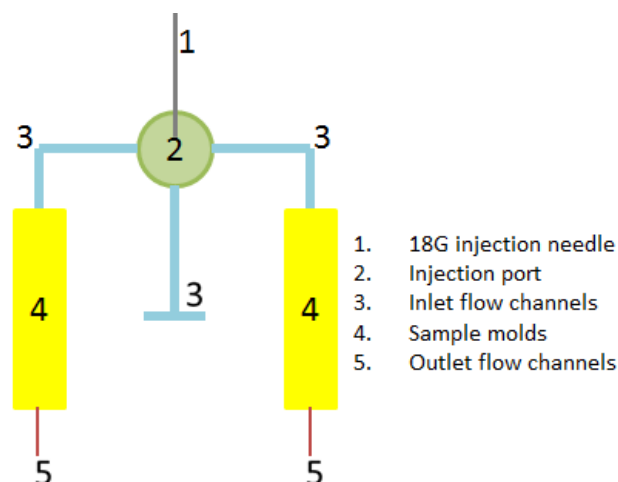


Figure 27. Sample injection depiction and mold layout. Sample molds (4) dimensions were width 6 mm, length 20 mm, and thickness 20 mm. Preparation and detection of degradation and chain scission events in epoxy-amine networks using a profluorescent nitroxide probe, by K.F. Fazende, 2013, The University of Southern Mississippi, p. 9. Reprinted with permission from the author.⁷

The epoxy samples were then allowed to vitrify overnight and post-cured in the morning. Based on NIR data from Chapter III, the epoxy conversion was approximately 70% before post-curing. The samples were post-cured in a nitrogen atmosphere forced air convection oven at 60 °C for 85 minutes followed by 120 °C for 145 minutes. The nitrogen atmosphere is used to avoid oxidative degradation of the nitroxyl radicals. The samples were then removed from the mold and weighed on an analytical balance. The samples were then thermally annealed under nitrogen purge according to Figure 28 to erase any aging effects, remove absorbed atmospheric water, and ensure consistent thermal histories between samples. Since the DGEBA - 2-methyl-1,5-diaminopentane samples were measured to absorb up to 0.5 wt% of water over a 24 hour period, all mechanical testing was performed immediately after the thermal cycle in Figure 28.

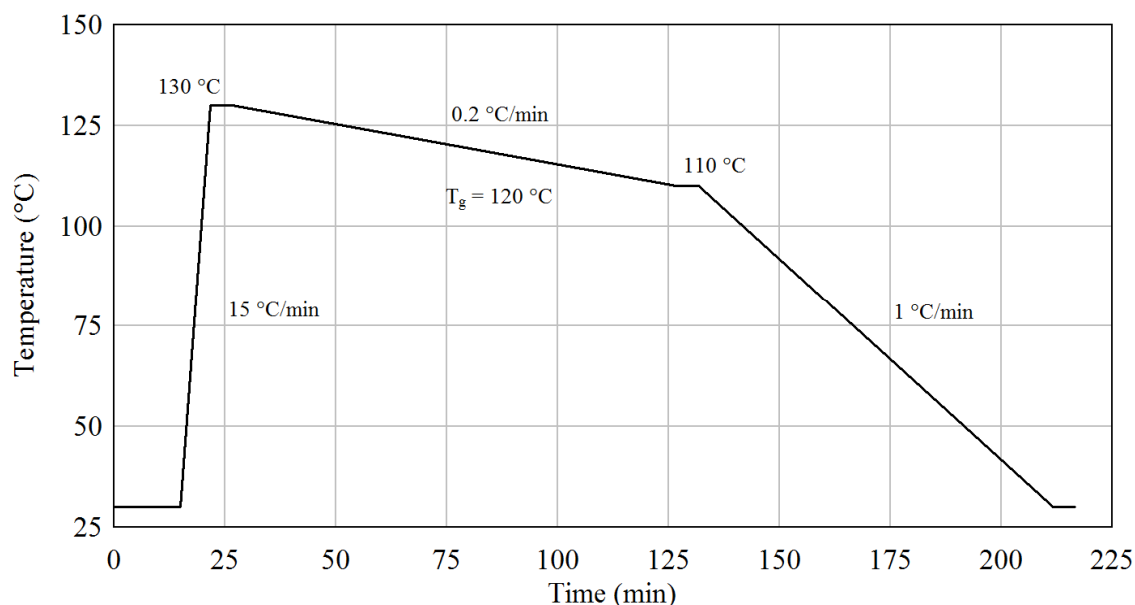


Figure 28. Thermal annealing temperature ramps for samples.

Experimental

Monotonic tensile and cyclic tensile fatigue testing was performed on the BOSE ElectroForce[®] 3330 Series II Test Instrument. This separate motor transducer (SMT) system is capable of monotonic testing as well as dynamic oscillation up to 100 Hz with a load envelope of ± 3000 N. The BOSE system is capable of being operated in controlled stress or controlled strain modes. Fatigue experiments were carried out using a sinusoidal application of tensile force using an R value of 0.1 as shown in Equation 9. Experiments were conducted at a frequency of 10 Hz to avoid strain induced heating at higher frequencies.

$$R = \frac{Stress_{min.}}{Stress_{max.}}$$

Equation 9. Stress ratio equation.

Quantitative EPR spectroscopy was performed using a Bruker EMX^{Micro} X-band spectrometer using a quartz solid tissue holder at ambient temperature. The following

EPR instrumental settings were used to collect each spectrum: microwave power of 0.63 mW, receiver gain of 5020, frequency of 9.82 GHz, modulation amplitude of 2 gauss, modulation frequency of 100 KHz, conversion time of 20.48 msec, time constant of 20.48 msec, and signal averaging of 4 scans.

EPR Spectra of Nitroxyl Radicals

In this research study, a primary method was analysis of EPR spectra, specifically of nitroxyl radicals. Only radicals (paramagnetic species) produce signals within EPR experiments. The line splitting pattern is determined by the quantum number of the coupling nuclei, in this case, for nitroxyl radicals, it would be equal to one, the quantum number for ^{14}N . The number of observed spectral lines will be equal to L in Equation 10.⁸ The number of hyperfine splittings, L , is equal to 2 times the number of adjacent nuclei, n , times the quantum number I .

$$L = 2 \times n \times I + 1$$

Equation 10. Number of hyperfine splittings predicted by the Hartman equation.²

For a nitroxyl radical, the active radical is the oxygen atom, which is covalently bonded to nitrogen. The nitrogen atom has a quantum number of one, which, based on the above equation, the expected number of hyperfine lines to be observed is then three. This can be clearly shown in the solution spectra in Figure 29. The characteristic shapes of the splitting pattern can change based upon the local environment of the nitroxyl radical. In NMR, it is well known that the degree of motion that a nuclei possesses affects the shape and broadness of the peak. To a similar degree, the EPR spectra is affected as well, as shown in the solid state spectra in Figure 29. These two spectra are examples of nitroxyl radicals in different environments. However, the concentration of the species are different. Therefore, the signal to noise differences evident within the

spectra should be ignored. Within the context of this study, a quantitative measurement of population of radicals is important. It is not critical at this point to spin count or know the relationship between EPR intensity and exact radical concentration. It is, however, critical in that the EPR intensity is linearly proportional to radical population.

Quantitative measurement in EPR is obtained through low power usage of microwave radiation and low concentration of radical species. For more detail on conducting quantitative EPR experiments, the reader is referred to Eaton *et al.*⁹

The ideal method of measuring changes of the spectra in reference to change in population would be to double integrate the resulting spectra to determine the area under the curve. This would be the most accurate assessment of population. Double integration is necessary because the EPR spectra in Figure 29 is the first derivative of the EPR signal output. Double integration is necessary to remove the first derivative operation and then to integrate to determine the area under the curve. However, the low concentration of radicals used in this experiment due to baseline and signal to noise makes double integration inaccurate. Therefore, signal intensity of the central peak for the nitroxyl radicals will be used to assess population changes. This procedure is not reported in literature, but due to the experimental conditions and design, we believe it provides the most accurate assessment of population changes within the context of these experiments.

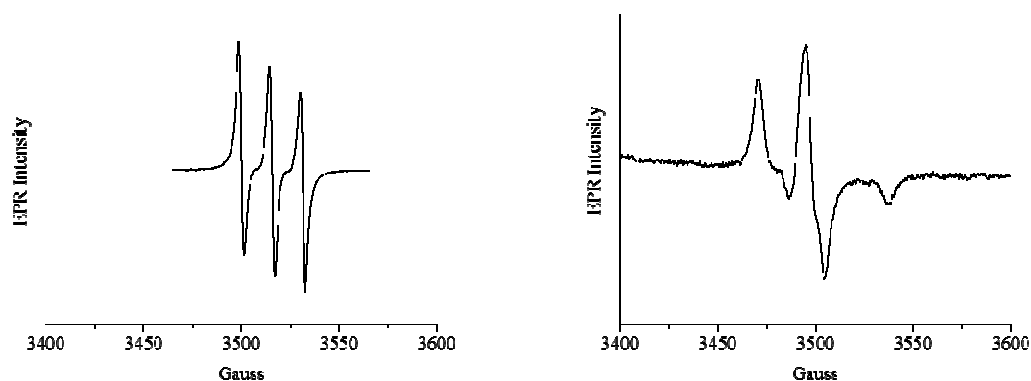


Figure 29. Examples of EPR spectra of nitroxyl radicals in solution and solid state. First spectrum on the right represents a solution environment, while the spectrum on the left environment pertains to a glassy solid (epoxy).

The x-axis in the spectra of Figure 29 is expressed in units of Gauss. This is a unit of magnetic field strength. In NMR, field strength is held constant by a superconducting magnet suspended in liquid helium while multiple frequencies of radio wavelengths is emitted into the sample. In continuous wave EPR, the emission frequency, which is microwave wavelengths, is held constant and the magnetic field strength is swept. Once the appropriate field strength is reached, absorption of the microwaves occurs and signal is produced.

Experimental Design of 50% UTS Experiments

Samples were synthesized and cast through reaction injection molding as previously described. This experiment will study two sample conditions, control and fatigue. Nitroxyl radicals were incorporated through using BT-IPDI at a loading level of 0.005 wt% as previously described. The samples were thermally annealed as shown in Figure 28. The ultimate strength of the materials was determined and shown in Table 7 through destructive testing of three control samples.

Table 7

Mechanical Properties of 50% UTS Controls

Strain-at-Break	Force-at-Break (N)	Modulus (GPa)
0.138	217	1.417
0.128	235	1.525
0.117	222	1.459

The average weight of the samples was 70.5 ± 3 mg, and the experimental design is shown in Figure 30. Both control and test samples were measured via EPR before being subject to fatigue. The fatigue test group was then exposed to 50% UTS sinusoidal force at a frequency of 10 Hz for 10,000 cycles using the BOSE Electroforce 3300 N. Experimental parameters were stress ratio (R) of 0.1 (Equation 9), force values of $11 N_{\min}$ and $115 N_{\max}$, and a sample gauge length of 8 mm. After the fatigue experiment, the samples were stressed to break at a loading rate of 2 N/sec to determine the resulting force-at-break. Most of the samples endured the fatigue experiment. However, some samples did fail from the 50% UTS fatigue stress input. The weights of the fatigue samples were recorded to account for any loss of signal due to fractured specimens. The control samples were exposed to the ambient temperature and atmosphere within the lab but were not subject to fatigue or stress-to-break. Both the fatigue test samples and control samples were then evaluated via EPR spectroscopy to determine any change in the population of nitroxyl radicals resulting from mechanical force input.

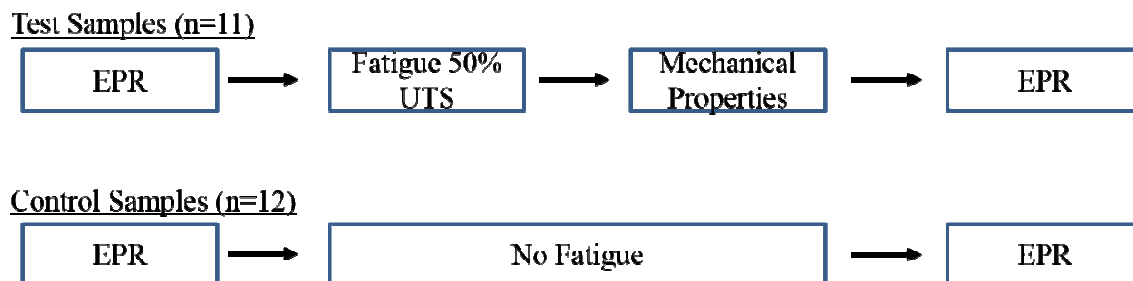


Figure 30. 50% UTS experimental design depiction.

The data shown in the figures and tables to follow encompass four trials composed each of three control samples and three fatigue samples that were analyzed through quantitative EPR spectroscopy with the exception of trial four in which only two fatigue samples were tested due to lack of sample availability. Trial one data are shown in Figure 31 and Table 8, data for trial two are found in Figure 32 and Table 9, Figure 33 and Table 10 contain data for trial three, and trial four data are depicted in Figure 34 and Table 11. Samples that were broken due to fatigue cycles are listed in the tables as “Fatigue Break.”

50% UTS Fatigue Trials Results

50 % UTS 10,000 Cycles Trial One

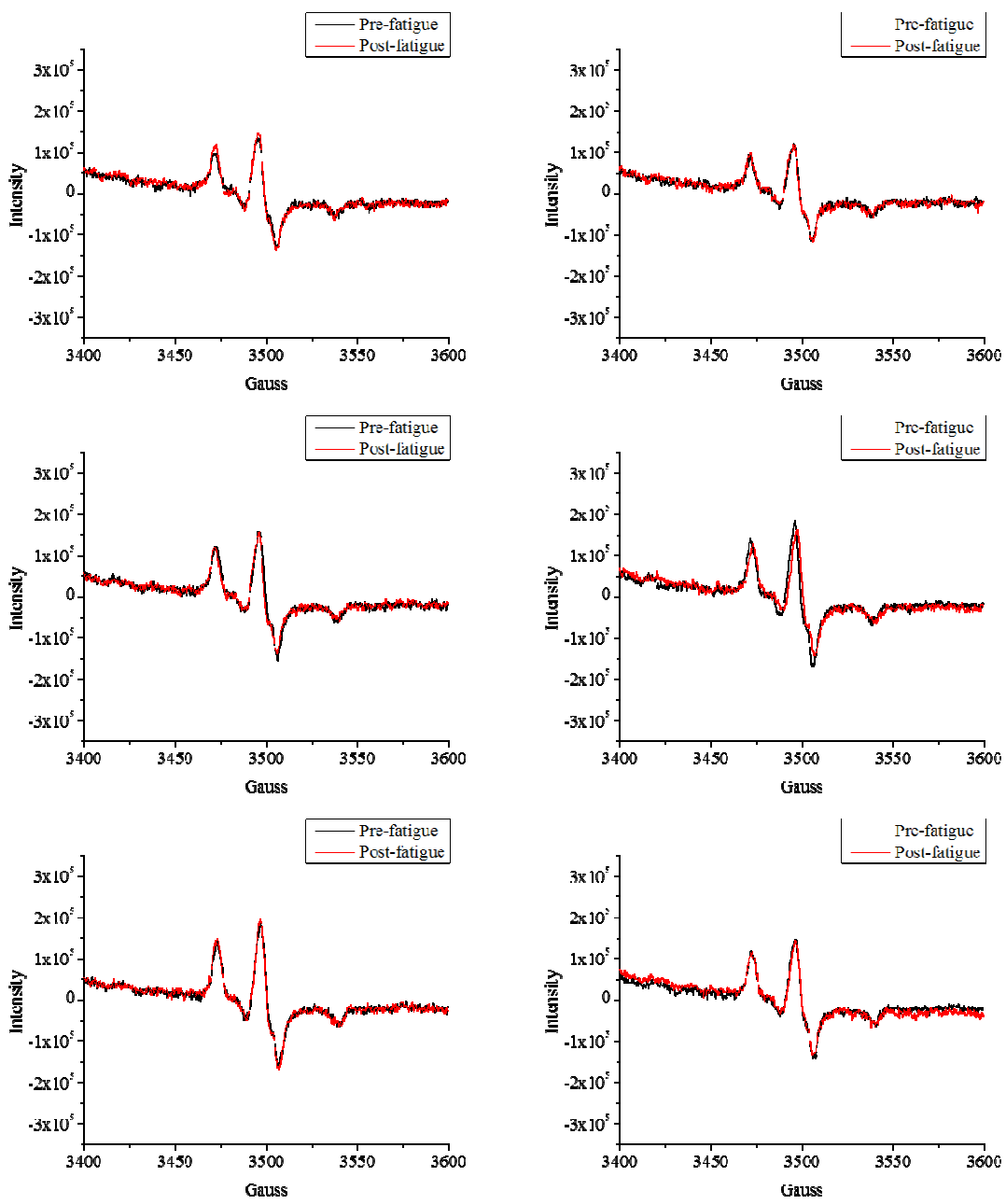


Figure 31. Trial one EPR intensity measurements for control and fatigue conditions before and after treatment. Graphs in left column are control conditions and graphs in right column are fatigue conditions.

Table 8

Trial One Residual Strength Properties at 50% UTS 10,000 Cycles

Strain-at-Break	Force-at-Break (N)	Modulus (GPa)	Δ Weight (mg)
0.162	242	1.532	-1.489
0.150	220	1.425	-0.934
0.133	238	1.569	-4.273

50 % UTS 10,000 Cycles Trial Two

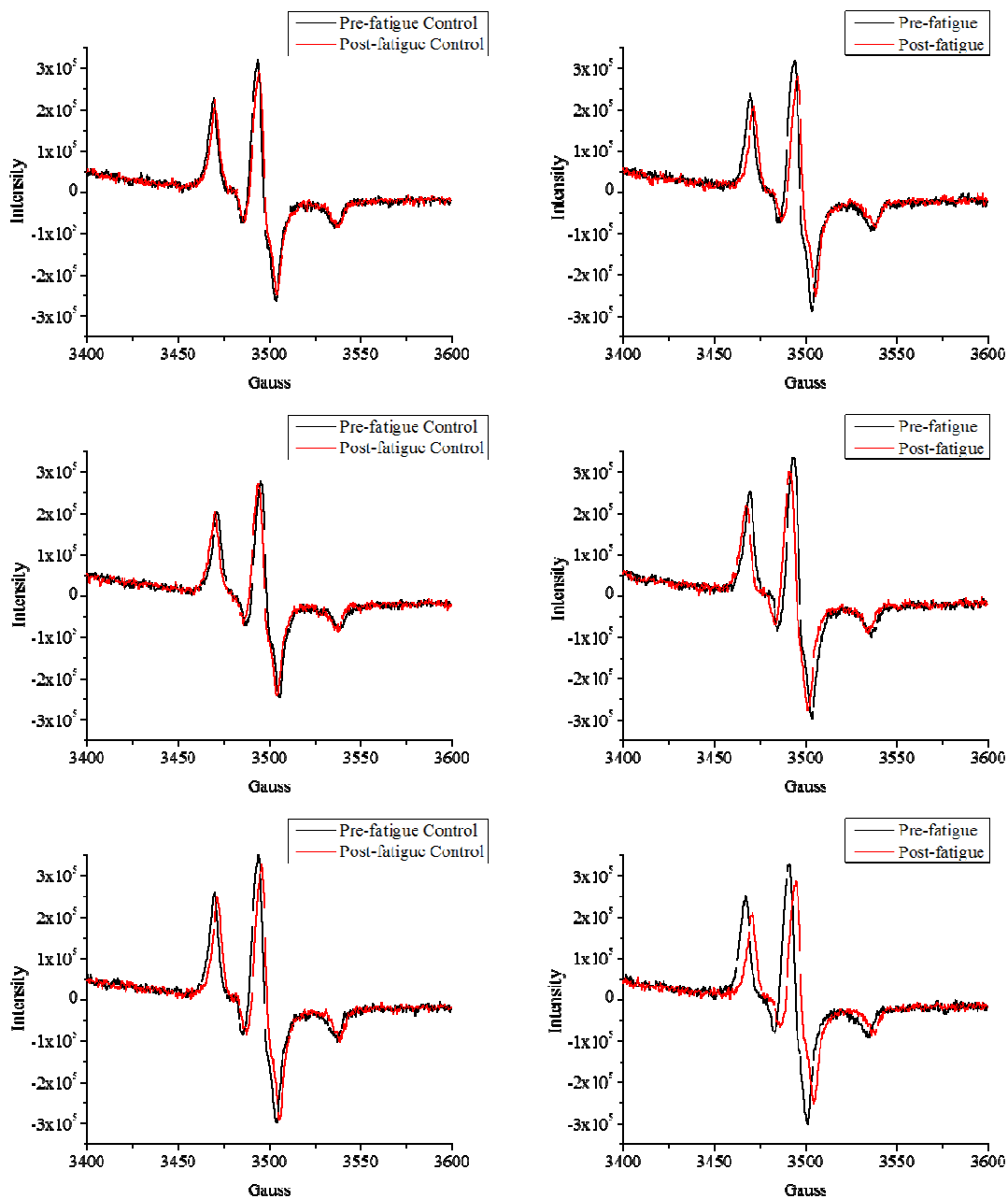


Figure 32. Trial two EPR intensity measurements for control and fatigue conditions before and after treatment. Graphs in left column are control conditions and graphs in right column are fatigue conditions.

Table 9

Trial Two Residual Strength Properties at 50% UTS 10,000 Cycles

Strain-at-Break	Force-at-Break (N)	Modulus (GPa)	Δ Weight (mg)
Fatigue Break	Fatigue Break	Fatigue Break	-0.962
0.115	209	1.480	-1.937
0.082	207	1.555	-0.765

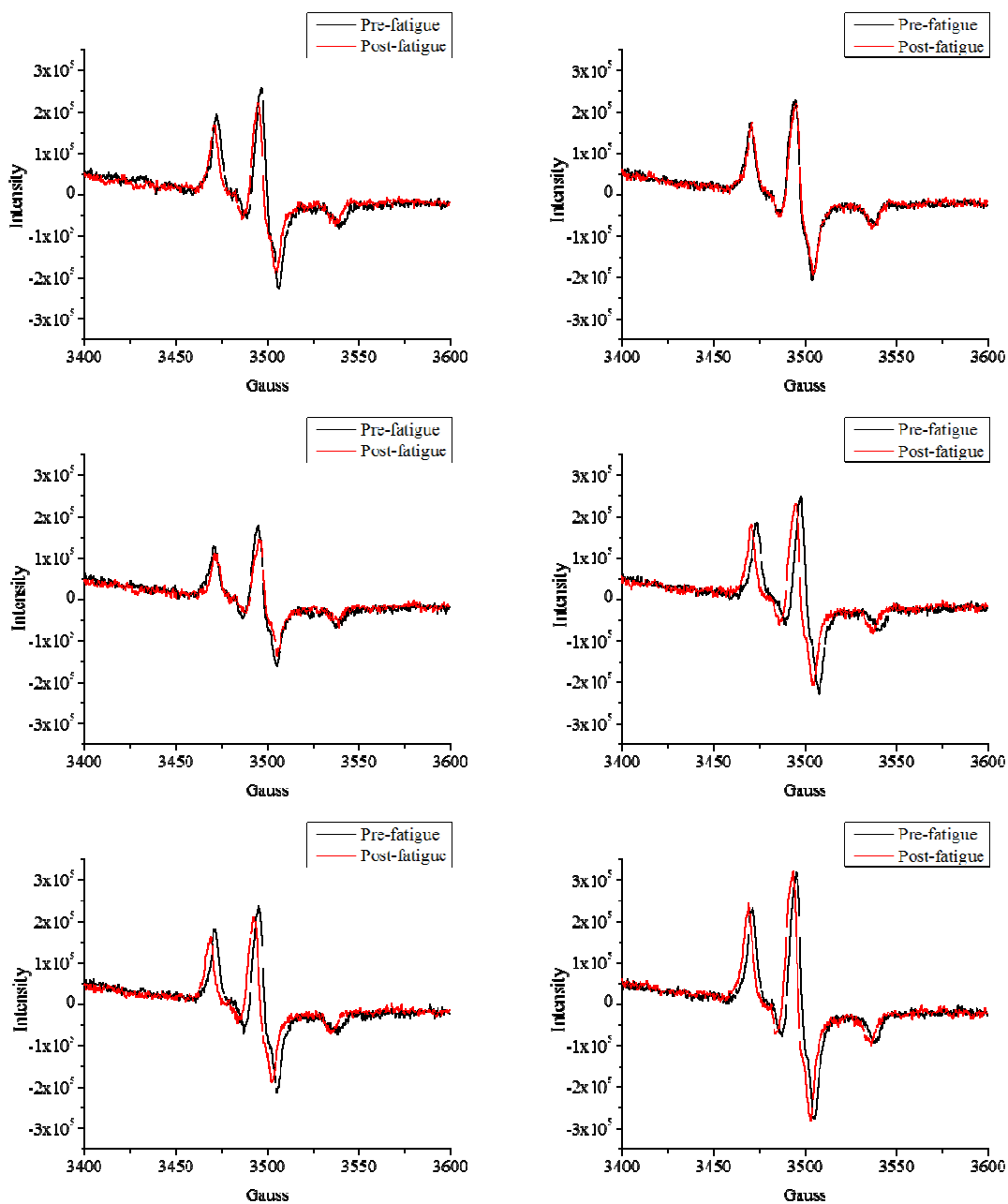
50 % UTS 10,000 Cycles Trial Three

Figure 33. Trial three EPR intensity measurements for control and fatigue conditions before and after treatment. Graphs in left column are control conditions and graphs in right column are fatigue conditions.

Table 10

Trial Three Residual Strength Properties at 50% UTS 10,000 Cycles

Strain-at-Break	Force-at-Break (N)	Modulus (GPa)	Δ Weight (mg)
0.115	222	1.479	+0.081
Fatigue Break	Fatigue Break	Fatigue Break	+0.084
0.168	239	1.529	-0.649

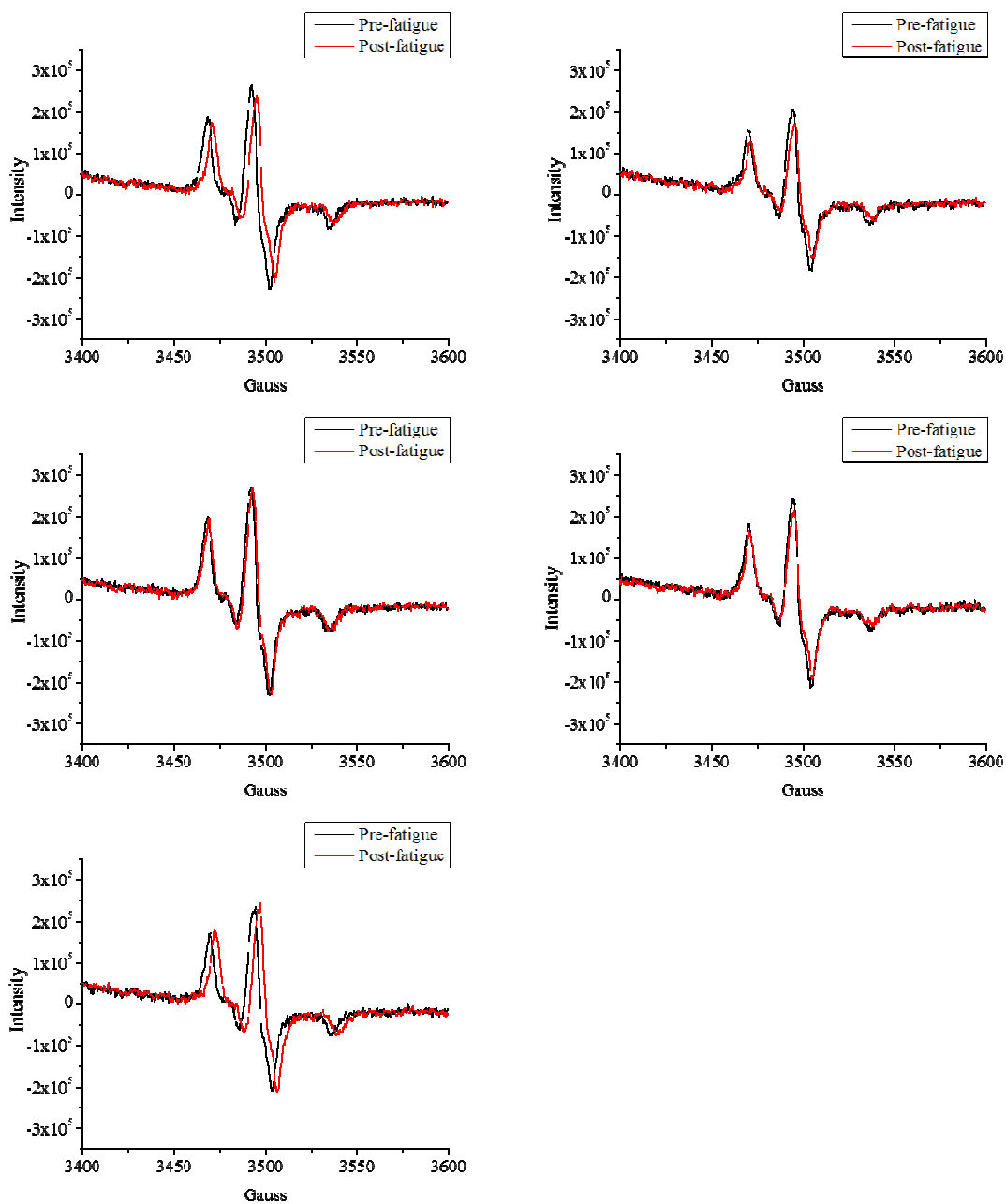
50 % UTS 10,000 Cycles Trial Four

Figure 34. Trial four EPR intensity measurements for control and fatigue conditions before and after treatment. Graphs in left column are control conditions and graphs in right column are fatigue conditions.

Table 11

Trial Four Residual Strength Properties at 50% UTS 10,000 Cycles

Strain-at-Break	Force-at-Break (N)	Modulus (GPa)	Δ Weight (mg)
0.095	202	1.535	+0.074
0.0501	160.2	1.526	-1.140

50% UTS Discussion

Trials one through four show EPR spectra that did not exhibit any change based on fatigue inputs or fracture. While some samples exhibited loss in properties from fatigue, none showed a decrease in EPR signal indicating that the nitroxyl radical concentration remained the same within the samples. In EPR, the radical concentration is directly proportional to the signal area or intensity if the line shape remains constant. Figure 35 displays the starting intensities of the control prior to the time allotment of the fatigue experiment. All 12 samples are shown with initial and post fatigue EPR signal intensities.

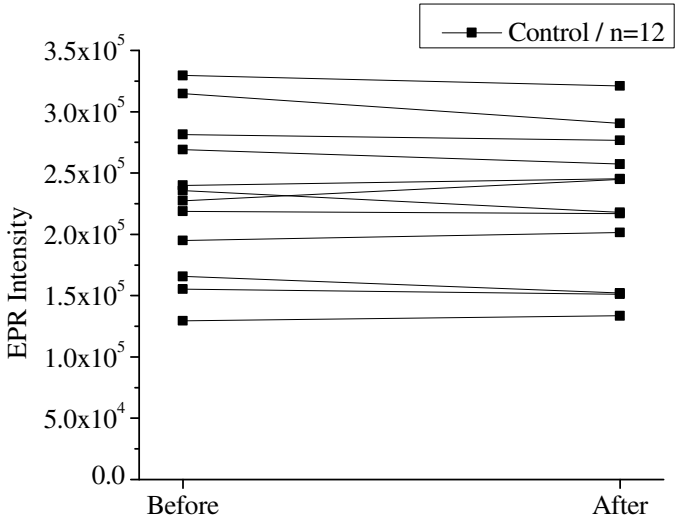


Figure 35. EPR intensity of control samples from trials 1-4 before and after fatigue time allotment normalized to q-value.

Figure 36 shows the same graphical configuration for the 11 fatigue samples. The EPR intensity was measured before and after fatigue treatment at 50% UTS – 10 Hz.

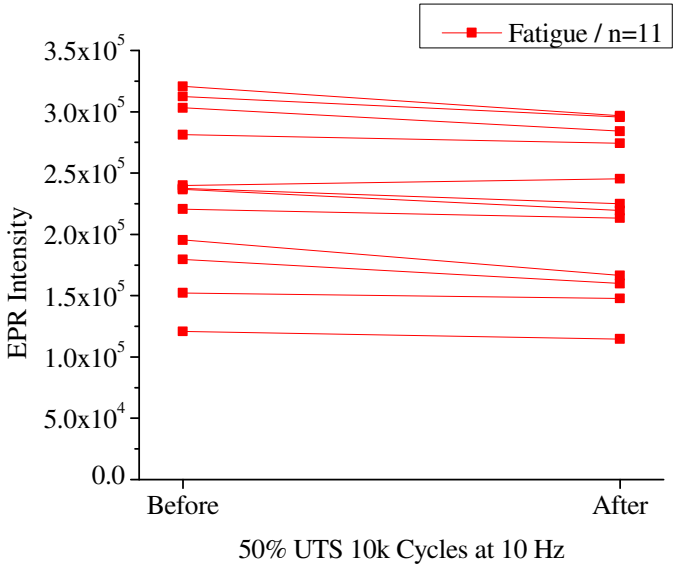


Figure 36. EPR Intensity of fatigue samples from trials 1-4 before and after fatigue treatment normalized to weight and q-value.

Figures 35 and 36 are plotted with the raw data of the EPR experiment. Figure 37 shows the EPR average intensities normalized to sample weight and q-value for both the control and the fatigue trials.

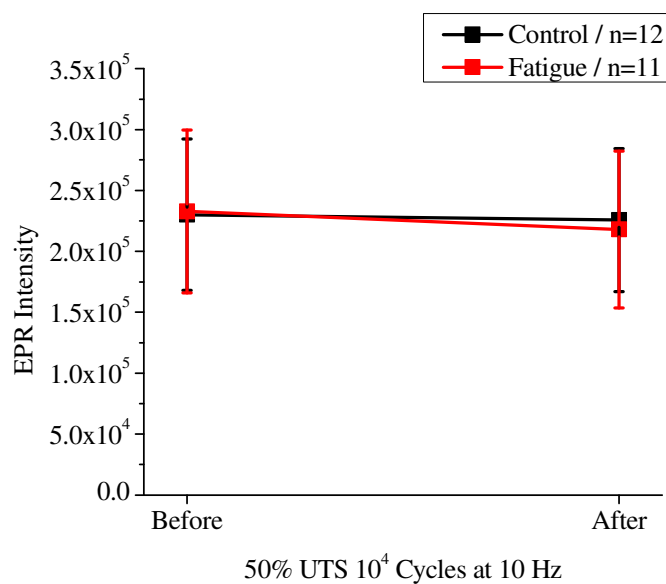


Figure 37. Average EPR intensity of control and fatigue samples from trials 1-4 before and after fatigue treatment normalized to weight and q-value.

In Figure 38, the signal was further refined to the normalized difference in signal before and after fatigue treatment. Although changes in properties were observed, Figure 38 indicated no statistical difference in population of nitroxyl signals at 50% UTS – 10 Hz.

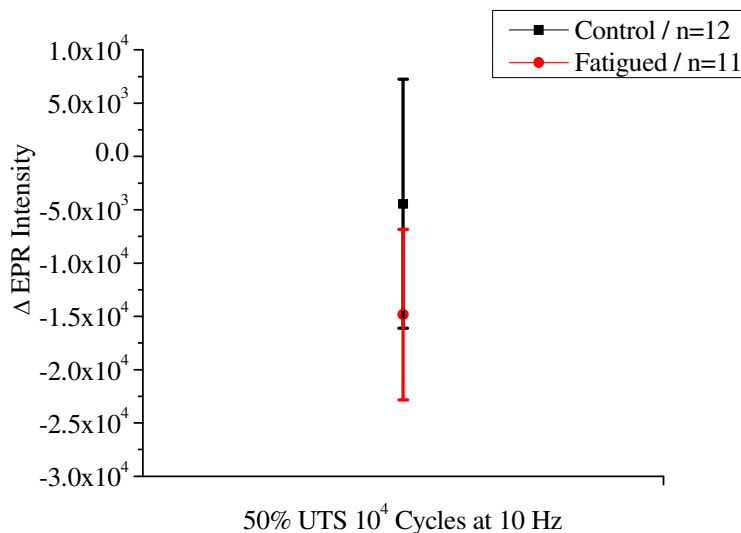


Figure 38. Δ EPR Intensity values of control and fatigue samples from trials 1-4 before and after fatigue treatment normalized to weight and q-value.

All though the average intensities have decreased for the fatigue condition in Figure 37, it has not decreased sufficiently in comparison to the control. Error is associated in this measurement due to the removal and replacement of the sample within the EPR cavity. At 9.8 GHz, a standing microwave possesses a wavelength of approximately 3 cm. This means that spatial placement of the sample to the exact point within the cavity is important for the magnitude of signal detected by the instrument. Since the specific treatment to the sample occurs outside of the cavity, spectra before and after treatment are taken, and placement back into the cavity for the second spectra will result in errors in signal of at least $\pm 7\%$.

This technique is attempting to discern the subtraction of population from existing signal. This makes the confirmed detection more difficult in that it places a requirement of how many events must occur before confidence of a positive result is obtained. Philosophically, it is easier to detect signal in the complete absence of overlapping or

conflicting sources. Extremely low concentrations of radicals can be detected in fracture events. However, this case differs in that before the event there was no EPR detectable source of radicals. Therefore, detecting signal where before there was none is more facile experimentally. In this experimental design, low concentrations of nitroxyl radicals were selected due to the previously mentioned reasons.

50% UTS Conclusions

This study did not observe losses of nitroxyl radicals due to mechanically induced chain scission. Some samples exhibited a loss in mechanical strength while other samples failed from the force input at 50 % UTS. The modulus or stiffness was shown to stay the same or increase after fatigue exposures. This study represents an aggressive approach by using 50 % UTS over a short amount of time. The next study was conducted at lower UTS for an increased duration of time along with FTIR evaluation to measure any additional functional group changes.

Experimental Design of 30% UTS Experiments

Samples were synthesized and manufactured through reaction injection molding as previously described. The next experiment was conducted under two sample conditions, control and fatigue. Nitroxyl radicals were incorporated into the epoxy-amine matrix via BT-IPDI at a loading level of 0.005 wt% as previously described. The samples were thermally annealed as shown in Figure 28. The UTS of the materials is determined in Table 12 through destructive testing of three control samples.

Table 12

Mechanical Properties of 30% UTS Controls

Strain-at-Break	Force-at-Break (N)
0.077	209
0.138	240
0.112	223

Average weight of fatigue sample selections was $76 \text{ mg} \pm 1 \text{ mg}$, and the experimental design is shown in Figure 39. Before the fatigue treatment, the samples were evaluated via EPR, ATR-FTIR, and NIR spectroscopic methods on both the control and fatigue groups. The fatigue test group samples were then exposed to 30% UTS sinusoidal force at a frequency of 10 Hz for 1,000,000 cycles using the BOSE Electroforce 3300 N. The experiment lasts for approximately 27 hours, and the parameters were a stress ratio (R) of 0.1 (Equation 9), force values of 7 N_{\min} and 69 N_{\max} , and a sample gauge length of 8 mm. Post fatigue, the samples were evaluated via the spectroscopic methods listed above. The fatigued samples were then strained to break at a strain rate of 10 %/min, and the resulting stress-strain curve, force-at-break, strain-at-break, and modulus were recorded. The control samples were maintained at ambient lab conditions for 27 hours and reevaluated using the same spectroscopic methods as conducted prior to the time allotment. The control samples were then strained to break at a strain rate of 10 %/min, and the resulting stress-strain curve, force-at-break, strain-at-break, and modulus were recorded.

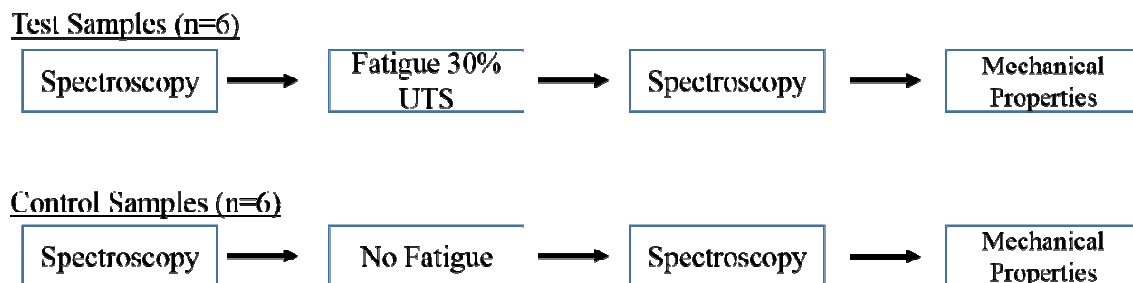


Figure 39. 30% UTS experimental design depiction.

NIR Fatigue Analysis

Near infrared spectroscopy was performed using a Thermo Scientific Nicolet 6700 infrared spectrometer using an InGaAs detector, CaF₂ beam splitter, and a quartz-halogen source. Spectra were obtained in the 10,000 - 4,000 cm⁻¹ region via 32 scans. A Type C attenuator (provided by Thermo) was used during data acquisition while the optical velocity was held constant for all runs. The samples were analyzed via transmission through the thickness of the sample (~ 0.5 mm) using a resolution of 4 cm⁻¹ and an aperture setting of 5.

ATR-FTIR Spectroscopic Analysis

The ATR-FTIR spectroscopy was performed using a Thermo Scientific Nicolet 6700 infrared spectrometer using an MCT/A detector, KBr beam splitter, and a quartz-halogen source. Spectra were obtained in the 4,000 - 750 cm⁻¹ region via 32 scans. A Type B attenuator (provided by Thermo) was used during data acquisition while the optical velocity was held constant for all runs. The samples were analyzed using a diamond ATR crystal with a resolution of 2 cm⁻¹ and an aperture setting of 7.

The data shown in the figures and tables to follow encompass six trials, each composed of one control sample and one fatigue sample that were analyzed through quantitative EPR spectroscopy, NIR, ATR-FTIR, and mechanical properties evaluated

through pull-to-break experiments. Figures 40, 44, 48, 52, 56, and 60 show the EPR spectroscopy of before and after fatigue treatment for trials one through six, respectively. The NIR spectroscopy for trials one through six before and after fatigue treatment are reported in Figures 41, 45, 49, 53, 57, and 61. Before and after fatigue treatment analyzed via ATR-FTIR spectroscopy are presented in Figures 42, 46, 50, 54, 58, and 62 for trials one through six, respectively. The mechanical properties were evaluated through pull-to break experiments, and stress-strain curves of control and fatigue samples are depicted in Figures 43, 47, 51, 55, 59, and 63. The resulting mechanical data from the six trials are reported in Tables 12, 13, 14, 15, 16, and 17.

30% UTS Fatigue Trials Results

30 % UTS 1,000,000 Cycles Trial One

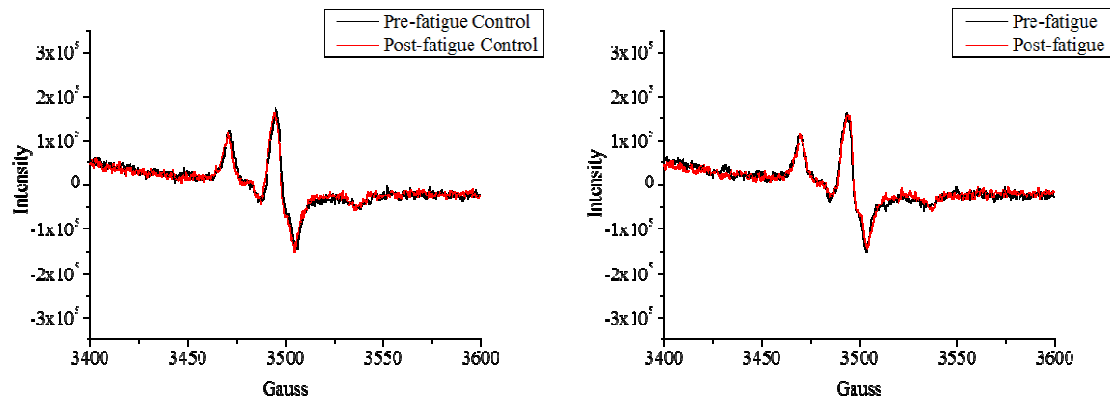


Figure 40. Trial one EPR intensity measurements for control and fatigue conditions before and after treatment.

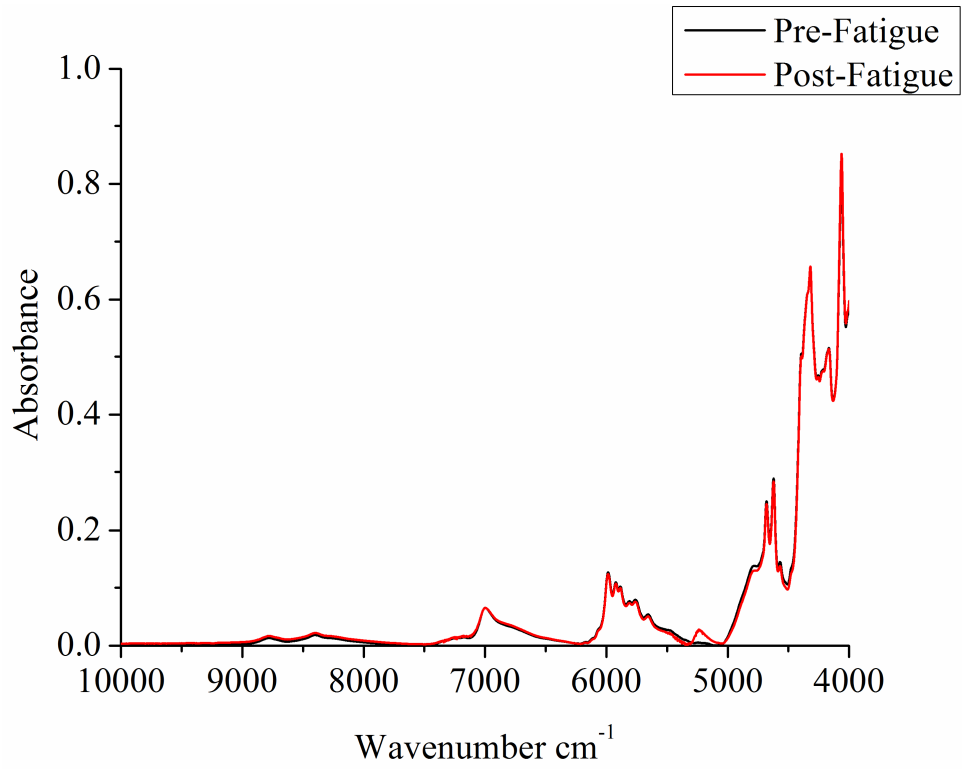


Figure 41. Trial one NIR spectra of fatigue sample before and after treatment.

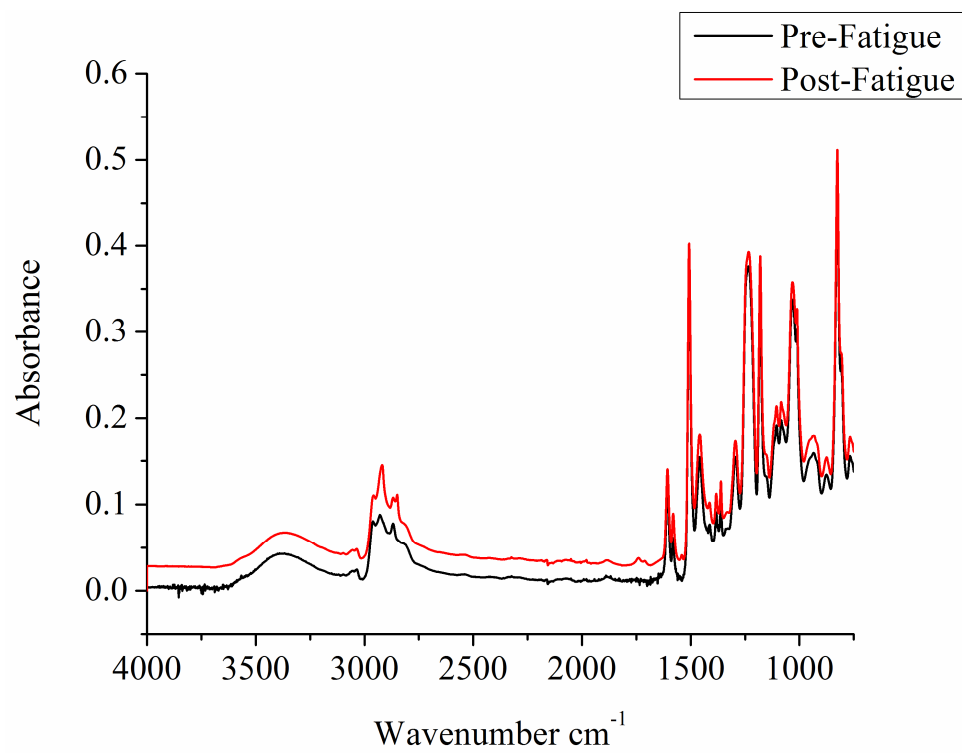


Figure 42. Trial one ATR-FTIR spectra of fatigue sample before and after treatment.

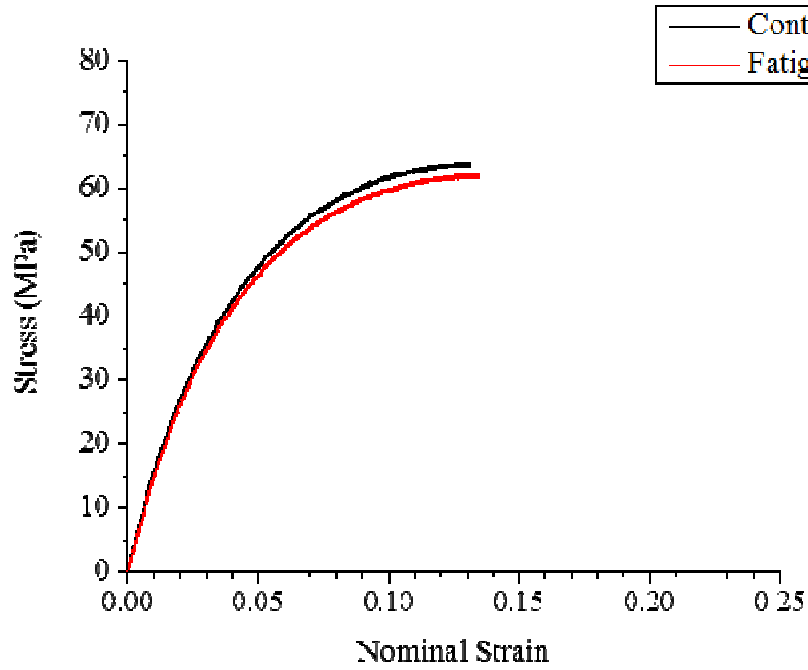


Figure 43. Stress-strain curves of trial one.

Table 13

Trial One Residual Strength Properties at 30% UTS 1,000,000 Cycles

Samples	Strain-at-Break	Force-at-Break (N)	Modulus (GPa)
Control	0.131	226	1.647
Fatigue	0.135	227	1.588

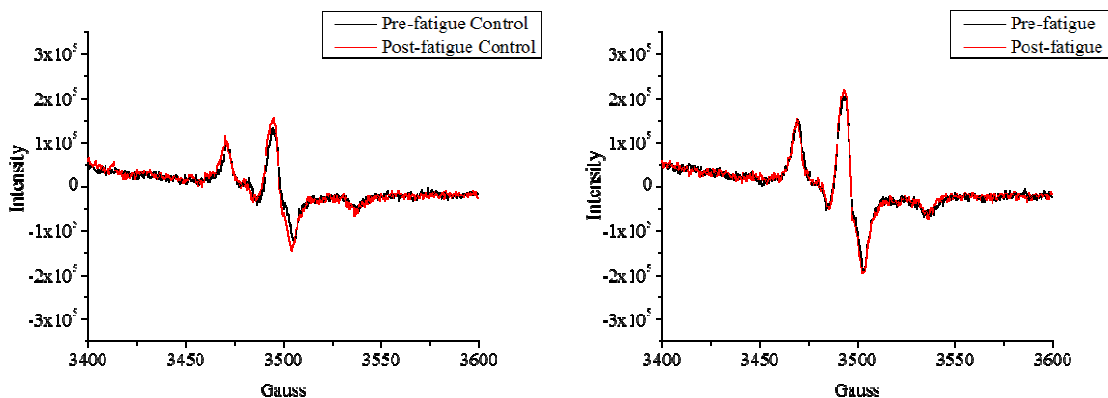
30 % UTS 1,000,000 Cycles Trial Two

Figure 44. Trial two EPR intensity measurements for control and fatigue conditions before and after treatment.

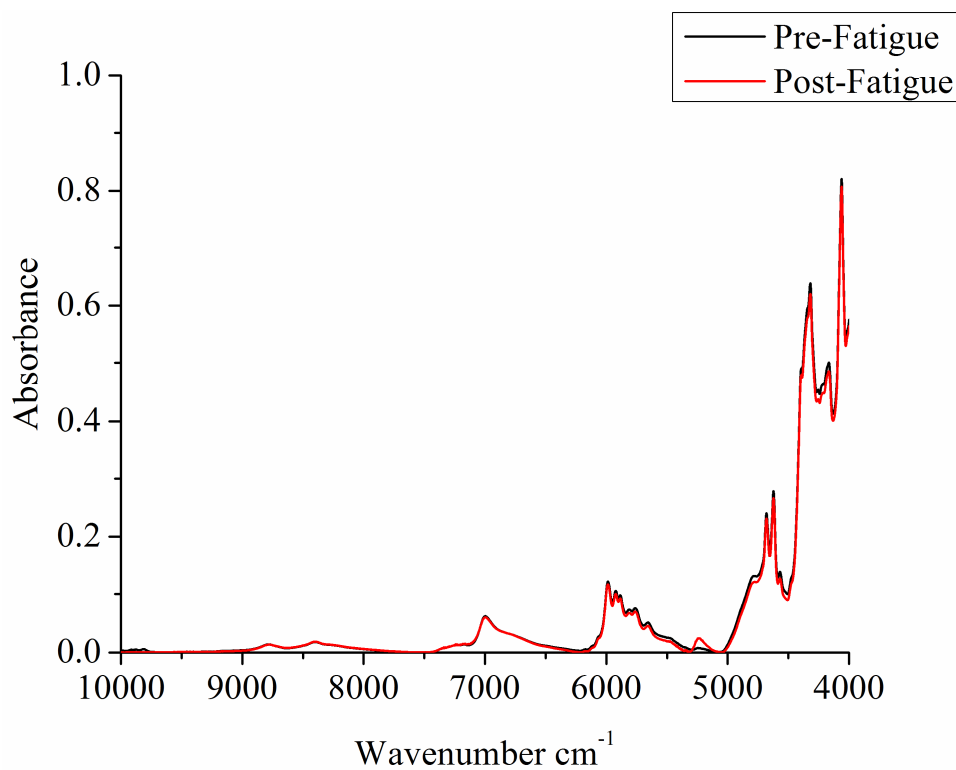


Figure 45. Trial two NIR spectra of fatigue sample before and after treatment.

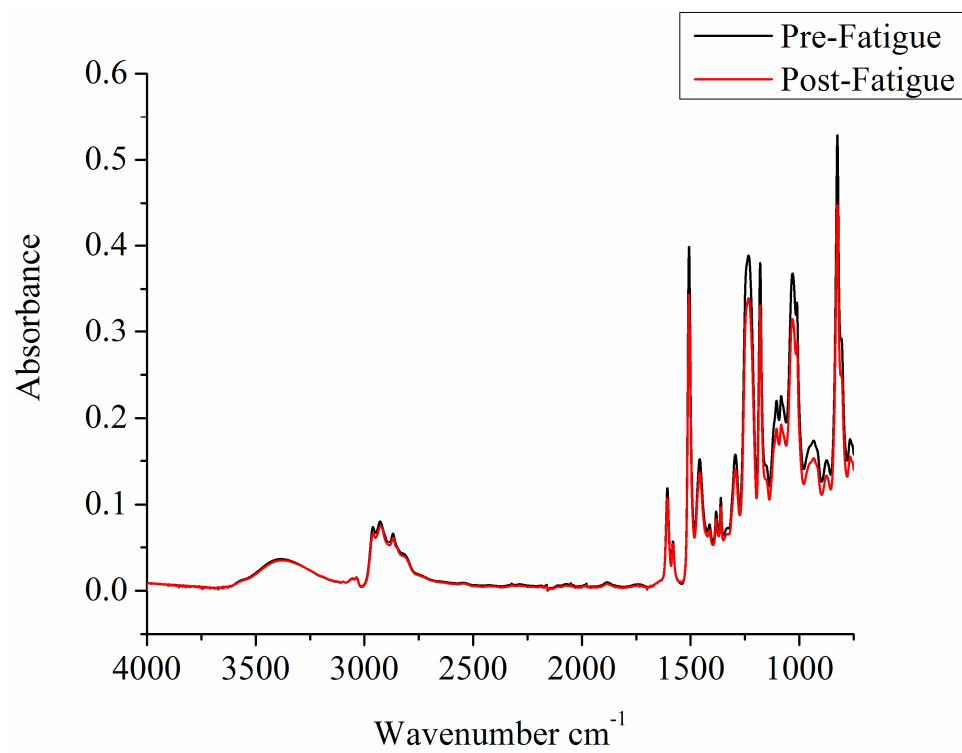


Figure 46. Trial two ATR-FTIR spectra of fatigue sample before and after treatment.

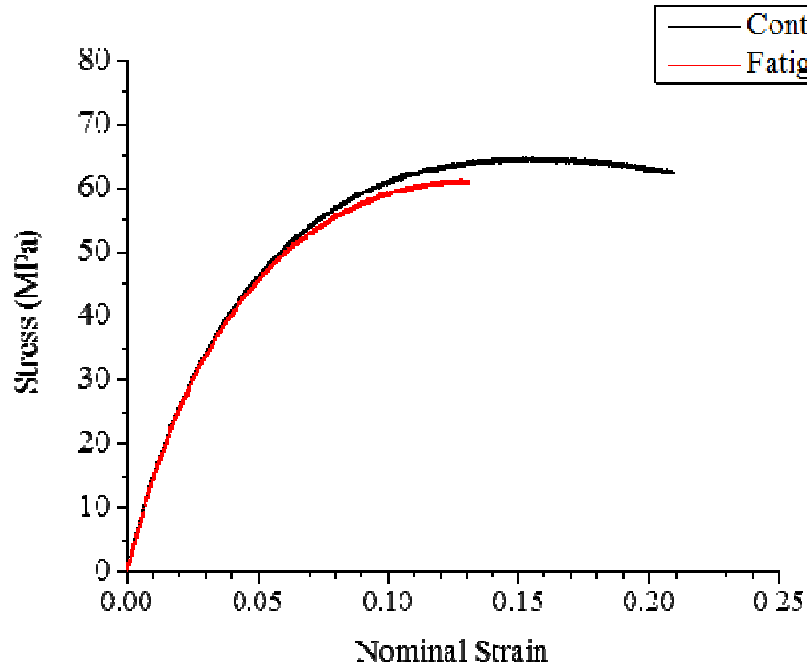


Figure 47. Stress-strain curves of trial two.

Table 14

Trial Two Residual Strength Properties at 30% UTS 1,000,000 Cycles

Samples	Strain-at-Break	Force-at-Break (N)	Modulus (GPa)
Control	0.209	224	1.574
Fatigue	0.137	219	1.541

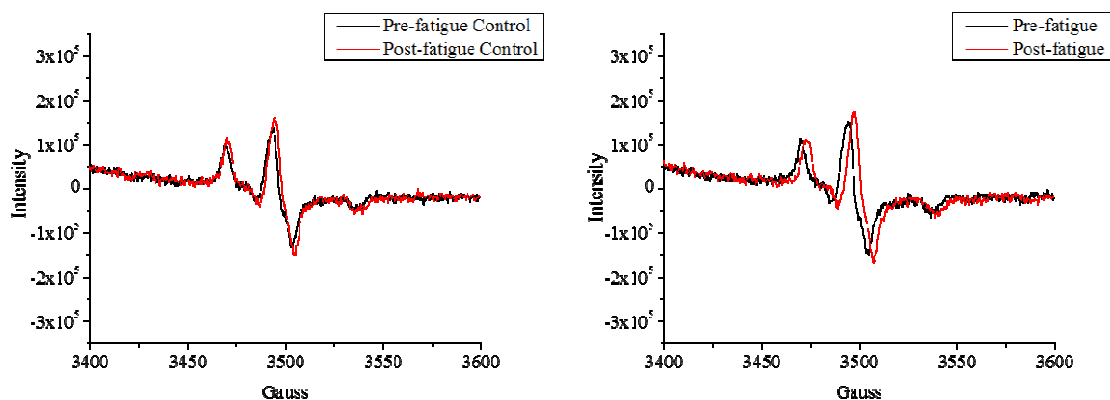
30 % UTS 1,000,000 Cycles Trial Three

Figure 48. Trial three EPR intensity measurements for control and fatigue conditions before and after treatment.

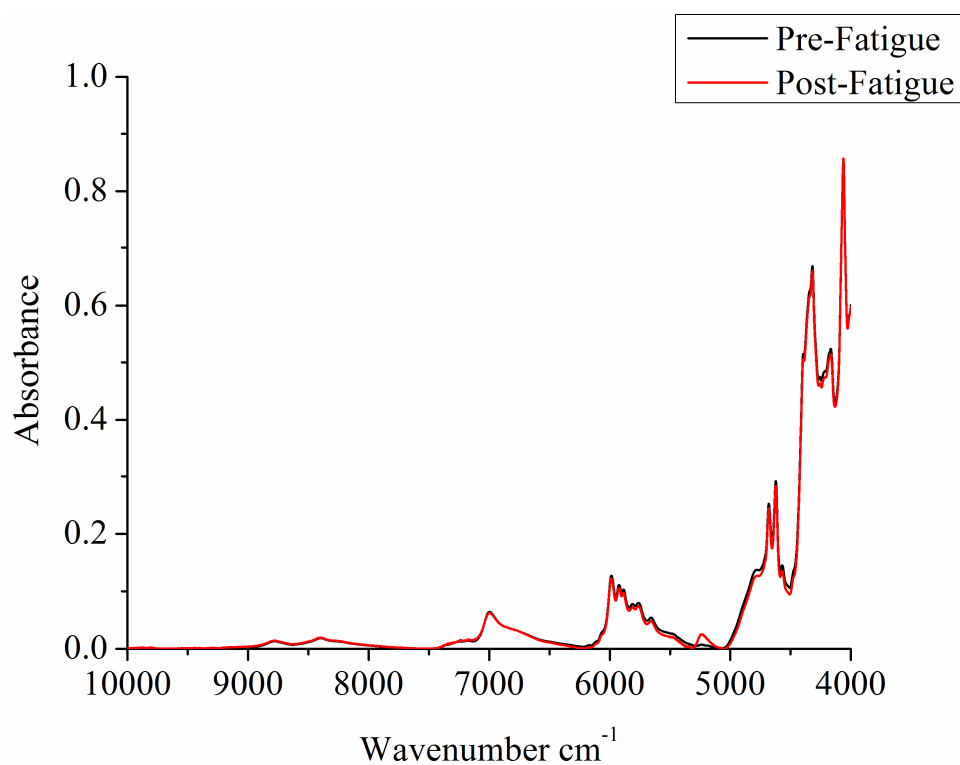


Figure 49. Trial three NIR spectra of fatigue sample before and after treatment.

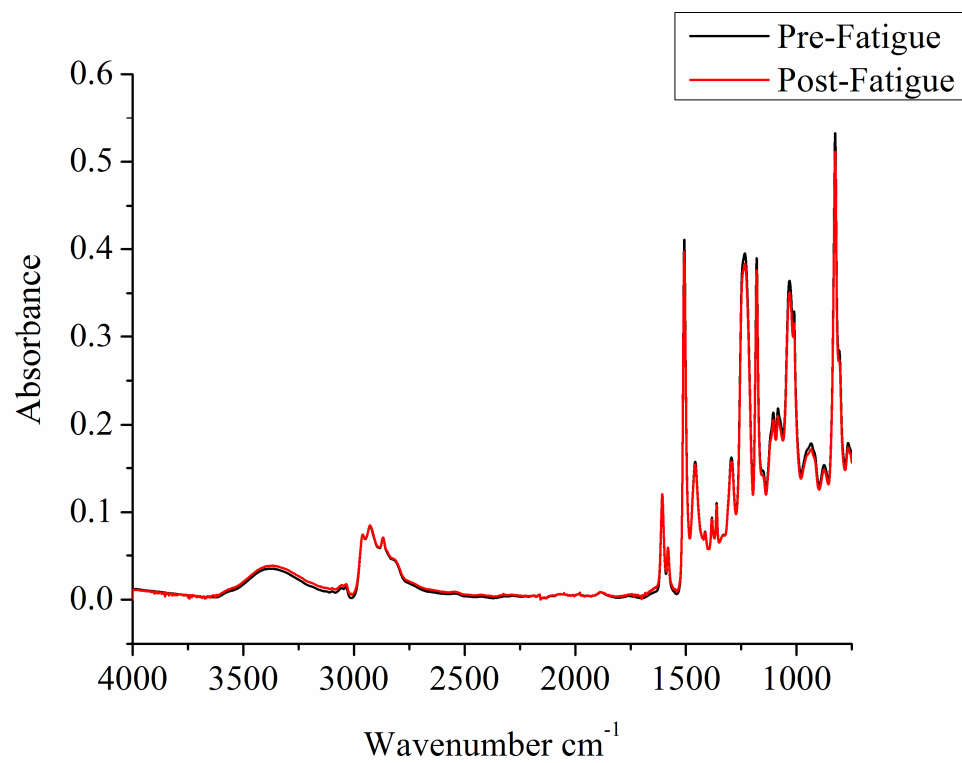


Figure 50. Trial three ATR-FTIR spectra of fatigue sample before and after treatment.

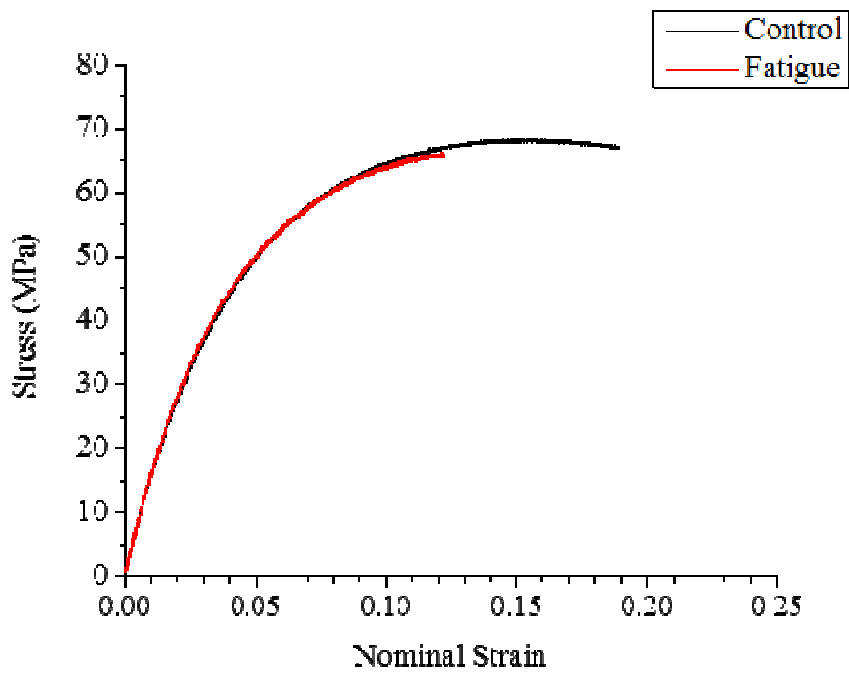


Figure 51. Stress-strain curves of trial three.

Table 15

Trial Three Residual Strength Properties at 30% UTS 1,000,000 Cycles

Samples	Strain-at-Break	Force-at-Break (N)	Modulus (GPa)
Control	0.189	232	1.678
Fatigue	0.154	224	1.683

30 % UTS 1,000,000 Cycles Trial Four

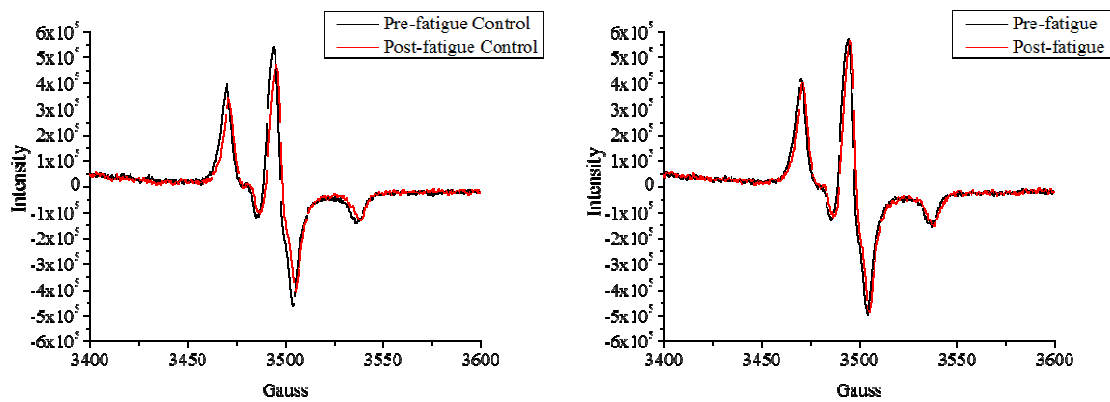


Figure 52. Trial four EPR intensity measurements for control and fatigue conditions before and after treatment.

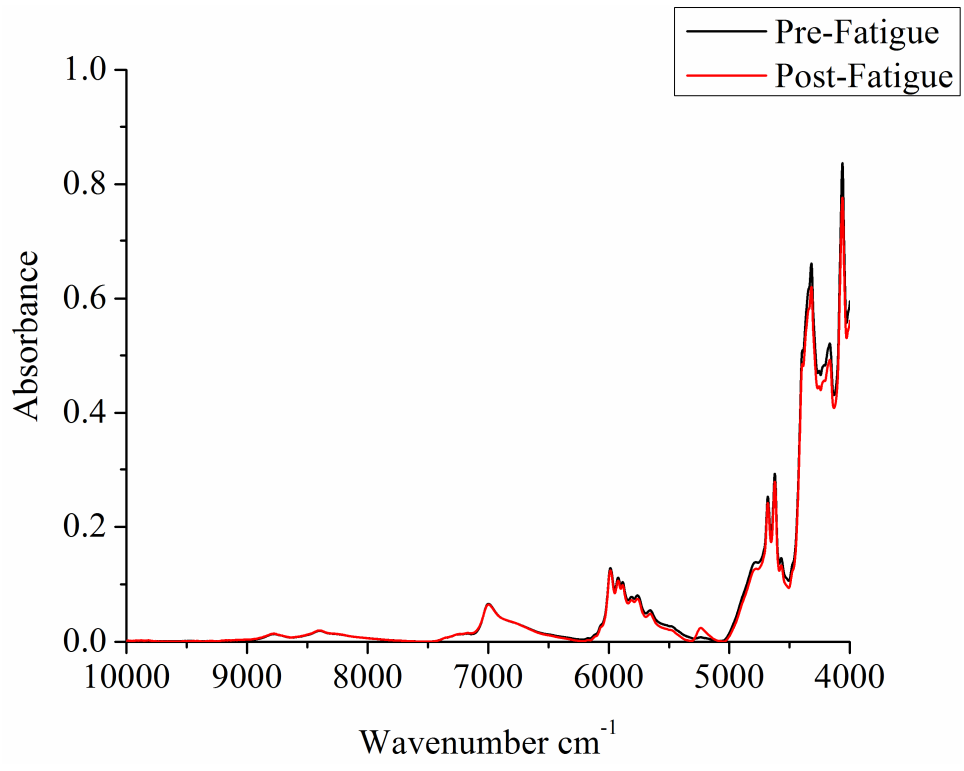


Figure 53. Trial four NIR spectra of fatigue sample before and after treatment.

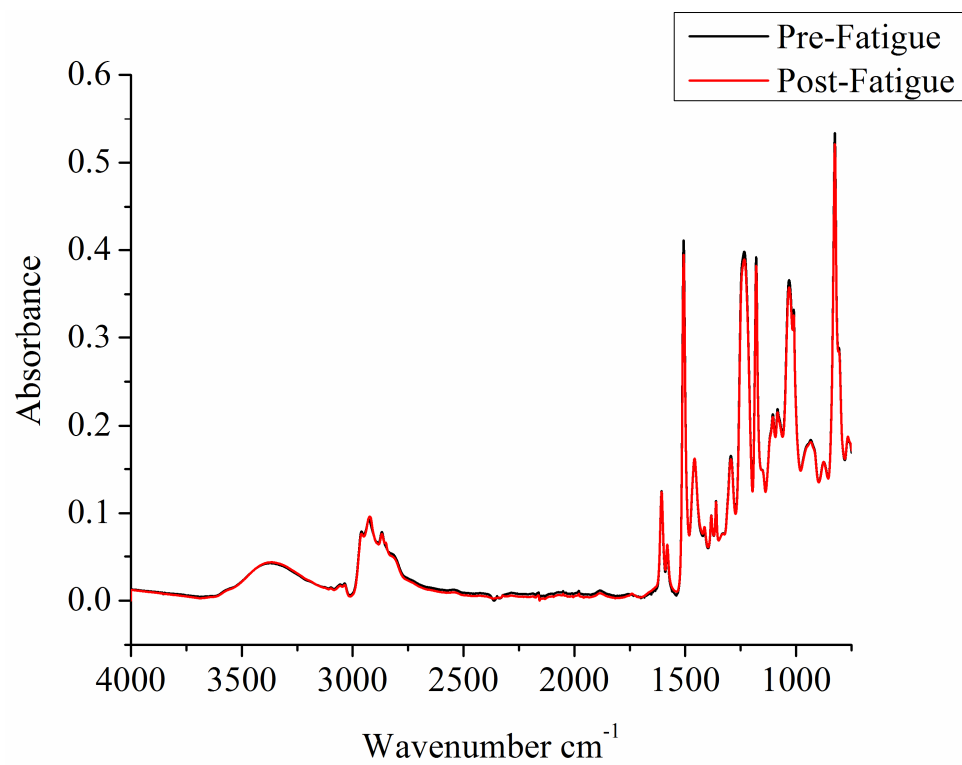


Figure 54. Trial four ATR-FTIR spectra of fatigue sample before and after treatment.

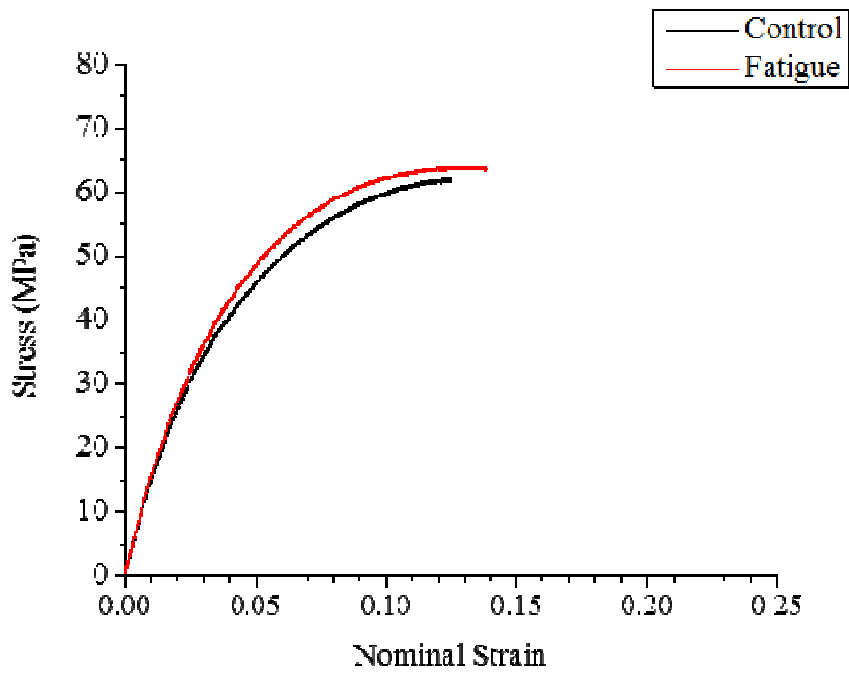


Figure 55. Stress-strain curves of trial four.

Table 16

Trial Four Residual Strength Properties at 30% UTS 1,000,000 Cycles

Samples	Strain-at-Break	Force-at-Break (N)	Modulus (GPa)
Control	0.125	229	1.623
Fatigue	0.138	234	1.585

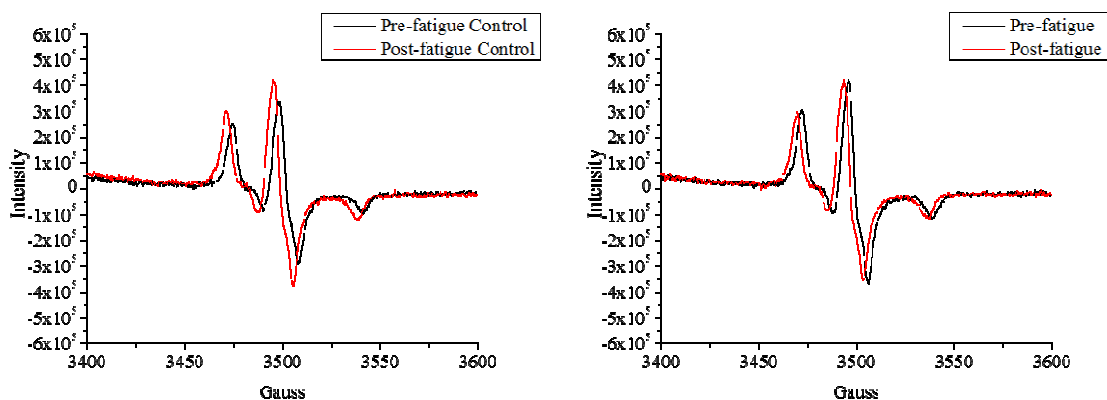
30 % UTS 1,000,000 Cycles Trial Five

Figure 56. Trial five EPR intensity measurements for control and fatigue conditions before and after treatment.

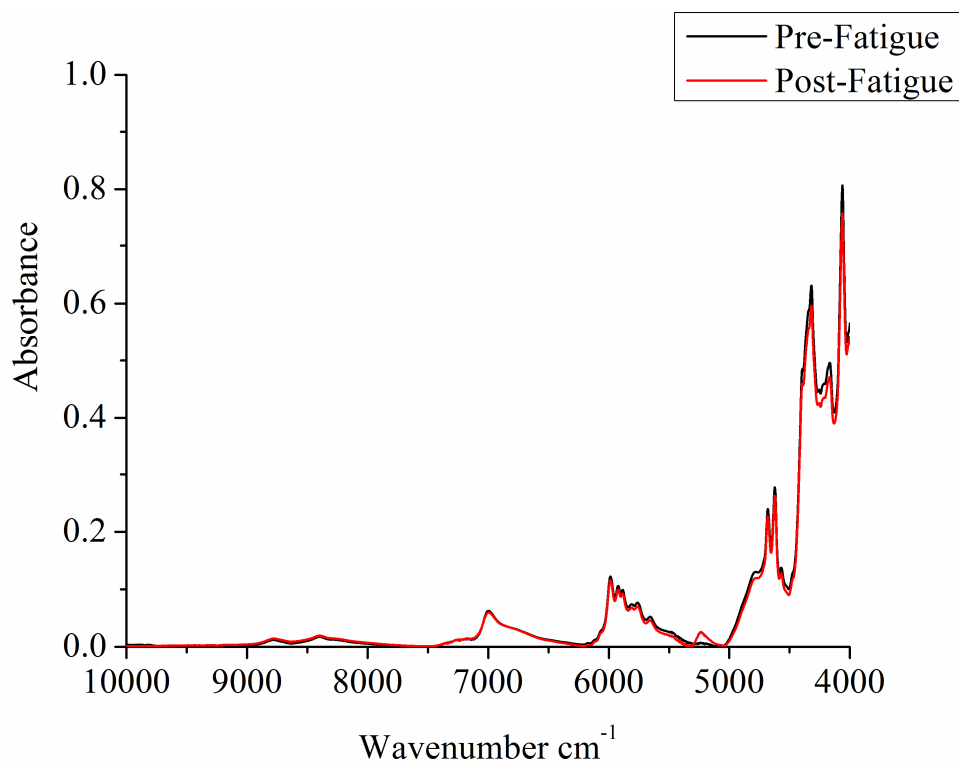


Figure 57. Trial five NIR spectra of fatigue sample before and after treatment.

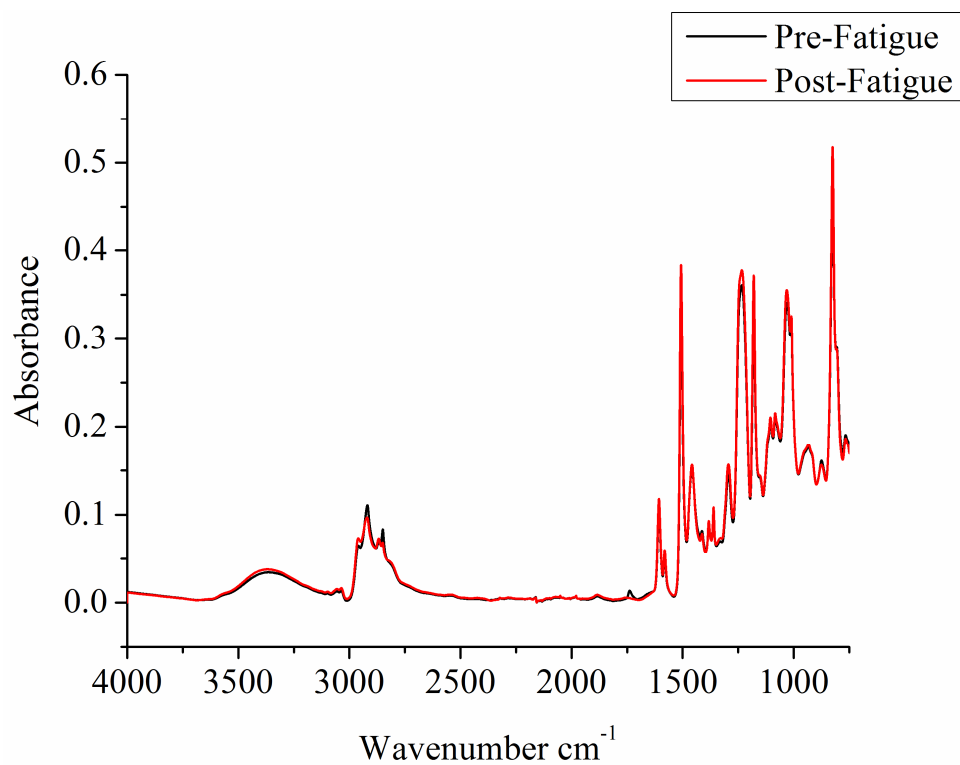


Figure 58. Trial five ATR-FTIR spectra of fatigue sample before and after treatment.

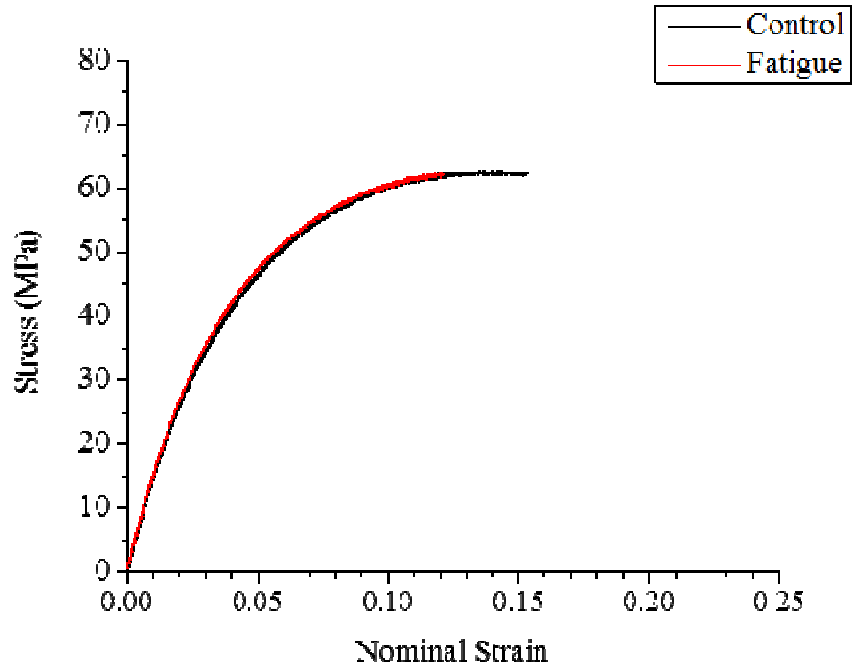


Figure 59. Stress-strain curves of trial five.

Table 17

Trial Five Residual Strength Properties at 30% UTS 1,000,000 Cycles

Samples	Strain-at-Break	Force-at-Break (N)	Modulus (GPa)
Control	0.153	217	1.578
Fatigue	0.121	224	1.582

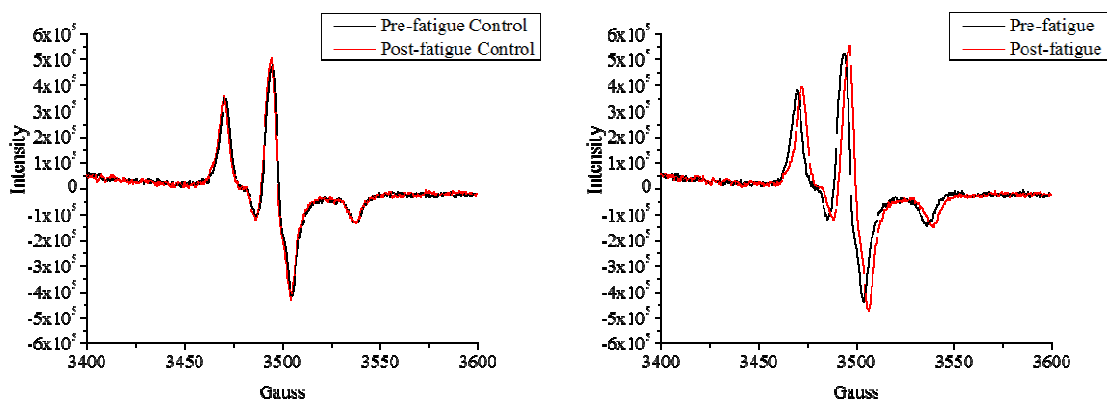
30 % UTS 1,000,000 Cycles Trial Six

Figure 60. Trial six EPR intensity measurements for control and fatigue conditions before and after treatment.

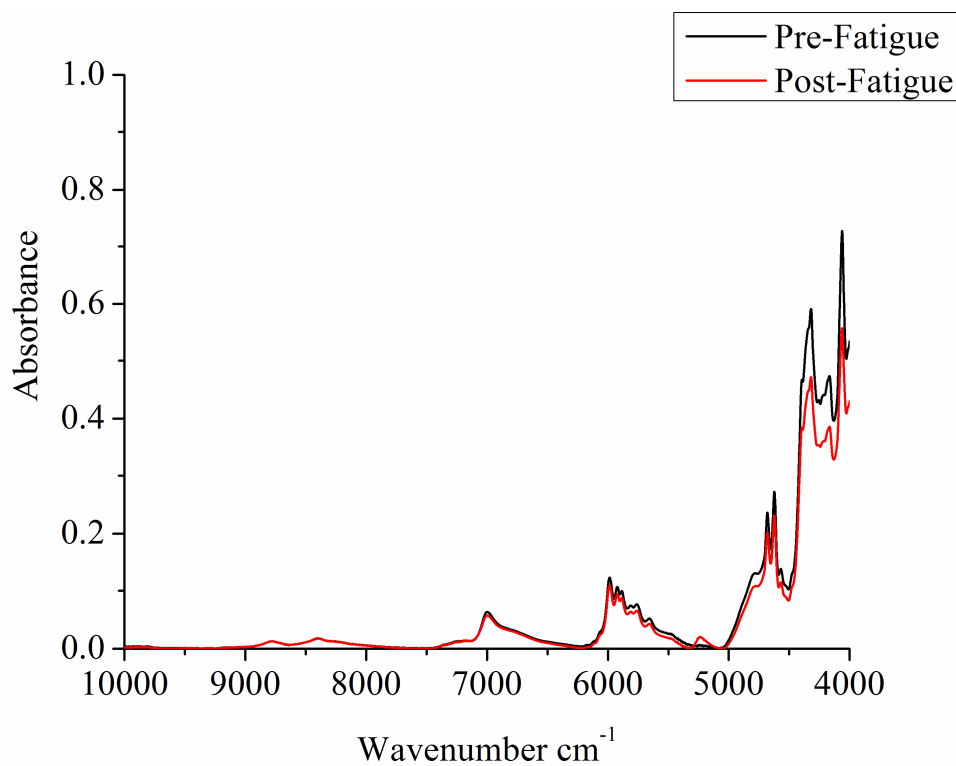


Figure 61. Trial six NIR spectra of fatigue sample before and after treatment.

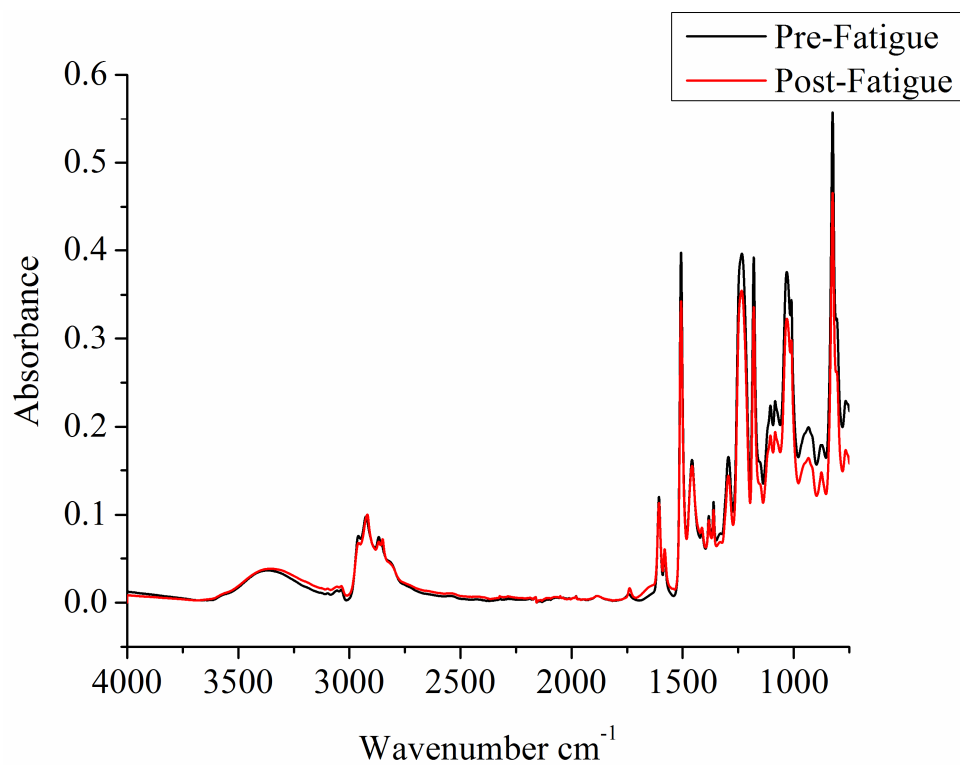


Figure 62. Trial six ATR-FTIR spectra of fatigue sample before and after treatment.

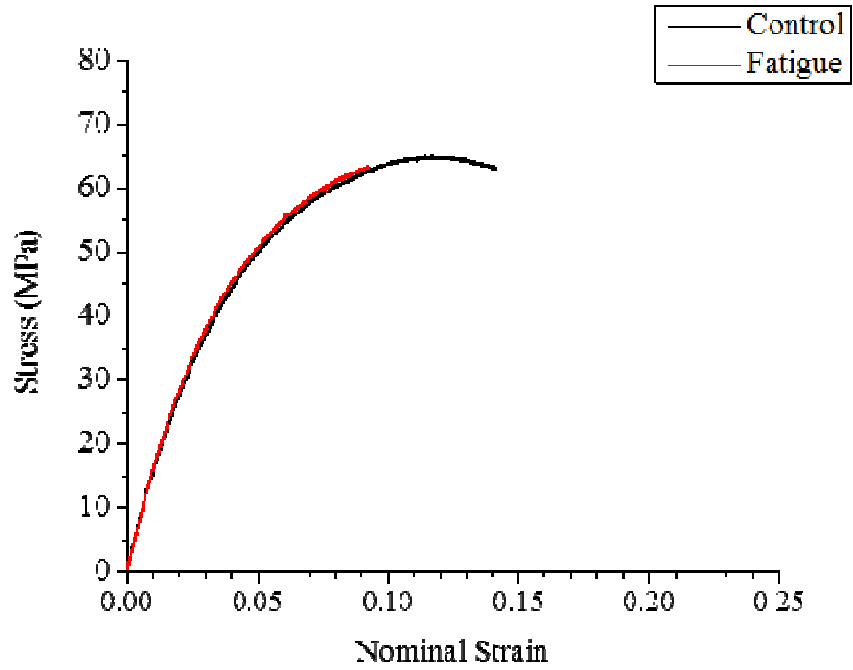


Figure 63. Stress-strain curves of trial six.

Table 18

Trial Six Residual Strength Properties at 30% UTS 1,000,000 Cycles

Samples	Strain-at-Break	Force-at-Break (N)	Modulus (GPa)
Control	0.142	226	1.667
Fatigue	0.093	223	1.685

30% UTS Discussion

Monitoring the peak intensity of the nitroxyl signal across trials 1 - 6, an increase in peak intensity was observed for all samples except the trial 4 control. It is not clear why Figures 52 and 64 show atypical peak decrease. Since this was a control sample, it was not subject to mechanical fatigue, and the EPR experimental settings were nominal. Due to the abnormal result, the EPR data for this sample was not included in subsequent analysis with averages, standard deviations, and Δ EPR intensity graphs.

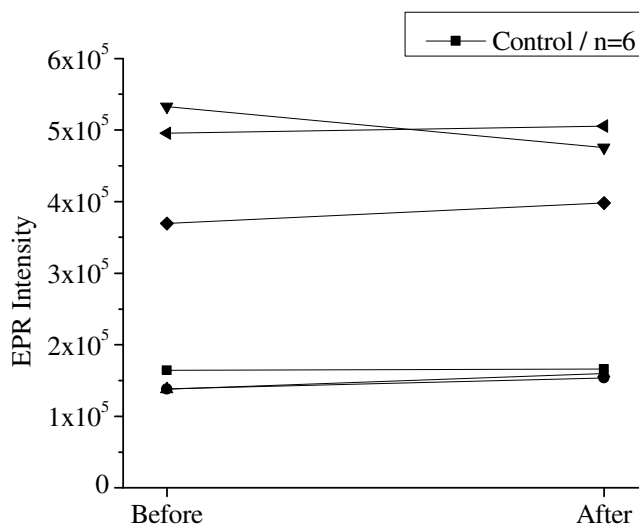


Figure 64. EPR intensity values of control samples from trials 1-6 before and after time allotment normalized to q-value.

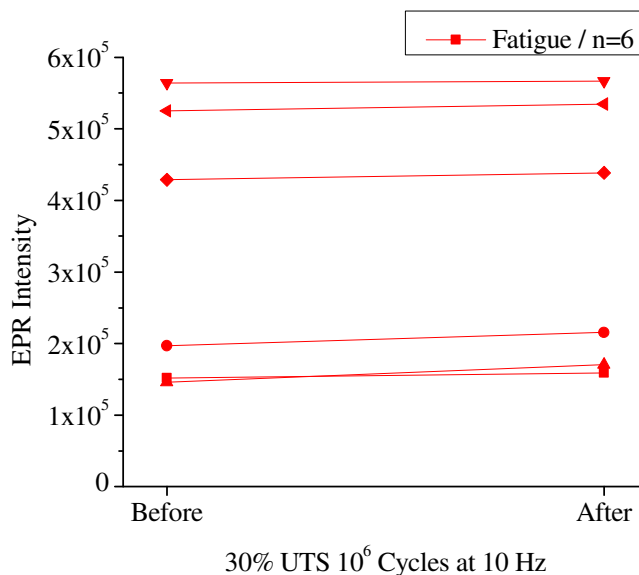
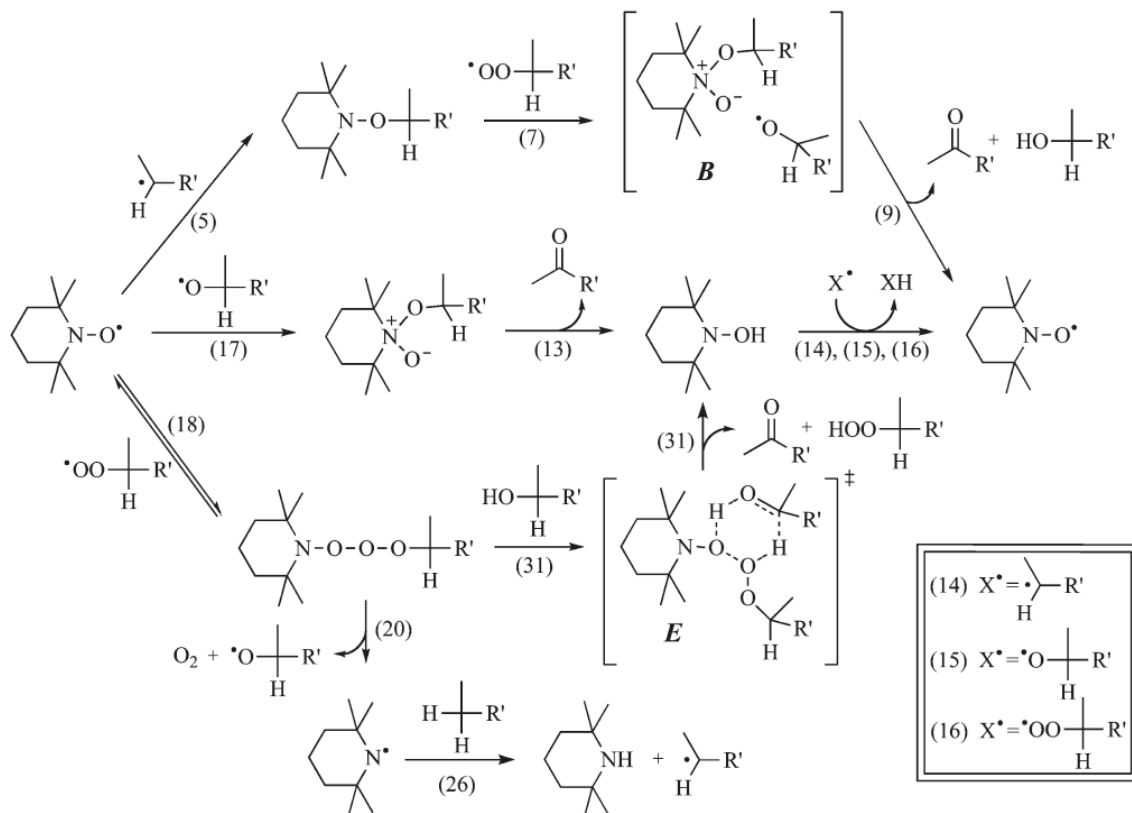


Figure 65. EPR intensity values of fatigue samples from trials 1-6 before and after fatigue treatment normalized to q-value.

The peak intensity values differ in magnitude from each other as is clearly indicated in the EPR spectra for all six trials as well as the summary intensities in Figures 64 and 65. This is attributed to the products generated via the Denisov cycle, which portrays the equilibrium of mechanisms when nitroxyl radicals react with atmospheric oxygen (Scheme 5). While nitroxyl radicals do not react directly with oxygen¹⁰, oxygen will react with various functional groups within the polymer via radical mechanisms. Nitroxyl radicals can react with the various side products of oxidative degradation, even at ambient temperatures. The starting intensities vary due to the varying ages of the samples, a necessity from the method of manufacturing through reaction injection molding. However, the focus of this experiment was the change in magnitude of the EPR signal due to mechanical fatigue, not the initial intensities.



Scheme 5. Denisov cycle demonstrating major products of the reaction of alkyl, alkoxy, and peroxy radicals with TEMPO. Clarifying the mechanism of the Denisov cycle: How do hindered amine light stabilizers protect polymer coatings from photo-oxidative degradation, by J.L. Hodgson and M.L. Coote, 2010, *Macromolecules*, volume 43, p. 4582. Reprinted with permission from the publisher.¹¹

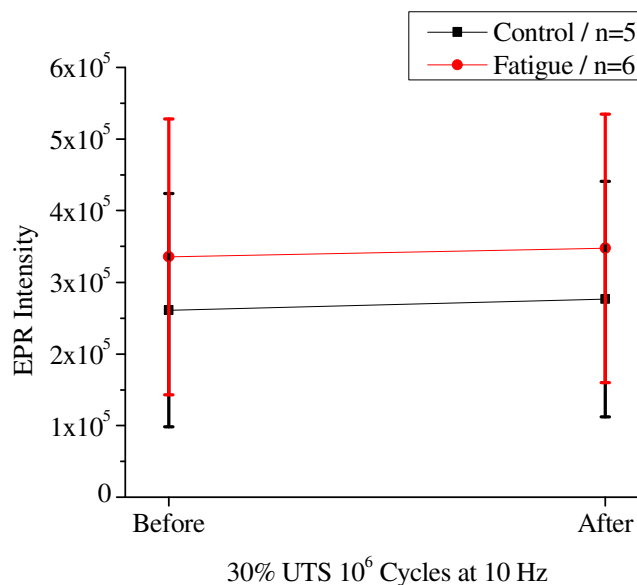


Figure 66. EPR intensity average values of control and fatigue samples from trials 1-6 before and after fatigue treatment normalized to q-value. Trial 4 control has been excluded due to error.

The EPR spectra and average intensity values in Figures 66, both control and fatigue conditions, were observed to increase. Figure 67 shows that both control and fatigue conditions exhibited equal increases in EPR intensities (excluding trial control from analysis) indicating that the increase was caused by a mechanism other than mechanical degradation, possibly the Denisov cycle (Scheme 5).

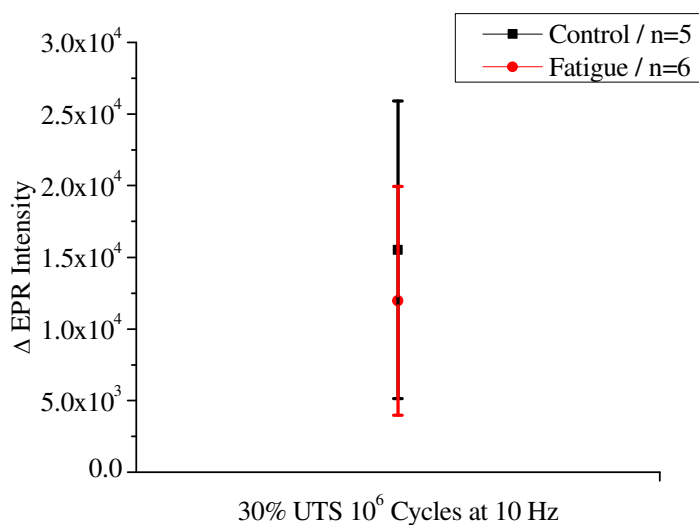


Figure 67. Δ EPR intensity normalized to q-value for control and fatigue conditions post treatment. Trial 4 control has been excluded due to error.

Hodgson and Coote performed various chemical simulations to describe the possible mechanisms involving hindered amine light stabilizers (HALS).¹¹ Structurally, HALS are very similar to TEMPO-based molecules in that the N-O nitroxyl radical is replaced with an amine-hydrogen N-H functional group. Through various reactions, as shown in Scheme 5, the nitroxyl radical can be converted to various non-paramagnetic functional groups and then back to a nitroxyl radical in a cyclical manner. Through these mechanisms, HALS protect coatings and polymer formulations from oxidative degradation.

Despite the samples being cured and annealed under an inert nitrogen atmosphere, it is possible that the sample has absorbed oxygen gas during storage or synthesis. At the cure temperatures of 120 °C, oxygen radicals can react via any of the mechanisms shown in Scheme 5. While the products of such reactions are not known, the increase in EPR signal suggests that nitroxyl radicals were likely converted to N-H or N-OH during

synthesis and then back to nitroxyl radicals over the 27 hour experimental time via the Denisov cycle.

This equilibrium effect was not observed in previous experiments, possibly due to the time differences. The experiments for 10,000 cycles at 10 Hz lasted 15 minutes unlike the 27 hours required to complete 1,000,000 cycles. Thus, within the context of 27 hours, the equilibrium changes become significant. Based on the fact that the control and fatigue conditions produced the same EPR result, we can conclude that chain scission events were not detected.

From the NIR spectra of all six trials, no changes or production of new functional groups were detected other than the uptake of atmospheric water at approximately 5200 cm^{-1} . The ATR-FTIR spectra showed spectral overlap for both control and fatigue conditions indicating that the nature of functional groups did not change due to mechanical forces. Unlike the 50% UTS trials, no mechanical degradation was noted with the samples subject to fatigue. All samples were able to endure 1,000,000 cycles at 30% UTS without failure. In both the 30% UTS and 50% UTS trials, no chain scission events were detected via loss of signal with nitroxyl radicals. However, this study did not indicate whether chain scission was produced from fatigue experiments.

Conclusions

In this Chapter, nitroxyl radicals were incorporated into an epoxy matrix to detect mechanically produced homolytic chain scission events resulting from fatigue. The epoxy-amine matrix was subject to 30% UTS and 50% UTS fatigue studies with subsequent EPR and FTIR spectroscopies to detect changes in nitroxyl radical populations and epoxy-amine functional groups. Although mechanical property

decreases and fatigue failure of specimens were observed in the 50% UTS study, decreases in nitroxyl populations relative to controls were not observed. This indicates that chain scission events were not detected. No changes in properties or functional groups within the epoxy-amine matrix were observed in the 30% UTS study. However, both control and fatigue conditions resulted in increases of nitroxyl radical population. This is attributed to the Denisov cycle significantly affecting nitroxyl populations within the 27 hour time frame of the study.

Non-detection of chain scission events can be attributed to several reasons. The viscosity of the glassy state is relatively high and can impede diffusion of the radical chain end to a BT-IPDI molecule. Also, it is unknown whether fatigue produces chain scission events prior to failure. Radicals are known to be capable of migration based on hydrogen abstraction. If radicals were known to be produced through mechanical destruction of the sample, it could then be determined experimentally if reactions could take place between the mechano-radicals and BT-IDPI. This would help elucidate if the physical barrier of the glassy state impedes both physical migration and chemical migration of mechano-radicals during strain.

REFERENCES

1. G. Tao & Z. Xia. A non-contact real-time strain measurement and control system for multiaxial cyclic/fatigue tests of polymer materials by digital image correlation method. *Polymer Testing* **24**, 844-55, (2005).
2. G. Tao & Z. Xia. Fatigue behavior of an epoxy polymer subjected to cyclic shear loading. *Materials Science and Engineering: A* **486**, 38-44, (2008).
3. G. Tao & Z. Xia. Biaxial fatigue behavior of an epoxy polymer with mean stress effect. *International Journal of Fatigue* **31**, 678-85, (2009).
4. G. Tao & Z. Xia. Ratcheting behavior of an epoxy polymer and its effect on fatigue life. *Polymer Testing* **26**, 451-60, (2007).
5. G. Tao & Z. Xia. Mean stress/strain effect on fatigue behavior of an epoxy resin. *International Journal of Fatigue* **29**, 2180-90, (2007).
6. G. Tao & Z. Xia. An experimental study of uniaxial fatigue behavior of an epoxy resin by a new noncontact real-time strain measurement and control system. *Polymer Engineering & Science* **47**, 780-88, (2007).
7. K.F. Fazende. *Preparation and detection of degradation and chain scission events in epoxy-amine networks using a profluorescent nitroxide probe*. The University of Southern Mississippi. (2013).
8. *Electron Paramagnetic Resonance: A Practitioner's Toolkit*. (John Wiley & Sons, Inc, 2009).
9. G.R. Eaton, S.S. Eaton, D.P. Barr & R.T. Weber. *Quantitative EPR*. (Springer, 2010).
10. J.P. Blinco. *The Synthesis and Application of Novel Profluorescent Nitroxides as Probes for Polymer Degradation*. Queensland University of Technology. (2008).
11. J.L. Hodgson & M.L. Coote. Clarifying the Mechanism of the Denisov Cycle: How do Hindered Amine Light Stabilizers Protect Polymer Coatings from Photo-oxidative Degradation? *Macromolecules (Washington, DC, U. S.)* **43**, 4573-83, (2010).

CHAPTER V

CRYO-GRINDING OF EPOXY-AMINE THERMOSETS

Introduction

As a summary of research findings so far, in Chapter II, Bis-TEMPO-IPDI was synthesized from 4-hydroxy-TEMPO and isophorone diisocyanate and the nitroxyl radical FEW shown to be retained through titration experiments. In Chapter III, it was demonstrated that BT-IPDI possessing nitroxyl radical functionality and molecules incorporating urethane functional groups could be incorporated without affecting the kinetics of the DGEBA/2-methyl-1,5-diaminopentane reaction at loading levels exceeding 5 wt%. In Chapter IV, BT-IPDI was used as a molecular probe to detect homolytic chain scission events resulting from mechanical fatigue at 30% UTS and 50% UTS. The nitroxyl radicals were not observed to decrease in comparison to controls concluding that covalent bond scission was not detected. An uncertainty exists in that it is unknown if covalent bond scission was produced in fatigue experiments. If chain scission events were produced, could the nitroxyl radicals react with the mechano-radicals? It would be advantageous to produce chain scission events to then observe if the nitroxyl radicals are capable of reacting with the mechano-radicals.

Mechanical grinding of polymer and the production of radicals from broken bonds has been performed since the 1950s.¹ Several papers have since been published regarding radical formation via mechanical fracture of samples.²⁻⁷ Liquid nitrogen temperatures of 77 K stabilize the radical functional group trapping it within a glassy matrix. Forming mechano-radicals from grinding is a specific characteristic of polymers. Cryo-grinding materials composed of low molecular weight molecules only breaks the

Van der Waal attractive forces and hydrogen bonding, not the covalent bonds.

Researchers have shown that radicals could be formed and stabilized at low temperatures until EPR spectroscopic analysis of the samples could be performed. Literature has shown that grinding of epoxy-amine thermosets does indeed result in carbon centered radicals, specifically the cumyl radical by cleaving the phenyl group and the central carbon in the DGEBA repeat unit.⁴ The tertiary carbon radical is then stabilized by delocalization into the adjacent phenyl ring.⁴ No concrete evidence has been shown to indicate the detection of the phenyl radical counter partner, which is most likely due to the high reactivity of the phenyl radical.⁸ Therefore, the aim of the research in chapter five is to induce homolytic scission of the covalent bonds of an epoxy-amine matrix and determine if the resulting radicals are capable of reacting with nitroxyl radicals incorporated into the matrix.

Experimental

Epoxy-amine thermosets used in this study were DGEBA / 2-methyl-1,5-diaminopentane and in addition SC-15. SC-15 is a rubber toughened 2 component formulation of DGEBA as an epoxy and a proprietary aliphatic amine as a hardener. This set of experiments are reported here involving SC-15 because cryo-grinding experiments are difficult to perform, and the data gathered when this system was initially studied exemplifies nitroxyl EPR behavior at variable temperature. It is included here as a case study to show how nitroxyl radicals should respond to variable temperature EPR experiments.

Materials used in this study are DGEBA and 2-methyl-1,5-diaminopentane as shown in Scheme 1 of Chapter II. Epon 828 (DGEBA) was degassed under vacuum for

approximately 6 hours prior to introduction of amine. For samples containing nitroxyl probes, BT-IPDI, synthesized in Scheme 2 was incorporated through volumetric addition of BT-IPDI - acetonitrile solution to DGEBA monomer to achieve target wt% loading of final samples. Acetonitrile (boiling point 82 °C) was removed from DGEBA by heating the sample at 80 °C under vacuum overnight. The DGEBA monomer was measured gravimetrically to ensure complete solvent removal and mixed with 2-methyl-1,5-diaminopentane at a molar ratio of 1:1 based on epoxide to amine hydrogens. The blend was poured into silicone molds, which had been sprayed with a dry film mold release agent to facilitate sample removal.

The samples were then allowed to vitrify overnight and post-cured in the morning in a nitrogen purged, forced air convection oven at 60 °C for 85 minutes followed by 120 °C for 145 minutes. The nitrogen atmosphere was maintained to avoid oxidative degradation of the nitroxyl radicals. Prior to mechanical testing, the materials were annealed thermally under nitrogen as discussed earlier in Chapter IV, Figure 28 to erase any aging effects as well as remove absorbed atmospheric water and trapped oxidative radicals prior to conducting the experiment. The same manufacturing procedures were used for the SC-15 formulations.

Cryo-grinding Experimental

The fracturing of samples was performed in a dry box nitrogen atmosphere. Samples were cooled to liquid nitrogen temperatures and ground using a high speed grinder, which sprayed the powder directly into liquid nitrogen. The powder was then collected quickly into an EPR tube and capped within the dry box nitrogen atmosphere. The EPR tube was then quickly submerged into a liquid nitrogen dewar and removed

from the dry box. The sample was removed from the dewar and inserted into the EPR cavity, which had been precooled to 130 K. Below, in Figure 8, is a depiction of the cryo-grinding procedure.

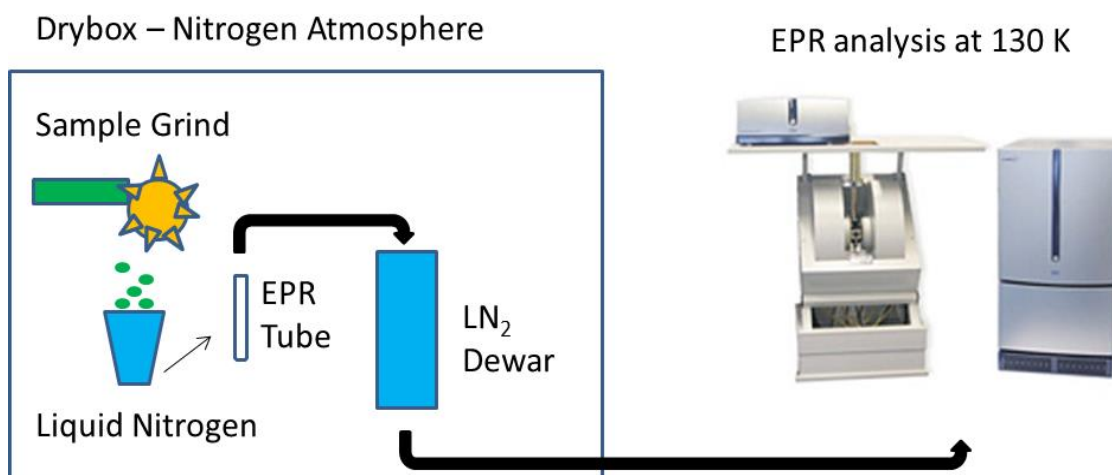


Figure 68. Cryo-grinding experimental procedure.

EPR Analysis

The variable temperature (VT) EPR spectroscopic measurements were carried out on a Bruker EMX^{Micro} X-band spectrometer using quartz variable temperature holder cooled to 130 K. The following EPR instrumental settings were used to collect each spectrum: a microwave power of 0.6 mW, receiver gain of 5020, frequency of 9.5 GHz, modulation amplitude of 2 gauss, modulation frequency of 100 KHz, conversion time of 20.48 msec, time constant of 20.48 msec, and signal averaging of 16 scans. The temperature was increased in a stepwise manner pausing for several minutes at each temperature stage to equilibrate and collect spectra.

Light Scattering Analysis for Particle Size

Particle size distribution of the ground powder samples was determined using the Zetatrac Particle Size Analyzer with Turbotrac attachment. Index of refraction was

chosen to be 1.60 for ground particles with a detection range for particle sizes of 0.25 μm to 250 μm .

Results

In this first experiment, SC-15 (rubber toughened DGEBA crosslinked with proprietary aliphatic amine) was cryo-ground using the previously mentioned synthesis and manufacturing procedures within the experimental section. From Figure 69, a broad single peak was observed that decreased with increasing temperature. There was a sharp peak present within the spectra that is a paramagnetic defect of the quartz EPR sample tube. Although an artifact signal is present, continued analysis of this experiment is still beneficial. As the signal increases and the matrix softens, radicals should recombine and EPR signal decrease accordingly.

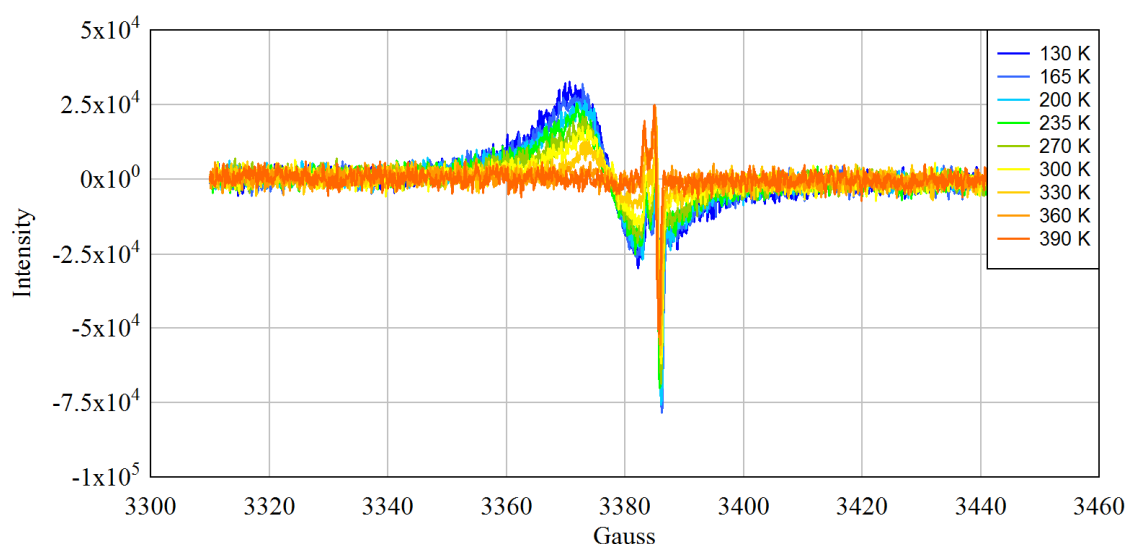


Figure 69. VT-EPR spectra of cryo-ground SC-15.

It is well known that EPR and NMR signals vary in strength based upon Boltzmann statistics. Within a magnetic field, spins are aligned against and with the magnetic field in two states as shown in Figure 5 of Chapter I. The population of the

spins are divided fairly evenly between the two states. The population differences is not exactly even, otherwise NMR and EPR spectroscopic techniques would not be possible. There is a slight difference in number between those in the upper and those in lower spin states with a slight excess being in the lower spin state. The slight excess in spins is the source of all signal originating from EPR and NMR spectroscopy. The higher the field strength of the magnet, the larger the number of excess spins and thus larger signal. Also, due to Boltzmann statistics, the lower the temperature, the larger the number of excess spins and thus larger signal. Distinguishing between chemical events leading to loss of signal and temperature/Boltzmann effects required modeling using Equation 11.

$$\frac{n_a}{n_p} = e^{\frac{-h\nu}{kT}}$$

Equation 11. Boltzmann statistics equation calculating the difference in quantum states as a function of temperature.⁹

Equation 11 gives the ratio of spin states aligned against the magnetic field (n_a) and with the magnetic field (n_p). The plank constant h is multiplied by the frequency of light, ν , which is approximately 9.5 GHz. The Boltzmann constant, k , is multiplied by the temperature T (K). At 130 K, the difference in quantum states is equal to 0.9965. This means that, out of a population of 10,000 spins, 35 spins are the difference in states and the actual source of EPR signal. At a temperature of 390 K, the difference in states has decreased to 0.99883, or approximately 12 spins out of ten thousand.

Since signal is proportional to population, double integration of the spectra within Figure 69 reflects the change in either population or change in signal due to temperature. Using Equation 11, the signal can be modeled with a population of 10,000 spins to calculate the change in signal due to change in temperature. Graphically, this can be

represented in Figure 70 as the orange curve showing the number of spins in EPR source signal as a function of temperature calculated from Equation 11.

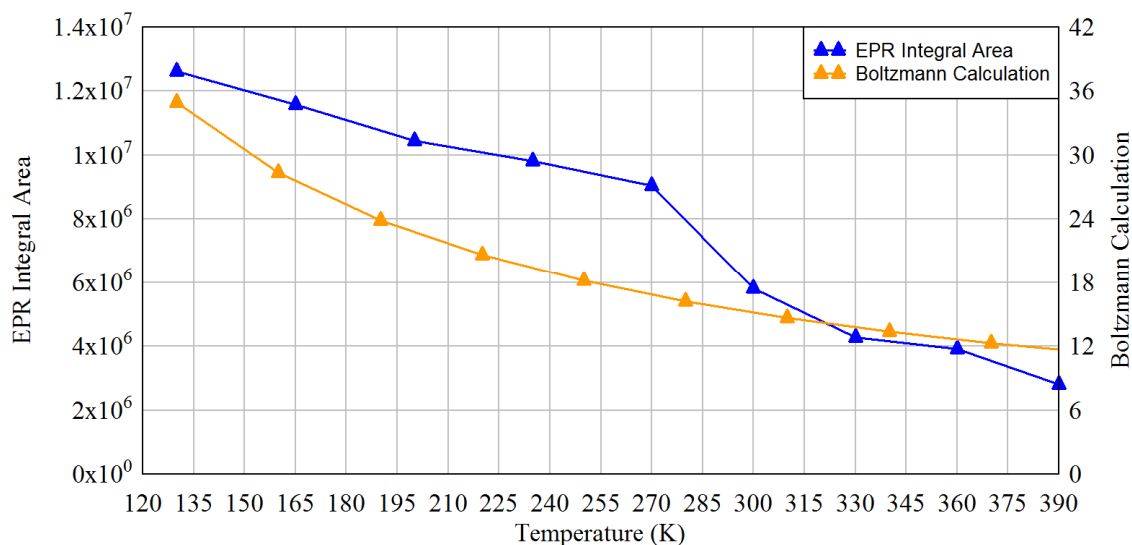


Figure 70. SC-15 cryo-ground EPR integral areas compared to Boltzmann statistics calculation for decreasing differences in quantum states with increasing temperature.

Figure 70 shows that at low temperatures, the decrease in signal closely follows the Boltzmann calculation until 270 K. Beyond this temperature, a sharp decrease in signal is noted with a slope greater in magnitude than that estimated via the Boltzmann prediction. This indicates that the radicals are reacting and becoming unstable at this temperature. To see if these radicals could be captured by BT-IPDI, the experiment was repeated with samples containing 0.1 wt% BT-IPDI (Figure 71), which shows a very large signal due to a high concentration of nitroxyl radicals. The decrease in signal almost perfectly matches the Boltzmann prediction in Figure 72. Signal deviation from the Boltzmann prediction at temperatures > 270 K was similar to measured deviations in Figure 70. The high concentration of nitroxyl radicals limits the possibility of detecting any loss in signals resulting from the reaction between nitroxyls and mechano-radicals.

Therefore, the next experiment focused on a DGEBA - 2-methyl-1,5-diaminopentane matrix with optimized loading of nitroxyl radicals (Figure 73).

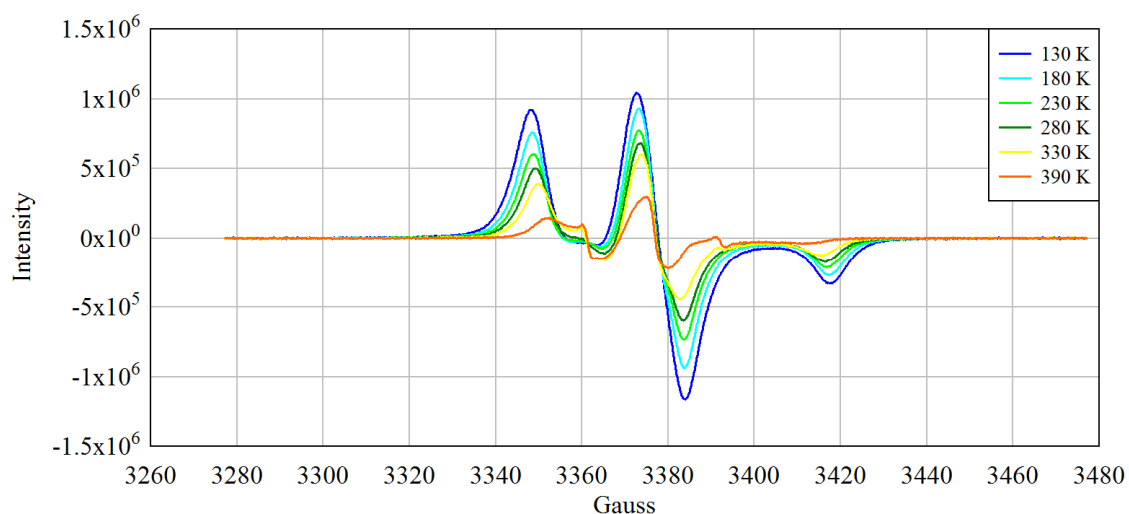


Figure 71. VT-EPR of cryo-ground SC-15 with 0.1 wt% BT-IPDI.

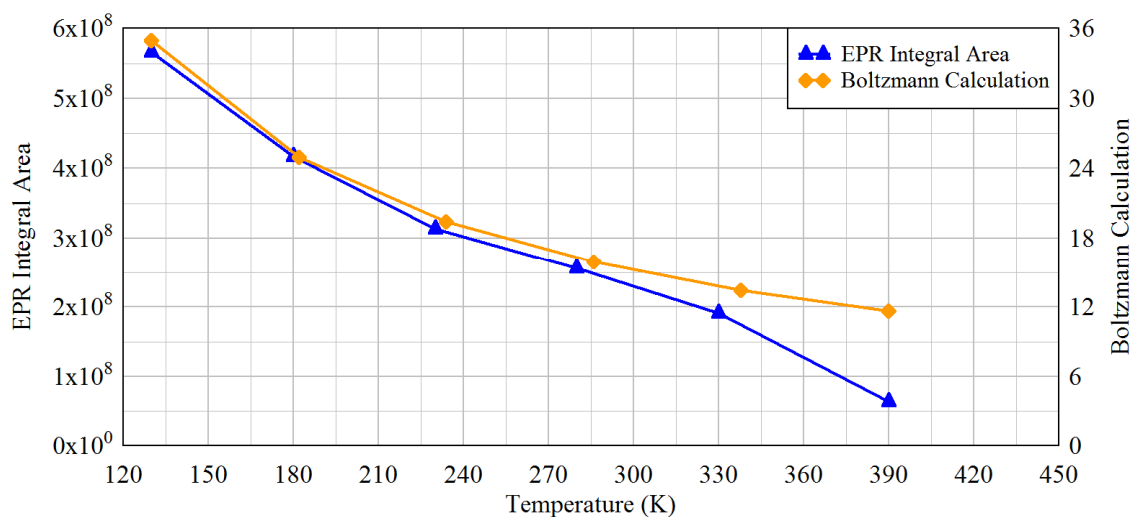


Figure 72. VT-EPR of SC-15 / 0.1 wt% BT-IPDI cryo-ground EPR integral areas compared to Boltzmann statistics calculation for decreasing differences in quantum states with increasing temperature.

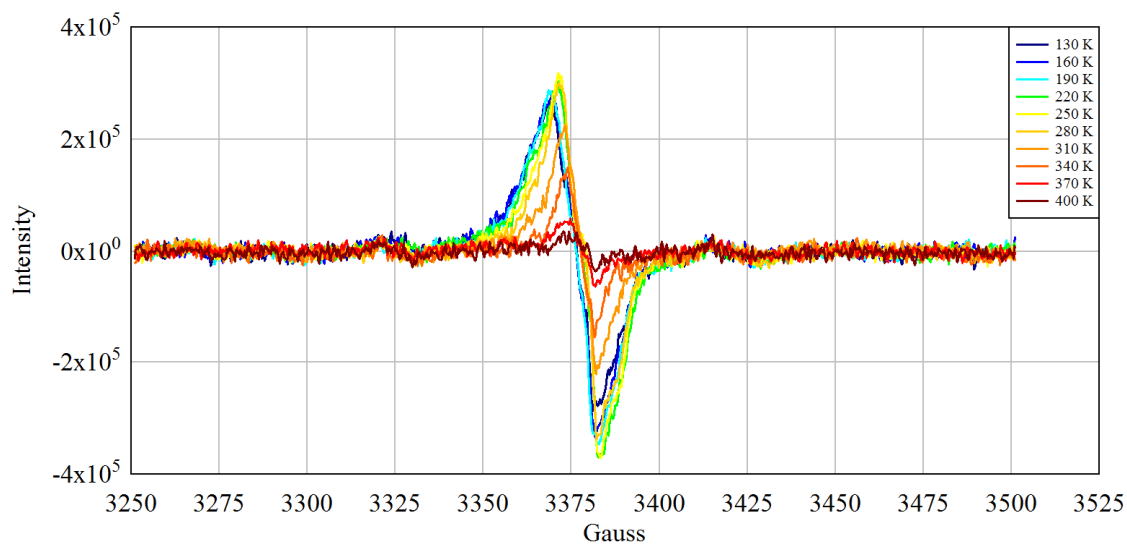


Figure 73. VT-EPR spectra of cryo-ground DGEBA and 2-methyl-1,5-diaminopentane.

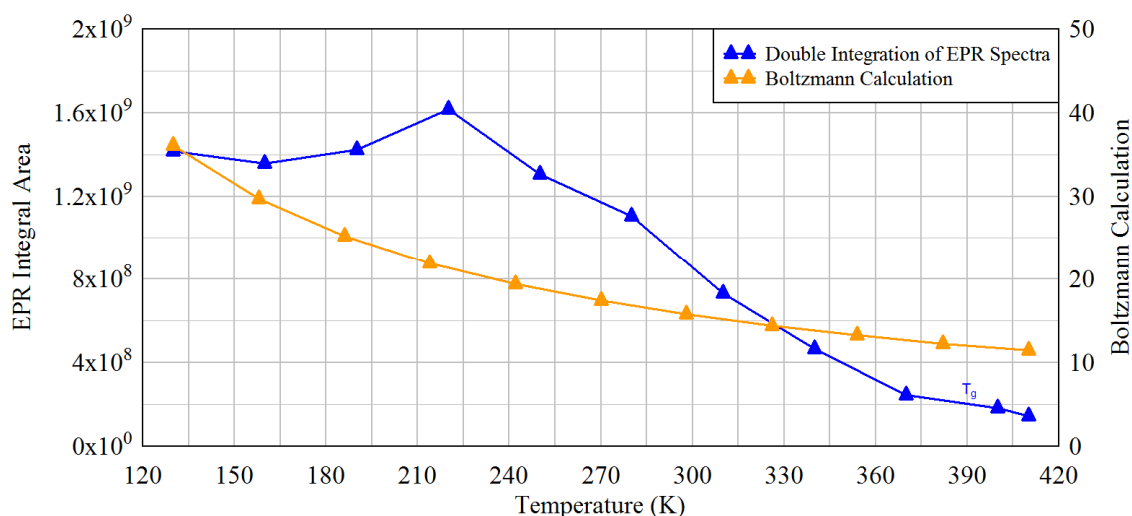


Figure 74. VT-EPR: DGEBA and 2-methyl-1,5-diaminopentane cryo-ground EPR integral areas compared to Boltzmann statistics calculation for decreasing differences in quantum states with increasing temperature.

Figure 74 displays an erratic behavior that was probably not quantitative below 270 K. Sohma and Sakaguchi showed that in this temperature region, the mechano-radical signal is in an unusual state of flux.⁷ The EPR spectra of mechano-radicals routinely show signal increases in these regions, but population increases due to rise in temperature are unlikely. One postulate is that the sample, having been mechanically

ground and deposited into glassware, has built up an electrical charge that is unable to ground causing fluctuations in signals below 270 K.⁷ Researchers have measured the charge of the ground polymer and observed decreased fluctuation in samples that were uninsulated.⁷

Despite the potential cause in fluctuation, 270 K marks a turning point in which the radicals begin to irreversibly lose population. This temperature region which marks the beginning of mechano-radical instability is where nitroxyl and mechano-radical reactions are most likely to occur. Overlaying the mechano-radical spectra from that of samples containing BT-IPDI, it is apparent that the mechano-radical single peak overlays that of the central nitroxyl peak. This presents an opportunity to monitor changes in nitroxyl and mechano-radical population independently of each other. The leftmost nitroxyl peak is directly proportional to nitroxyl signal while the central peak is the sum of the contribution from both the nitroxyl radicals and mechano-radicals. A modulated temperature experiment was conducted to determine if the radical signal changes are reversible due to temperature and if reactions occur between the cryo-ground radicals and the nitroxyl radicals.

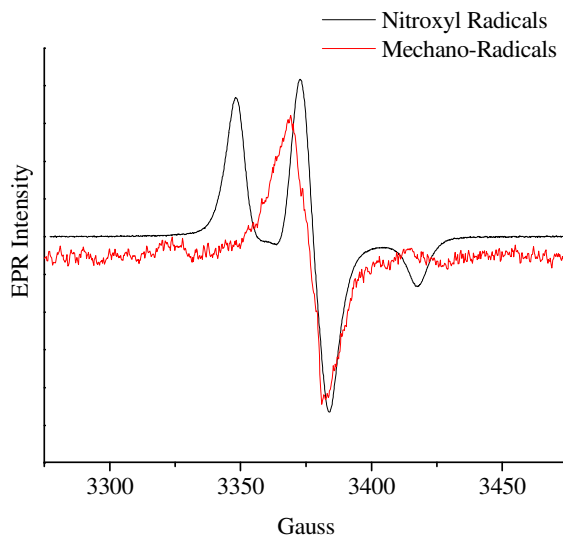


Figure 75. EPR overlay of the nitroxyl radical and mechano-radical spectrums.

To optimize the concentration of nitroxyl radicals and cryo-ground mechano radicals, a loading level of 0.005 wt % BT-IPDI was selected. BT-IPDI was incorporated with DGEBA and cured with 2-methyl-1,5-diaminopentane as previously discussed. The material was cryo-ground and then inserted into the EPR instrument at 130 K. The experiment represented in Figure 76 is a thermally modulated EPR experiment that is difficult to represent graphically. The experiment was initiated at 130 K for the initial spectrum, and then the temperature was increased to 160 K, decreased to 130 K for the second modulated spectrum, increased to 190 K for the initial spectrum, decreased to 160 K for the second modulated spectrum, and so on and so forth. This “leap frog” approach ensures an initial spectra at all temperature points and second modulated spectra at previous temperature points. The initial spectra intensity values are represented in blue and the second modulated intensity values are represented in red. When only one color is visible, it indicates complete intensity overlap and no difference between initial and modulated scans. The half-filled boxes represent the central peak intensity, which is the

nitroxyl / mechano-radical overlap. The open squares represent the intensity values of the nitroxyl side band.

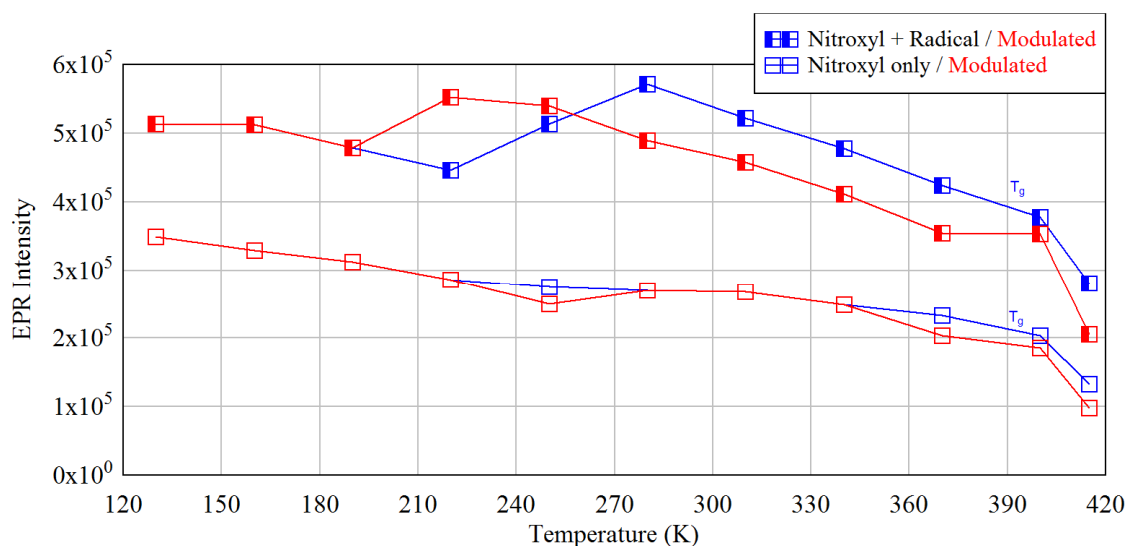


Figure 76. Modulated VT-EPR for cryo-ground DGEBA and 2-methyl-1,5-diaminopentane containing 0.005 wt% BT-IPDI. Red curves indicate the modulated spectra taken after temperature has been increased. Blue curves indicate first spectra at that temperature. Half-squares correspond to the intensity of the nitroxyl and cryo-ground radical overlap. Unfilled squares correspond to the nitroxyl only signal.

Figure 76 also shows the EPR signal fluctuation seen in previous experiments and by other researchers.⁷ Since nitroxyl radicals do not fluctuate in this region, the signal flux from the nitroxyl / mechano-radical overlap must be caused solely by the mechano-radicals. In agreement with the previous Boltzmann calculations in Figure 74, the mechano-radical signal overlap in Figure 76 shows irreversible loss of concentration after the material is heated above 270 K. The loss in concentration of mechano-radicals at 270 K was in agreement with the findings of other researchers.⁷ No irreversible changes occur to the nitroxyl signal until the material is heated above its T_g . From these two conditions, mechano-radicals are reacting above 270 K but not with the nitroxyl radicals. This can be due to several reasons; either the cryo-ground radicals are concentrated at the

surface and unable to react with bulk nitroxyl radicals, or the glassy state is too immobile for the nitroxyl radicals to react with the cryo-ground radicals.

Table 19

Cryo-ground Particle Size Analysis

Property	Amount
Amount of material (g)	0.0306
FEW of broken bonds (g/mol)	436
Density (g/mL)	1.159
Broken bond density (mol/mL)	0.00266
Surface area of particles (cm ²)	126.95
Width of crack (cm)	1×10^{-8}
Volume of crack (mL)	1.27×10^{-6}
Number of broken bonds (mol)	3.38×10^{-9}
BT-IPDI radicals in sample (mol)	5.72×10^{-9}
BT-IPDI radicals at surface (mol)	2.75×10^{-13}

Note: Calculations are made assuming bonds broken from cryo-grinding is the 2-methyl-1,5-diaminopentane molecule residing between the crosslinks which forms two radicals. The width of the crack is assumed to be 1 angstrom.

Table 19 presents a summary of calculations made from particle size analysis using the Zetatrac Particle Size Analyzer (static light scattering) instrument. Although the calculations are based on simple algebraic equations and assumptions, the concentration of broken bonds is experimentally reasonable given the detection capabilities of the EPR instrument. From the estimations, the deficit in concentration of nitroxyl radicals at the particle surface relative to the number of potential broken bonds is

readily apparent. This represents a significant experimental challenge in that increasing the nitroxyl radical concentration would only dilute the signal ratio between nitroxyls and mechano-radicals. Future experiments could investigate finer particle size grinding to maximize the ratio between the two species.

Conclusions

In this chapter, mechanically formed radicals were produced by grinding epoxy-amine thermosets. The temperature dependent characteristics of the mechano-radicals match data reported in literature.⁷ The Boltzmann statistics model was used to predict temperature dependent EPR signal decreases and distinguish between irreversible loss of radical population due to recombination versus reversible decreases in signal due to temperature changes. Modulated EPR was used to determine if reactions between nitroxyl and mechano-radicals occurred. The modulated experiment showed that mechano-radicals decrease in population due to recombination, but they did not detectably react with the nitroxyl radicals of BT-IPDI. Reduction in population of the nitroxyl radicals did not occur until temperatures were increased above the glass transition temperature. Particle size analysis from light scattering revealed the deficit in potential population of surface broken bonds versus that of nitroxyl radicals in the bulk.

Future experiments could increase their potential for success through finer grinds to maximize the mechano-radical to nitroxyl ratio. In these experiments, it was assumed that the radical species is either a carbon-centered radical that, by itself or upon destabilization, forms products that can react with BT-IPDI similar to the Denisov cycle in Scheme 5 of Chapter IV. It is also possible that the liquid nitrogen possesses sufficient liquid oxygen to contaminate the radical products and create peroxy radicals, which

cannot directly react with nitroxyl radicals. Ball milling under both high vacuum and liquid nitrogen temperatures would have to be performed with transfer to an EPR tube also under high vacuum and cryo-temperatures. The equipment to investigate this experimentally would involve cryo-grinding through specially manufactured equipment that is not commercially available as of yet.

REFERENCES

- 1 S.E. Bresler, E.N. Kazbekov & E.M. Saminskii. Macroradical studies in polymerization and degradation processes II. *Polymer Science U.S.S.R.* **1**, 540-50, (1960).
- 2 D.K. Backman & K.L. Devries. Formation of free radicals during machining and fracture of polymer. *Journal of Polymer Science (Part A-1)* **7**, 2125-34, (1969).
- 3 M.A. Grayson & C.J. Wolf. Mechanochemical reactions in an epoxy resin system. *Journal of Polymer Science: Polymer Physics Edition* **23**, 1087-97, (1985).
- 4 M.G. Panek, G.M. Villacorta, W.H. Starnes & I.M. Plitz. Fracture-induced free radicals in amine-cured epoxy resins. *Macromolecules* **18**, 1041-43, (1985).
- 5 M. Sakaguchi & J. Sohma. ESR evidence for main-chain scission produced by mechanical fracture of polymers at low temperature. *Journal of Polymer Science Part B: Polymer Physics Edition.* **13**, 1233-45, (1975).
- 6 T. Kawashima, S. Shimada, H. Kashiwabara & J. Sohma. ESR studies on the molecular mechanisms of fracture of polymers at low temperatures. *Polym. J.* **5**, 135-43, (1973).
- 7 J. Sohma & M. Sakaguchi. ESR studies on polymer radicals produced by mechanical destruction and their reactivity. *Adv. Polym. Sci.* **20**, 109-58, (1976).
- 8 M.B. Smith & M. Jerry. *March's Advanced Organic Chemistry: Reactions, Mechanisms, and Structure.* (John Wiley and Sons, Inc, 2007).
- 9 G.R. Eaton, S.S. Eaton, D.P. Barr & R.T. Weber. *Quantitative EPR.* (Springer, 2010).

CHAPTER VI
INVESTIGATION OF TENSILE PLASTIC FLOW AND FRACTURE
MORPHOLOGY OF A GLASSY EPOXY-AMINE THERMOSET

Introduction

In Chapter 4, mechanical experiments were conducted using specific rectangular shapes that were ideal for EPR spectroscopic analysis. Due to the negative results produced from those studies, it was decided that testing an ASTM Type V dogbone shape, a standard shape for mechanical experiments, would result in more consistent property degradation. The Type V dogbone is larger than sample dimensions used previously, and the hourglass shape is designed to concentrate deformation and stress within the neck region and away from the mechanical grip – sample interface. Samples were manufactured and tensile testing was performed to determine the ultimate tensile strength. However, unusual mechanical behavior for glassy epoxy thermosets was observed as shown in Figure 77.

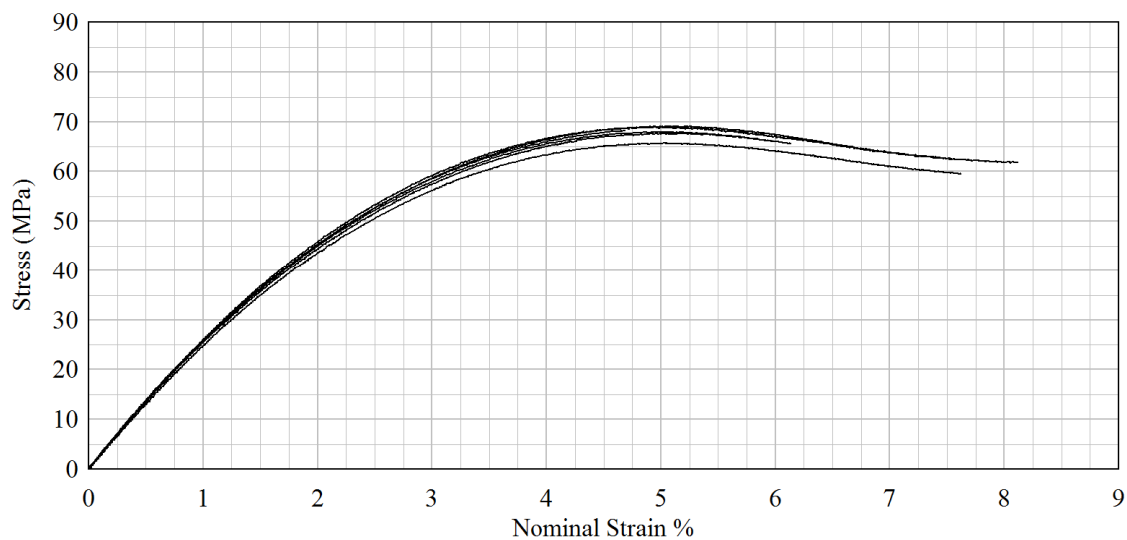


Figure 77. Tensile stress-strain curve of DGEBA-2-methyl-1,5-diaminopentane Type V dogbones.

Stress-strain terminology and its relation to the measured stress-strain curve is depicted in Figure 78. Yielding and plastic flow behavior within tensile stress-strain curves is common to linear glassy polymers such as polymethyl methacrylate (PMMA), polycarbonate (PC), poly(ethylene terephthalate) (PET), and many others. For linear glassy polymers, plastic strains can occur through shear banding and cold drawing.¹ Considering the highly crosslinked backbone structure of glassy epoxy thermosets and the occurrence of plastic flow, the obvious question is what is the structural origin of this mechanical behavior?

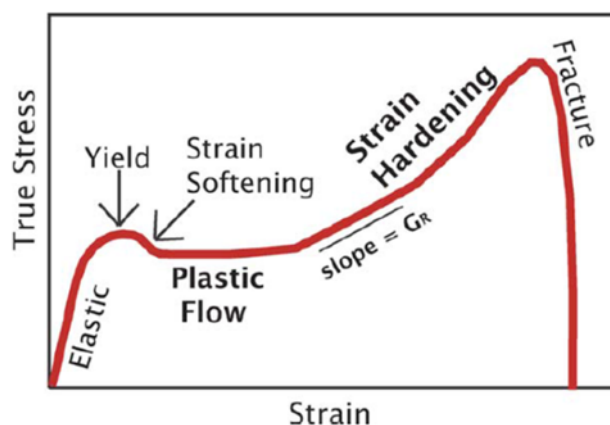


Figure 78. Stress-strain terminology. Why is understanding glassy polymer mechanics so difficult, by R.S. Hoy, 2011, *Journal of Polymer Science Part B: Polymer Physics*, volume 49, p. 979. Reprinted with permission from the publisher.²

Glassy epoxy thermosets are viewed within the polymer discipline as brittle thermosets possessing low fracture toughness, tensile elongation to breaks of approximately 5-7%, and lacking yield characteristics of linear engineering polymers. The plastic flow behavior in Figure 77 has been often reported for crosslinked epoxies mechanically tested in compression deformation. In their recent review on epoxy polymers and aging, Odegard and Bandyopadhyay state that glassy epoxy thermosets do not exhibit yield in tensile measurements.³ This unchallenged statement is reinforced

through the visualization of the highly crosslinked network possessing little mobility with regards to strain.

Furthermore, unusual fracture surfaces were observed. Test specimens exhibiting plastic flow resulted in mirror-like finishes, whereas samples that failed during yield or strain softening regions possessed notably rough surfaces. These rough surfaces are denoted as mirror-mist-hackle fracture topography. Figure 79 depicts the mirror-mist-hackle topography and labels the fracture zones from whence the name arises. Crack initiation begins in the mirror region and propagates outwards increasing in speed and roughness.⁴

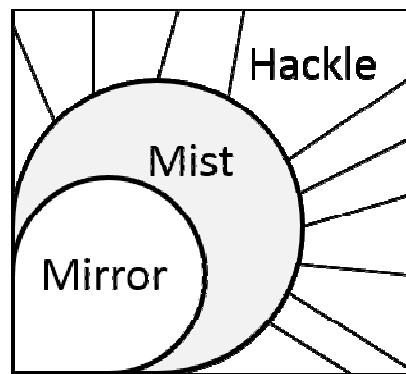


Figure 79. Mirror-mist-hackle topography.

Samples experiencing failure within the plastic flow region did not form mirror-mist hackle surfaces but instead formed completely smooth mirror surfaces resembling polished glass. Specimens failing prior to plastic flow with expected glassy epoxy mechanical behavior produced mirror-mist-hackle surfaces as depicted in Figure 79.

The research within this chapter seeks to understand if plastic flow is a requirement for these mirror surfaces to form. Plastic flow represents a viscous deformation. If the capacity of the epoxy to experience plastic flow was eliminated, would the complete mirror fractures still occur? In these experiments, physical aging was

used as a tool to inhibit the viscous movement of the epoxy without altering the epoxy thermosets' mechanism of chemistry, degree of conversion, or crosslink density.

The glassy state is a thermodynamic, non-equilibrium state of amorphous polymers. Physical aging occurs as a glass slowly approaches its equilibrium state and is characterized by increasing density and changes in molecular configuration represented in Figure 80.⁵ Property changes include decreases in toughness, visco-elastic response, and permeability.³ Physical aging can be accelerated by thermally annealing materials within 10 to 15°C below T_g .⁵

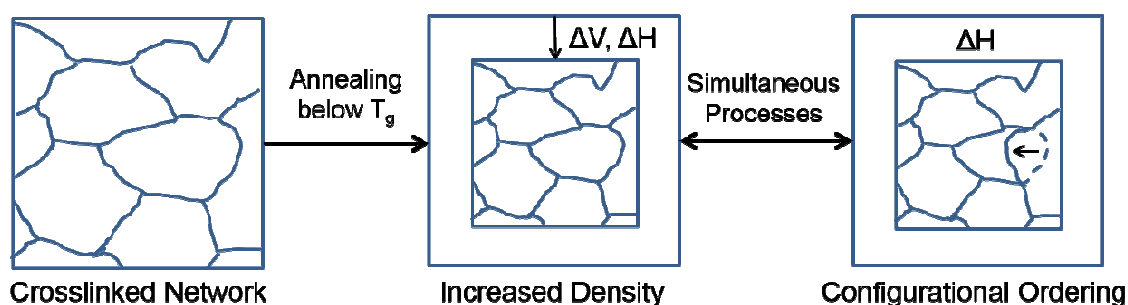


Figure 80. Physical aging resulting in simultaneous decreases in specific volume (V) and excess enthalpy (H).

It is hypothesized that plastic flow of the glassy thermoset occurs through the existence and deformation of structures within the network. Upon complete deformation of the structures, smooth plane fracture through the specimen will occur. To test this hypothesis, physical aging of the network will restrict mobility of these structures, thereby reducing the yield behavior and promoting the formation of rough fracture surfaces.

Experimental

Vacuum degassed DGEBA and 2-methyl-1,5-diaminopentane were blended in 2:1 molar ratios, mixed, degassed via sonication, and cast into test-specific molds.

Formulations were vitrified overnight under ambient conditions and post-cured at 60 °C for 75 min followed by 120 °C for an additional 75 min. Samples were polished first with 600 and then 800 grit sandpaper to remove any edge defects. Physical aging treatments were conducted at 95 °C (10 °C below T_g) under nitrogen purge for up to ten days. The DSC and TGA experiments were conducted at 10°C/min heating rates, whereas the heating rate for DMA was 2 °C/min. The DSC physical aging analysis was conducted via a heat - quench - heat procedure with the quench stage decreasing at a rate of 50 °C/min. Monotonic tensile testing was performed on Type V ASTM D638 dogbones at a testing speed of 0.762 mm/min. Non-Aged samples were tested on a BOSE Electroforce equipped with 3.3 kN loadcell. Additional samples were aged for 10 days, denoted as Aged-10 Days, and tested on an MTS Insight Series equipped with a 2.5 kN loadcell.

Results

There are potential sources or causes of thermoplastic behavior in stress-strain characterization that should be eliminated from consideration. Viscous mechanical behavior could be attributed to samples being in a state of incomplete cure or possessing plasticizers. To verify that the samples are “fully” cured, isothermal DSC analysis of the epoxy-amine thermal cure profile was employed.

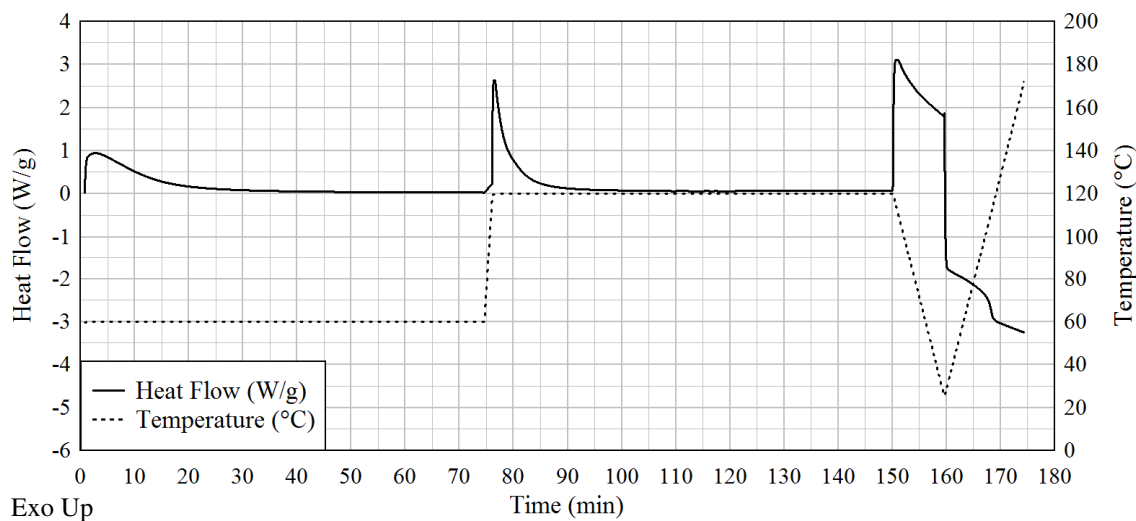


Figure 81. DSC isothermal scan of DGEBA and 2-methyl-1,5-diaminopentane cure temperatures followed by temperature sweep to 180 °C. Exothermic reaction ceases after approximately 25 min at 120 °C.

In Figure 81, DSC samples were prepared exactly according to the procedure listed in the methods section with the caveat of not being exposed to the oven curing procedure. Figure 81 shows the exothermic epoxy-amine reaction proceeding at 60 °C before re-thermally curing and diminishing. Increasing the temperature to 120 °C finishes the reaction in approximately 25 min. Cooling the sample to 25 °C and then thermally sweeping the sample to 180 °C reveals the T_g at 105 °C and does not detect additional exothermic reaction at the higher temperatures.

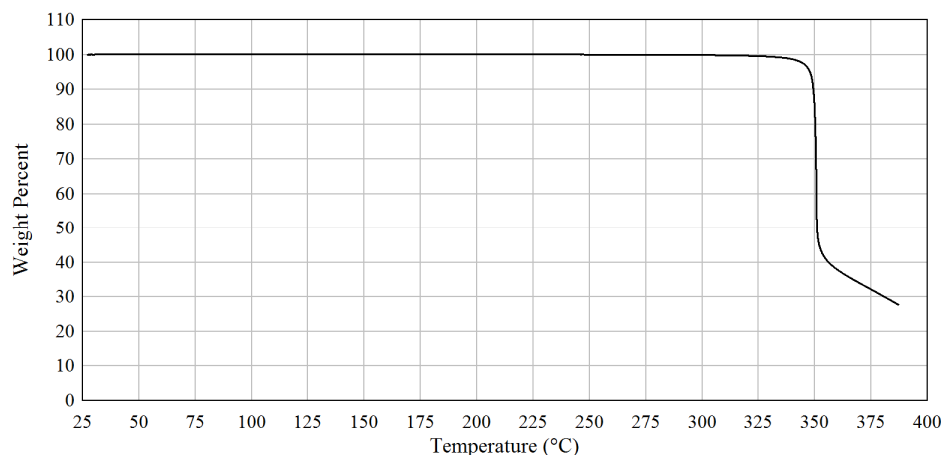


Figure 82. TGA thermal sweep of DGEBA-2-methyl-1,5-diaminopentane. No detection of volatile monomers, solvents or plasticizers.

Another potential source for viscous behavior would be contamination of the matrix with plasticizing agents such as volatile solvents. TGA was employed to detect these potential contaminants. In Figure 82, samples were prepared and post cured exactly according to the procedure listed in the methods section. In Figure 82, the TGA curve shows no degradation of the epoxy-amine network until approximately 350 °C. Maintaining 100 %wt. until this point strongly indicates the absence of volatile monomers, solvents, or plasticizers within the detection limits of TGA. From DSC and TGA, the epoxy-amine thermoset is “fully” cured and absent volatile contaminants, which could produce viscous deformation.

To determine an appropriate aging protocol, samples were physically aged at 95 °C (10 °C below the glass transition temperature) under nitrogen purge for varying times to determine an optimal procedure. Within the DSC first heating cycles in Figure 83, the increase in enthalpy of recovery can be detected after only one day of aging. As a glass ages, it releases excess enthalpy through configurational ordering. Once the material is heated to the glass transition, the enthalpy must be regained as it transitions into the

rubbery state producing an enthalpic signature within DSC traces. This enthalpic recovery increases with the extent of the aging time. For the purposes of this study, 10 days was selected as an appropriate time to age the samples.

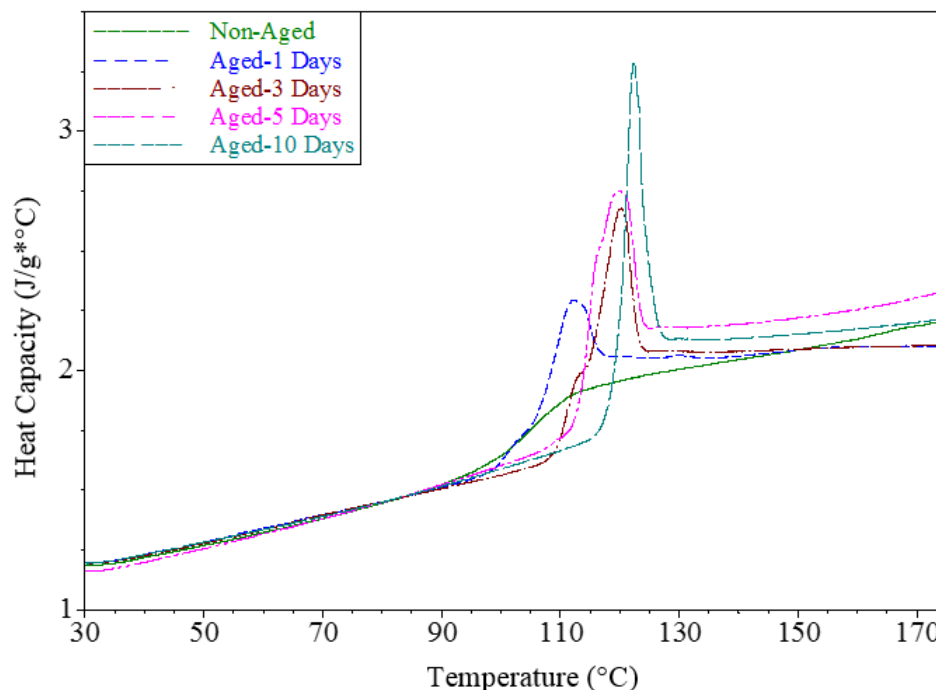


Figure 83. First heating cycles of aged samples showing increasing enthalpic recovery with aging time.

The aging procedure was conducted under nitrogen purge to eliminate thermal oxidative degradation and atmospheric moisture adsorption. The first heating cycle should erase the thermal history of the sample. The second DSC heating cycles were employed to detect if any permanent changes to the glass transition temperature occurred as a function of the aging treatment. From Figure 84, the second heating cycle reveals a linear time based increase in T_g with aging time. This could represent several factors including thermal oxidation, increases in cure of the epoxy-amine reaction, and incomplete erasure of the thermal history from the first DSC heating cycle.

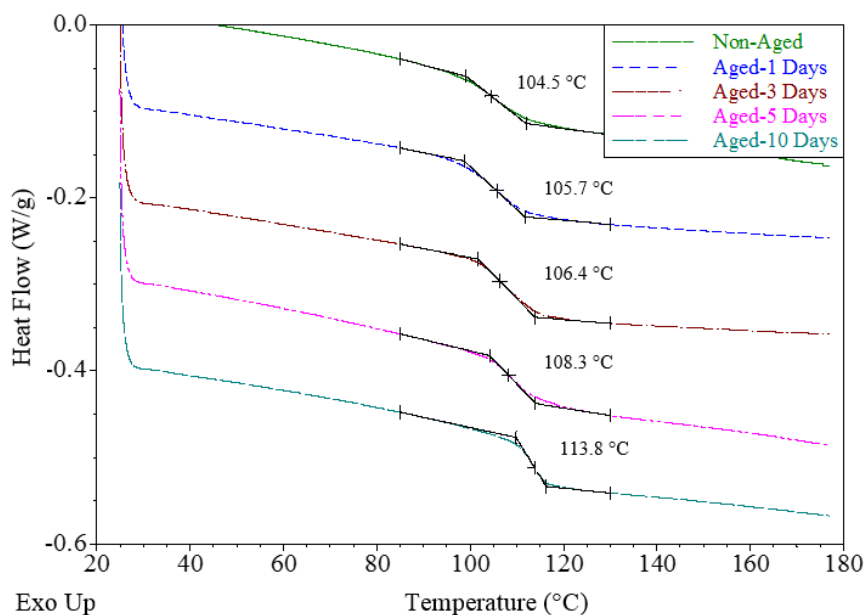


Figure 84. Second heating cycles of aged samples revealing increasing T_g from physical aging treatment.

Dynamic mechanical analysis was employed to discern between the possible explanations of the increasing T_g in Figure 84. The DMA samples were prepared and post cured according to procedure then aged at 95 °C for 10 days under nitrogen purge. From Figure 85, the mechanical thermal transitions completely overlay between the Non-Aged and Aged-10 Days samples as shown in Table 20.

Table 20

DMA Mechanical Thermal Transitions for Figure 85

Sample	Storage Modulus Onset (°C)	Peak Loss Modulus (°C)	Peak Tan δ (°C)
Non-Aged	107.5 \pm 0.35	111.4 \pm 0.36	118.4 \pm 0.15
Aged-10 Days	106.9 \pm 0.28	110.7 \pm 0.19	118.4 \pm 0.65

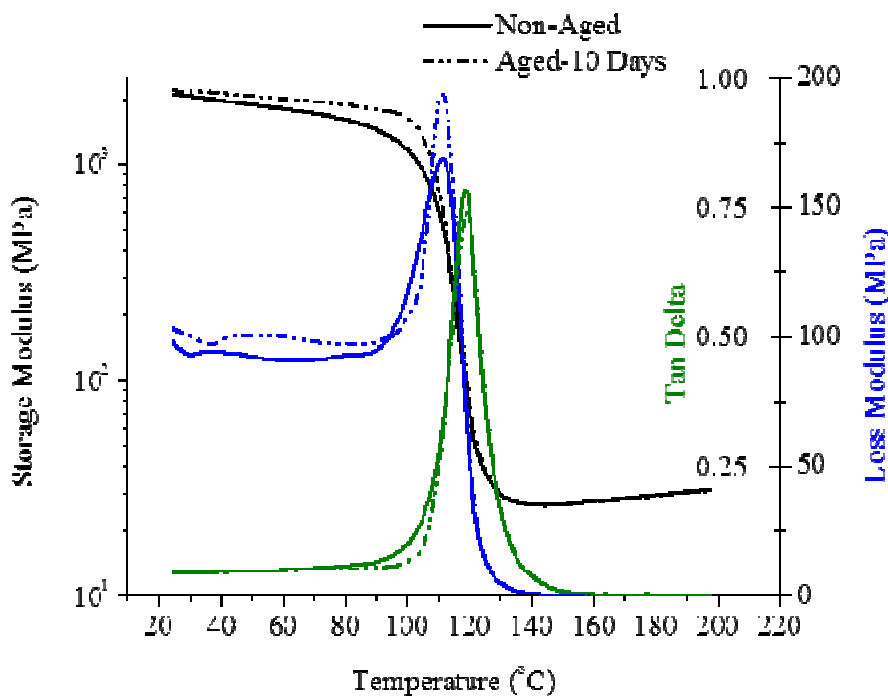


Figure 85. DMA thermal sweeps of Non-Aged and Aged-10 Days samples. T_g and crosslink density remain constant.

The three primary DMA T_g measurements (Table 20) were observed to be constant regardless of the aging treatment. This supports that T_g increases observed in Figure 84 are not likely due to chemical changes in the network. This excludes the possibilities of oxidative degradation and incomplete cure causing the increases in T_g seen in Figure 84. The unchanged T_g and trends in magnitudes of increased storage modulus, increased loss modulus, and decreases in $\tan \delta$ match previously reported results for physically aged epoxy-amine thermosets and DMA analysis.^{3,6} Authors have not explained why “apparent” T_g shifts are not observed in DMA from physical aging treatment. It is likely that the mechanical forces of DMA quickly facilitate the removal of physically aged thermal history.

To further examine the potential of chemical changes causing the data observed in Figure 84, the crosslink density was calculated using the rubber elasticity theory

(Equation 12). The density of DGEBA – 2-methyl-1,5-diaminopentane was experimentally determined from the PVT experiment conducted in Chapter II and is 1.0918 g/mL at 176 °C. The theoretical crosslink density (M_c) for this network is 436 g/mol while the measured M_c from DMA data for Non-Aged was 412 ± 9 g/mol and Aged-10 Days was 415 ± 11 g/mol.

$$M_c = \frac{3\rho RT}{E}$$

Equation 12. Crosslink density calculation using storage modulus and density. M_c is crosslink density in g/mol. E is storage modulus. T is temperature in Kelvin. P is density. R is the gas constant.

The DMA experiments revealed identical glass transition temperatures and crosslink densities from Non-Aged and Aged-10 Days samples. These results exclude explanations of oxidative degradation and incomplete cure of the epoxy-amine network from the underlying causes of T_g increase in Figure 84. Incomplete thermal history erasure remains as the likely explanation of the Figure 84 results. Literature uses dwell times in which the temperature is held above T_g for 15 minutes to remove all of the aging effects before subsequent heat cycles. It was incorrectly assumed that thermally sweeping to the elevated temperature of 180 °C would be sufficient to erase all previous thermal history.

Since DMA confirmed that the epoxy-amine networks were not altered chemically from physical aging treatments, stress-strain data was collected with monotonic tensile testing of type V ASTM D638 dogbones as depicted in Figure 86. Fracture images were captured using the Keyence microscope.

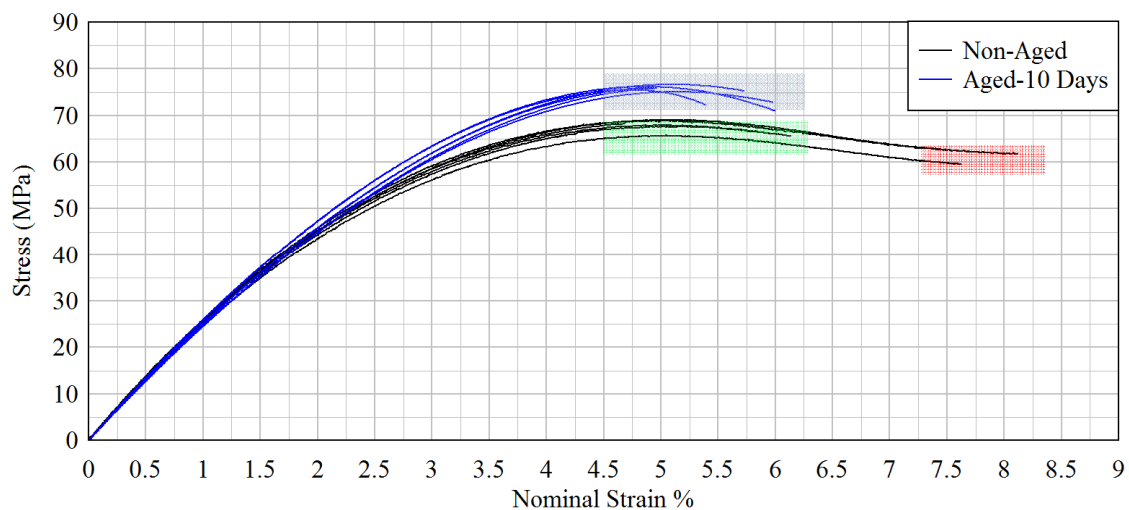


Figure 86. Tensile stress-strain curves of Type V ASTM D638 dogbones. Highlighted sections correlate fracture surfaces to strain at break shown in Figures 87-89.



Figure 87. Non-Aged fracture surfaces correlated to the yield region in Figure 86.



Figure 88. Non-Aged fracture surfaces correlated to the plastic flow region in Figure 86.

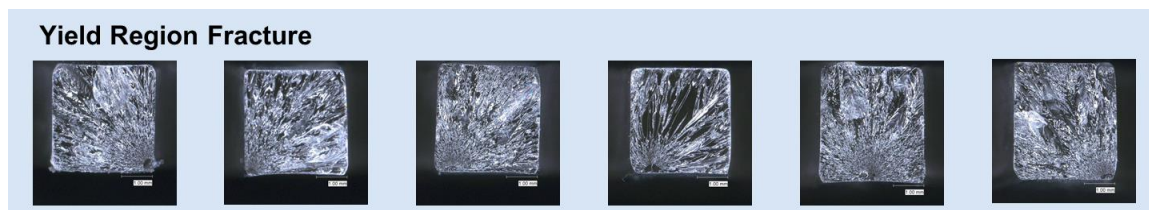


Figure 89. Aged-10 Days fracture surfaces correlated to the yield region in Figure 86.

In Figure 86, stress-strain curves of Aged-10 Days samples exhibited an increased stress at break, a decreased strain at break, and an elimination of plastic flow behavior in comparison to Non-Aged samples. The modulus of the epoxy-amine thermoset was not affected by the physical aging treatment and was consistent with literature results.³ Samples failing during the yield region of Non-Aged and Aged-10 Days specimens produced fracture surfaces (Figures 87 and 89) labeled as mirror, mist, and hackle depicted in Figure 79.⁴ Non-Aged samples undergoing plastic flow exhibited only mirror-like fracture surfaces (Figure 88). This suggests that the crack tip was not redirected due to local stress concentrations. Integration of max strain curves of Aged-10 Days and Non-Aged yields a 35% decrease in the simple toughness resulting from the physical aging treatment. Literature suggests correlation between the increasing size of the mirror region and increasing toughness.⁴

Physically aging the epoxy-amine network eliminated the capacity of plastic flow as evidenced from the stress-strain curves in Figure 86. The resulting fracture surfaces were all composed of the mirror-mist-hackle topography. This confirms the relationship between the atypical viscous mechanical behavior and the atypical fracture surface. This links the viscous deformation being required for both observations, but viscous deformation of what? The deformation could result from the alignment of chain segments, but in a highly crosslinked glassy network, this seems unlikely. It was

hypothesized that the results indicate the existence of a physical structure feature capable of viscous deformation. The identity, size, and shape of the structure is unknown; therefore, atomic force microscopy (AFM) and scanning electron microscopy (SEM) were employed to image fracture surfaces at nanometer scales.

Microscopy

The AFM images were collected using a Bruker Dimension Icon operating in tapping mode with Bruker RTESP probes (0.01 - 0.025 Ω cm Antimony (n) doped silicon probe, spring constant: 20-80 N/m). Scanning electron microscopy images were collected using a Zeiss Sigma Variable Pressure, Field Emission Gun Scanning Electron Microscope (VP-FEG-SEM) with Thermo energy dispersive and wavelength dispersive X-ray detectors (EDS/WDS) at an acceleration voltage of 10 kV. Mirror fracture surfaces from Figure 88 were then mounted and scanned by SEM and AFM. Samples used for SEM analysis were sputter coated with silver at instrument reported thickness of 5 nm.

Analysis of the mirror fracture surfaces from Figure 88 through AFM and SEM revealed a nodular morphology (Figure 90 and 91). The images from both of these methods correlate nodule size in the 50 nm range. The SEM images in Figure 91 show the nodules to be an almost wormlike tendril network of separate domains. These images reveal multiple layers of this structure through the nooks and crevices residing in the image. The AFM results agree very well with SEM. However, the tip is unable to resolve the depth of the nooks due to the width of the wedge shaped tip. The tip radius is a reported 8 nm, thus the failure to penetrate to the full depth of the sample crevices was most evident within the phase images in Figure 90. The height image reveals a nodular morphology, but the phase image shows 0 phase (dark brown) in many areas. This is due

to the wedge shape tip contacting multiple areas of the sample at once as it attempts to measure the depth of a crevice. Nodular morphology has been reported by many researchers within the epoxy-amine discipline, and its existence as a true representation of the epoxy-amine bulk morphology is disputed. The literature background of nodule morphologies within epoxy-amine thermosets will be discussed in the next chapter.

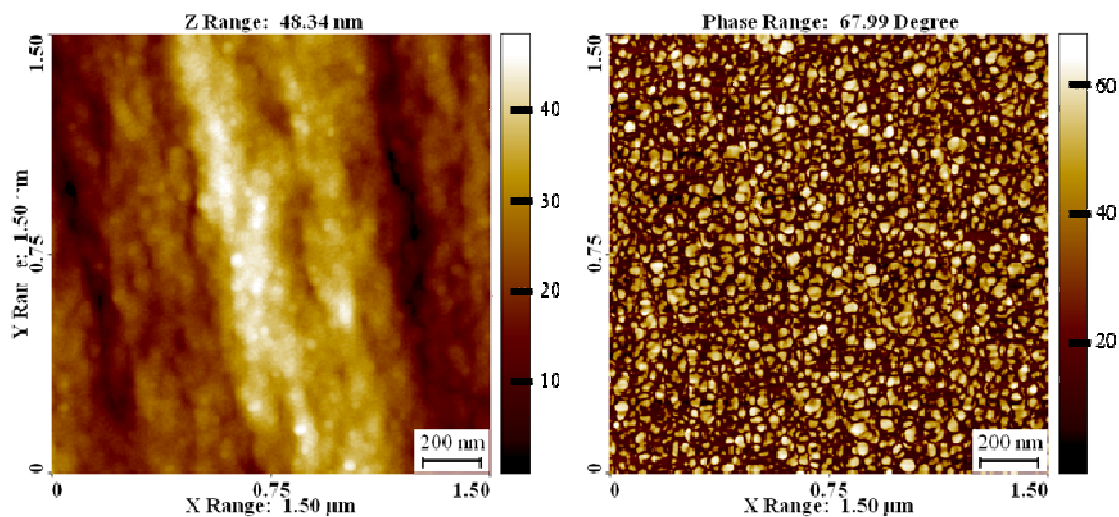


Figure 90. AFM images of DGEBA - 2 methyl-1,5-diaminopentane resulting from tensile fracture. Images in the left column are height images, whereas the images in the right column are phase images.

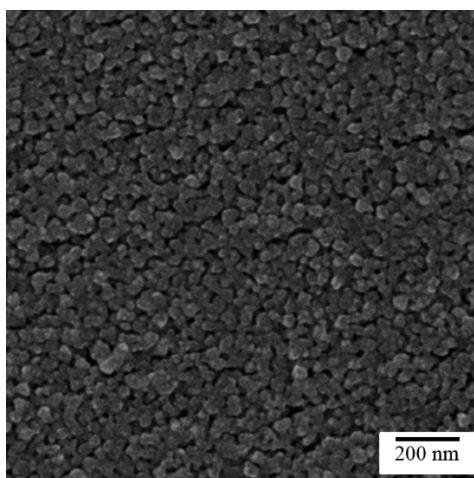


Figure 91. SEM images of DGEBA / 2 methyl-1,5-diaminopentane resulting from tensile fracture.

Conclusions

Reproducible and uncharacteristic tensile stress-strain behavior of cured glassy epoxy-amine networks were observed to produce distinctive fracture surfaces. Test specimens exhibiting plastic flow resulted in mirror-like finishes, whereas samples that failed during yield or strain softening regions possessed notably rough surfaces. It was

hypothesized that viscous deformation was required to form the atypical complete mirrored fracture surfaces. By using physical aging as an investigative tool, it was possible to eliminate the capacity of the epoxy-amine network for viscous deformation without adversely altering the polymer structure through chemical means. The elimination of plastic flow resulted in the elimination of smooth fracture surfaces thus correlating the relationship between the atypical mechanical behavior and atypical fracture surfaces. The results indicate the potential existence of a structural feature capable of viscous deformation.

The AFM and SEM images revealed wormlike nodule type structures at the 50 nm size scale. We hypothesize that these structures, as seen in Figures 90 and 91, are the underlying cause of the unusual mechanical yield behavior and atypical mirror fracture surfaces. The development of the morphology and its impact on mechanical properties will be investigated in the next chapter.

REFERENCES

1. Z. Bin Ahmad & M.F. Ashby. Failure-mechanism maps for engineering polymers. *J. Mater. Sci.* **23**, 2037-50, (1988).
2. R.S. Hoy. Why is understanding glassy polymer mechanics so difficult? *Journal of Polymer Science Part B: Polymer Physics* **49**, 979-84, (2011).
3. G.M. Odegard & A. Bandyopadhyay. Physical aging of epoxy polymers and their composites. *J. Polym. Sci., Part B: Polym. Phys.* **49**, 1695-716, (2011).
4. D. Hull. *Fractography: Observing, Measuring and Interpreting Fracture Surface Topography*. (Cambridge University Press, 1999).
5. J.M. Hutchinson. Physical aging of polymers. *Progress in Polymer Science* **20**, 703-60, (1995).
6. L. Barral, J. Cano, J. Lopez, I. Lopez-Bueno, P. Nogueira, M.J. Abad & C. Ramirez. Physical aging of an epoxy/cycloaliphatic amine resin. *Eur. Polym. J.* **35**, 403-11, (1998).

CHAPTER VII
CHEMORHEOLOGY INVESTIGATION OF A GLASSY EPOXY THERMOSET ON
TENSILE PLASTIC FLOW AND FRACTURE MORPHOLOGY

Introduction

In Chapter VI, reproducible and uncharacteristic tensile stress-strain behavior of cured glassy epoxy-amine networks produced distinctive fracture surfaces. Test specimens exhibiting plastic flow resulted in mirror-like fracture surfaces, whereas samples that failed during yield or strain softening regions possessed nominal mirror-mist-hackle topography. Atomic force microscopy and SEM revealed tendril nodule morphologies in the 50 nm size scale that may be responsible for the unusual tensile properties. It is hypothesized that plastic flow of the glassy thermoset occurs through the existence and deformation of these nodular nanostructures. The experiments within this Chapter seek to understand the causes that lead to the formation of nodule morphology and the impact it has on the mechanical properties of the epoxy-amine thermoset.

Epoxy resin is an important industrial material as its multiple reaction pathways facilitate a variety of chemistry options and comonomer selections that enable broad tailoring of the T_g , mechanical stiffness, surface adhesion, chemical resistance, and corrosion barrier properties. Epoxy-amine thermosets are able to deliver broad tunability and high performance through high reactivity, robust chemistry, and excellent property development even at incomplete conversion while maintaining affordability.

Mechanical properties are governed by the molecular structure and architecture of the polymer matrix.¹ The structure controls rigidity of the repeating backbone, number and strength of intermolecular forces, molecular and polymer strand density, crosslink

density, free volume, and the T_g . These parameters drive the final bulk properties of the material through a variety of interactions. Marks and Snelgrove measured decreasing mechanical properties of epoxy-amine thermosets with increasing conversion.² Literature reported results have been consistent^{2,3} in that properties such as modulus and fracture toughness diminish as conversion increases from 0.8 to 1.0. Marks measured the phenomenon using several amine monomers ranging from aliphatic to aromatic selections.² The measured decrease in modulus was 25% or greater while advancing the epoxy-amine conversion from 0.9 towards 1.0 and was consistent across multiple amine monomer types. Due to the wide assortment of monomers, the cure temperatures varied widely, yet the property loss trend was consistent and could not be explained by the occurrence of competing side reactions. The authors proposed that the loss of properties with increasing conversion originated from decreasing intermolecular forces and inefficiency of polymer glass packing.

Sahagun and Morgan showed *via* AFM that epoxy-amine thermosets exhibit detectable heterogeneous microstructures on the 50 nm scale.^{4,5} Earlier studies supported these observations *via* electron microscopy of various epoxy-amine polymers⁶⁻⁹ and other thermosets.¹⁰ However, dissenting authors argued that the electron beam was responsible for these heterogeneous surfaces through surface etching.¹¹ Sahagun and Morgan observed that in the absence of etched surfaces *via* atomic force microscopy, heterogeneous nanostructures were present within crosslinked epoxy-amine polymers. The nanostructures formed at the gel point and continued to develop throughout conversion up to vitrification.⁴ The authors hypothesized that the nodular morphology originated between regions of high crosslink density and low crosslink density as a part

of the complex diffusion-vitrification limited processes arising from infinite molecular weight at the gel point.⁵

Haba *et al.* proposed a counter argument stating that the nodule morphology detected by AFM could result from an artifact known as tip convolution. Tip convolution artifacts occur when AFM tip sizes are large relative to the surface features causing non-spherical surface features to appear as spherical nodules.¹² The author showed the size of the apparent nodule morphology was affected by the AFM tip radius and concluded that the nodule morphologies detected within glassy thermosets were likely not indicative of real surface features. Although Haba *et al.* used a chain growth polymerization and did not report characterization of the epoxy-amine monomers or thermoset, the author was able to show surfaces with uniform surface modulus through ultra-microtoming.¹²

The contribution of epoxy-amine morphology to mechanical properties is poorly understood but relevant as recent literature has indicated that controlling and altering the morphology may improve strain-to-failure for epoxy-amine thermosets without diminishment of modulus.¹³ The research reported herein seeks to quantify and understand the effect of epoxy-amine morphology on its mechanical properties.

Experimental

In this Chapter, we seek to understand how the morphology develops within the epoxy-amine thermoset and the mechanical properties it affects. Dynamic rheology and FT-NIR will be used to track the conversion of the epoxy-amine reaction at the various stages of sample manufacture that have been used previously. Images will be captured through both AFM and SEM to measure the formation and development of the morphology throughout the cure process. By quantifying both the chemical structure

changes through NIR and the morphology changes through AFM and/or SEM, we can attempt to correlate contributions towards mechanical properties.

Synthesis

Epoxy-amine thermosets were prepared by blending vacuum degassed diglycidyl ether of bisphenol-A (Epon[®] 828, Momentive) and 2-methyl-1,5-diaminopentane (Sigma-Aldrich) in a 2:1 molar ratio, degassed through sonication, and cast into test-specific molds. The resin blends were cured for 15 hours under ambient conditions then post-cured for the specified time and temperature under nitrogen. Four distinct cure profiles were selected to create samples with specific characteristics targeting varying conversion values, mechanical properties, and morphology differences. Samples cured at ambient for 15 hours were designated as α . Samples cured at ambient for 15 hours and post-cured for 75 min at 60 °C under nitrogen were designated β . Samples that were cured at ambient for 15 hours and post-cured for 75 min at 60 °C and 75 min at 120 °C under nitrogen were designated as γ . Finally, samples that were cured at ambient for 15 hours and post-cured for 75 min at 60 °C and 195 min at 120 °C under nitrogen were designated as δ . Additionally, a thermal cure profile was designed to eliminate vitrification from the cure process during polymerization. The thermal profile was designed using rheological data from Figure 93, and was ambient for 4 hours, 20 minutes at 60 °C, and 3 hours at 120 °C under nitrogen atmosphere. This thermal profile is designated as non-vitrification (NV).

Mechanical Testing

Mechanical testing samples were prepared and tested using ASTM D638-10 procedure for Type V dogbone-shaped samples. Samples were polished first with 600 and then 800 grit sandpaper to diminish edge defects that are known to facilitate premature failure during tension testing. Monotonic tensile testing was performed at a testing speed of 0.75 mm/min on an MTS Insight Series equipped with a 2.5 kN load cell with 28.5 mm gauge length.

Bonded strain gauges were applied to the test region center using cyanoacrylate as per the manufacturer's suggestion (Omega, Stamford, CT). Tri-axial gauges were applied to one side of the sample to capture axial, bias, and transverse strain data. The adhesive bonded gauge was allowed to rest at ambient for at least one hour before testing. Resistance strain data was captured at a rate of 100 points per second throughout the MTS test period. The mechanical MTS data capture rate was set to 10 per second. The initiation of the test cycle was synchronized to the failure point in both test methods.

Digital image correlation experiments were conducted using a GOM Optical Measuring Techniques ARAMIS 3D Deformation Analysis System (Trilion Quality Systems). The high visual contrast surface needed for the image capture technique was created by using a "speckle coat" technique. The surface pattern was created using a basecoat of white acrylic latex and speckled with black aerosol commercial paints. The water-based acrylic latex basecoat minimized solvent exposure from the aerosol with the test sample surface. Gray scale images were captured with two 2M digital CCD cameras with 50 mm lenses at one frame per second. Capture volume was calibrated with calibration panels (15 mm x 12 mm) supplied by Trilion Quality Systems.

Fracture toughness specimens were created by casting into rectangular shapes measuring 7 mm x 15 mm x 75 mm. Testing was performed using three point bend geometry with a span of 59.2 mm (4xW) and a testing speed of 0.75 mm/min on an MTS Insight Series equipped with a 2.5 kN load cell. The specimens were then machined to remove surface defects and pre-notched according to ASTM D 5045-99. Samples were tested and K_{IC} values calculated according to section A1.4 of ASTM D 5045-99.

Thermal Characterization

Oscillatory rheometric experiments were performed on an ARES-G2 from TA Instruments, Inc. using 8 mm parallel plates at a frequency of 1 Hz. The auto-strain feature and axial force adjustment was used to prevent damage to the instrument and capture the full cure of the epoxy thermoset. The rheological experiments were staged in multiple phases to match the controlled cure conditions experienced by the mechanical test specimens. The experiment began with the sample mixed and loaded onto the rheometer. The forced air convection oven was turned off and the sample was cured for 15 hours at ambient. The auto-strain settings were set to 0.001% min to 10% max with minimum transducer force of 0.1 g-cm and a maximum of 25 g-cm. The axial force was in tension mode set to 0 g with a max of 10 g. The forced air convection oven was then ramped to 60 °C at 15 °C/min using nitrogen gas as a precise heating source and inert atmosphere. The auto-strain settings were changed to a minimum transducer force of 0.1 g-cm to a maximum of 100 g-cm. The sample was held at 60 °C for 75 min, ramped to 120 °C at 15 °C/min and held for 195 min, ramped to 176 °C at 15 °C/min and held for 15 min. The axial force was changed to compression mode and set to 0 g with a max of 10 g. The sample was then cooled from 176 °C to 25 °C at 2 °C/min.

Dynamic mechanical analysis was performed using a DMA Q800 (TA Instruments, Inc.) in tension mode at a frequency of 1 Hz and heating rate of 2 °C/min ramping from 25 °C to 200 °C and analyzed by Universal Analysis 2000 software. Sample specimens were cured according to specific thermal profiles with dimensions approximately 1 mm thick and 5 mm wide.

Differential scanning calorimetry was performed using a DSC Q2000 from TA Instruments, Inc. Approximately 7.5 mg was weighed into aluminum DSC pans, sealed, cured according to specific thermal profiles, heated at 10 °C/min and cooled at 5 °C/min through the temperature range of 25 °C to 200 °C, and analyzed by Universal Analysis 2000 software.

Spectroscopy

Near infrared spectroscopy in transmission mode was conducted on a Thermo Nicolet 6700 using a CaF₂ beamsplitter, wavenumber range of 4000 cm⁻¹ to 8000 cm⁻¹, thermo heat cell attachment, B screen filters, an aperture of 15 – 20, and sample thickness of 0.5 mm using Teflon[®] spacers. Spectra were collected every 5 min and composed of 32 scans at a resolution of 4 wavenumbers (cm⁻¹). The experiment began with the sample mixed as previously described and loaded into the heat cell. The heat cell temperature was at ambient for 15 hours then ramped to 60 °C at 15 °C/min under purging nitrogen gas. The sample was held at 60 °C for 75 min then heated to 120 °C at 15 °C/min and held for 195 min. Spectra were processed using Omnic software automatic baseline corrections. Molar absorptivities of monomers were measured by collecting spectra at ambient temperature, 60 °C, and 120 °C.

Microscopy

Visual light microscopy experiments were performed on Keyence VHS 600 microscope at 50 x magnification. The AFM images were collected using a Bruker Dimension Icon operating in tapping mode with Bruker RTESP probes (0.01 - 0.025 Ωcm Antimony (n) doped silicon probe, spring constant: 20-80 N/m). Scanning electron microscopy images were collected using a Zeiss Sigma Variable Pressure, Field Emission Gun Scanning Electron Microscope (VP-FEG-SEM) with Thermo energy dispersive and wavelength dispersive X-ray detectors (EDS/WDS) at an accelerating voltage of 10 kV. Samples used for SEM analysis were sputter coated with silver at an instrument reported thickness of 5 nm. For fracture analysis, the samples were scored and fractured rapidly with a hammer driven razor blade. The fractured samples were then mounted and scanned by SEM and AFM.

Results and Discussion

Chemorheology

Near infrared spectroscopy enables quantitative analysis of the epoxy-amine reaction through detection of the epoxide, primary amine, and secondary amine functional groups. Specific peaks of interest were the epoxide overtone at 4530 cm^{-1} , primary amine overtone at 4940 cm^{-1} , and primary/secondary amine overlap overtone at 6500 cm^{-1} .³ Since the primary amine was completely consumed during the second post-cure, the secondary amine molar absorptivity could be calculated since its non-linear contribution to peak area at the primary/secondary amine overlap overtone at 6500 cm^{-1} had ceased. The simultaneous calculation of epoxy, primary amine, secondary amine, and even tertiary amine concentrations has been reported.^{3,14,15} However, analyzing this system by these methods resulted in inconsistent concentrations of secondary amine. For

simplicity, only the epoxy and primary amine concentrations were considered for the first stage of the reaction until the primary amine peak was eliminated during the second post-cure stage. The NIR spectroscopy of the DGEBA / 2-methyl-1,5-diaminopentane reaction revealed complete conversion of the epoxide functional group within 25 min at the 120 °C post-cure stage. Decreases in the secondary amine functional group were observed to continue for an additional hour after the epoxy peak was no longer detectable (Figure 92).

Table 21 summarizes the molar absorptivities of the epoxide, primary amine, and secondary amine. The molar absorptivity of the secondary amine was twice as large in magnitude as that of the epoxide. The increased absorption sensitivity of the secondary amine overtone allowed for smaller concentrations of the secondary amine to be detected than the epoxide. In the last 120 °C post-cure stage, the NIR results showed subtle (< 1%) changes in the secondary amine at > 99% conversion of the amine hydrogens while the epoxy peak was non-detectable.

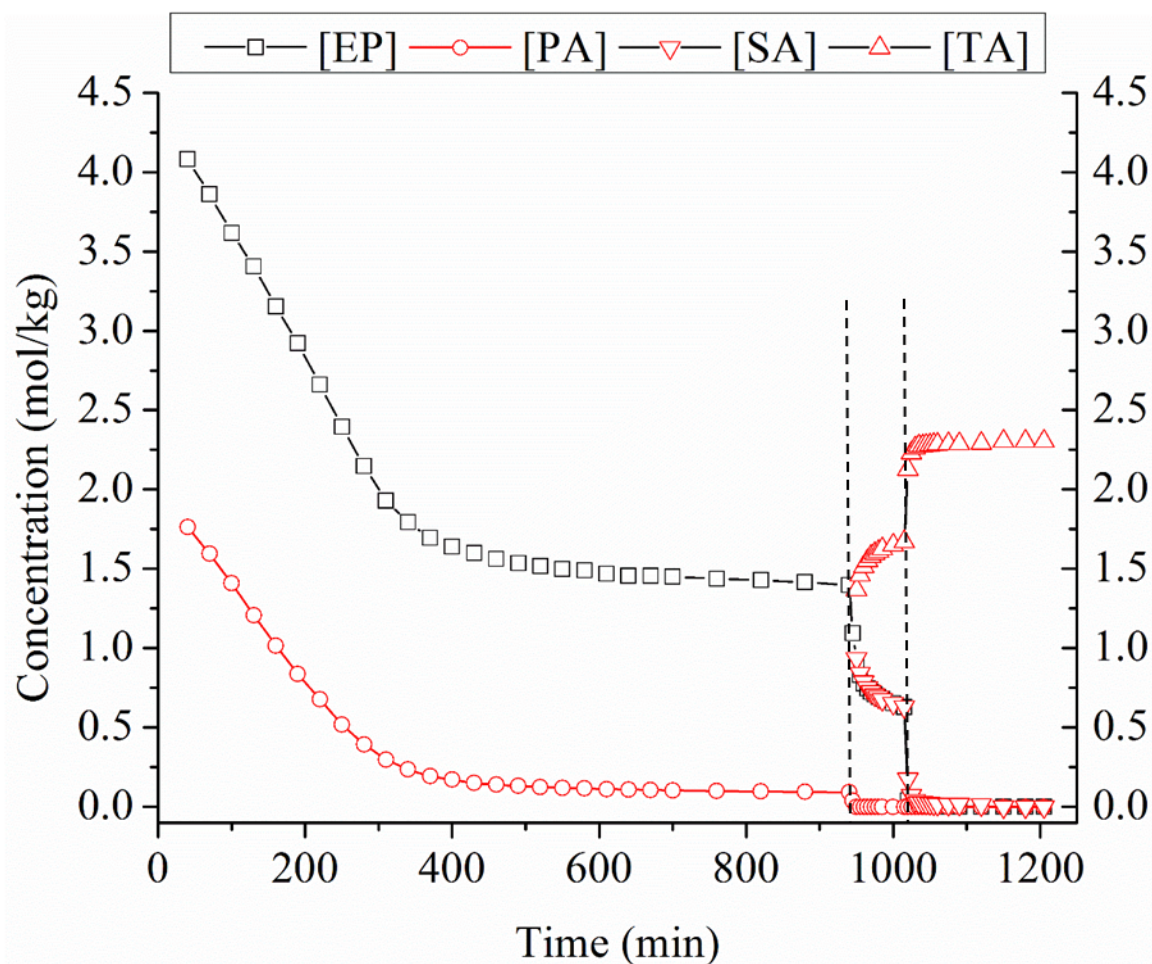


Figure 92. Functional group concentrations measured by transmission NIR of the DGEBA - 2-methyl-1,5-diaminopentane epoxy-amine reaction. EP is concentration of epoxy functional group, PA is concentration of primary amine, SA is concentration of secondary amine and TA is the calculated concentration of tertiary amine. The dashed vertical lines separate the cure profile temperature zones; ambient for 15 hours, 60 °C for 75 min., and 120 °C for 195 min.

Table 21

Molar Absorptivities

Functional Group (NIR Peak)	Molar Absorptivity ($A \cdot \text{kg} \cdot \text{mol}^{-1} \cdot \text{cm}^{-1}$) ^a
Epoxide (4530 cm^{-1})	4.15
Primary Amine (4940 cm^{-1})	5.98
Secondary Amine (6500 cm^{-1}) ^b	8.42

^a The A unit in molar absorptivity is peak area.

^b Molar absorptivity of the secondary amine was not calculated from the monomer, but after complete consumption of the primary amine during the reaction. Since relatively low temperatures were used, quantitative conversion was assumed to have taken place between epoxy and amine functional groups.

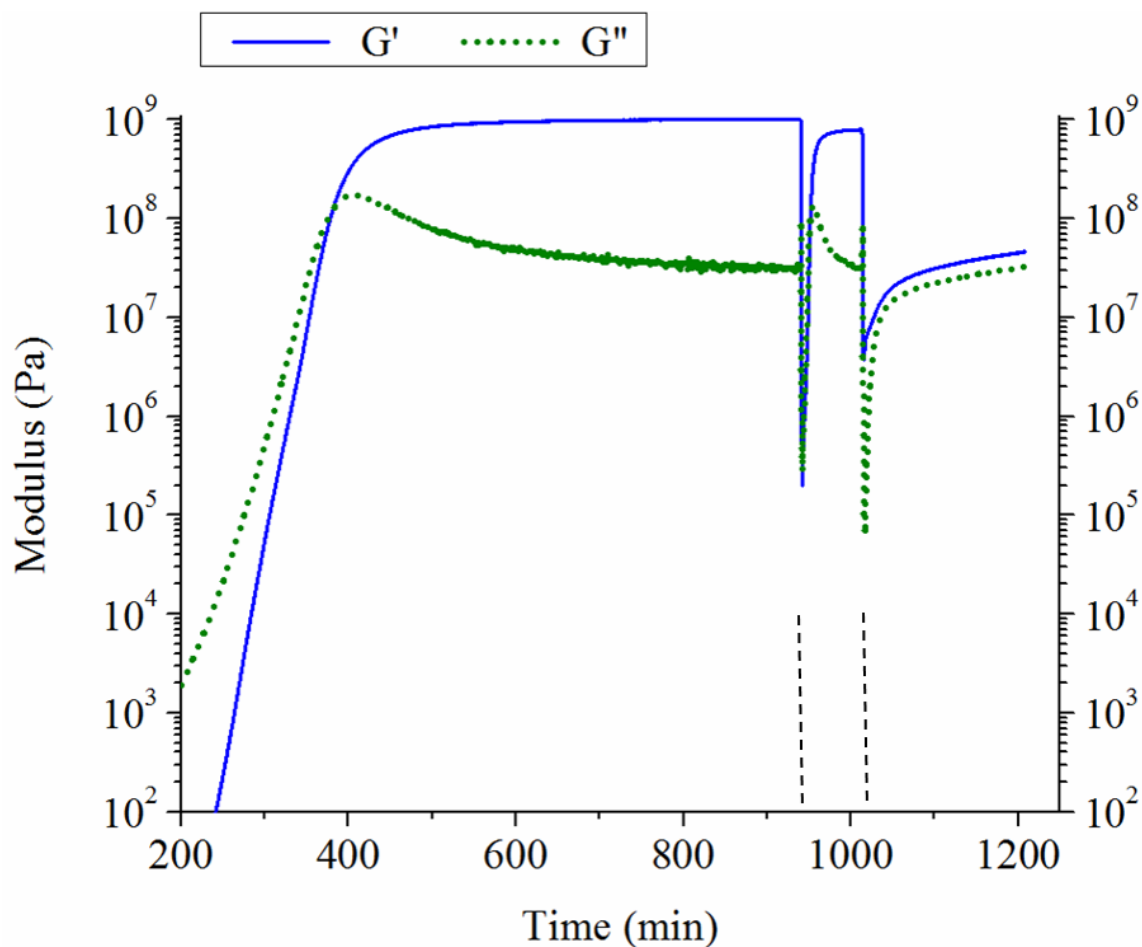


Figure 93. Rheology profile of DGEBA - 2 methyl-1,5-diaminopentane epoxy-amine reaction. The dashed vertical lines separate the temperature zones; ambient for 15 hours, 60 °C for 75 min., and 120 °C for 195 min.

The gel point occurred at approximately 390 minutes as indicated by the G'/G'' crossover during the ambient temperature stage (Figure 93). The material quickly vitrified transitioning to the glassy state before post-cure stages at 60 °C and 120 °C. The storage modulus continued to increase during the 120 °C post-cure stage. NIR confirmed within detection limits the reaction cessation, thus, the modulus increase was most likely a physical change within the material and not due to a chemical process. The mechanical T_g of the material, taken as the $\tan \delta$ peak, was 122 °C, which indicates that the material may be physically aging while glassy domains may still exist in the material during the

holding period at 120 °C (Figure 93). An opposing possibility to the observed increase in modulus is that these results indicate a chemical change, and, as a result, the mechanical T_g has retarded the epoxy-amine reaction preventing full conversion of the material during the 120 °C post-cure stage of the rheology experiment. NIR spectroscopy indicated complete conversion during the 120 °C post-cure stage, and no significant differences in mechanical properties were observed between samples cured according to γ and δ thermal cure profiles.

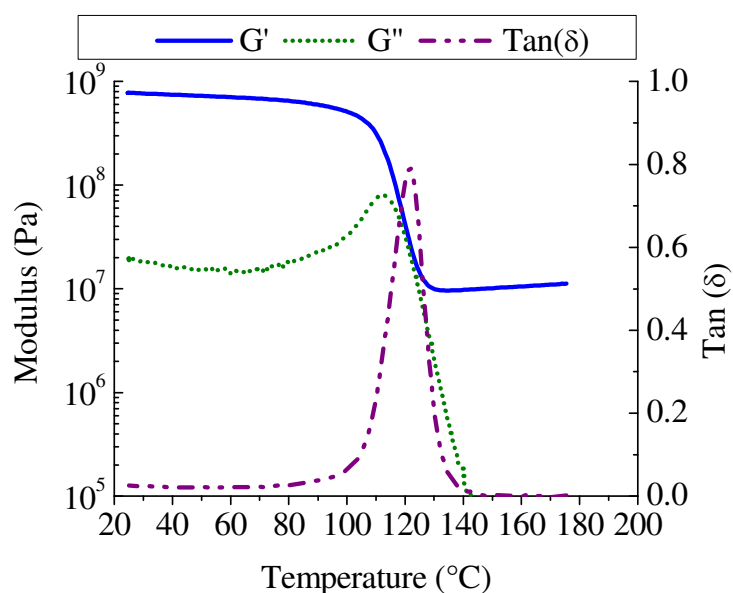


Figure 94. Dynamic rheology thermal sweep from high temperature to low temperature of the same experiment as Figure 93.

After the material was held at 120 °C for 195 min. (Figure 93), the sample was heated to 176 °C and cooled to 25 °C at a rate of 2 °C/min (Figure 94). Transition from the rubbery plateau to the glass resulted in an accurate measurement absence of any thermal historical effects that would artificially alter the T_g . Exposing the sample to high temperatures for extended time results in complete cure with a final T_g of 122 °C as indicated by the peak $\tan \delta$ (Figure 94).

The NIR experiments measured the epoxy functional group conversion at the various stages of cure (Table 22). Although DMA is a more sensitive technique than DSC for T_g measurement, the relaxation times of polymers in response to deformation frequency yield T_g values higher than that obtained from purely thermal techniques. In Table 22, midpoint analysis of the inflection in DSC heat flow curves indicated a T_g value slightly less than 120 °C.

DMA data in Figures 95 and 96 indicate subtle shifts in T_g between the γ and δ cure profiles. Although the rubbery plateau moduli for the two cure conditions overlay very well, the onset storage modulus and peak $\tan \delta$ was shifted by 2-3 °C for the extended cure profile δ . These changes in T_g response of the cure profiles represent slight increases in conversion that are non-detectable from NIR spectroscopic techniques. Peak $\tan \delta$ values for δ and NV cure profiles in Table 22 match the peak $\tan \delta$ of the rheology experiment in Figure 94 confirming with reasonable certainty full cure for δ and NV thermal profiles.

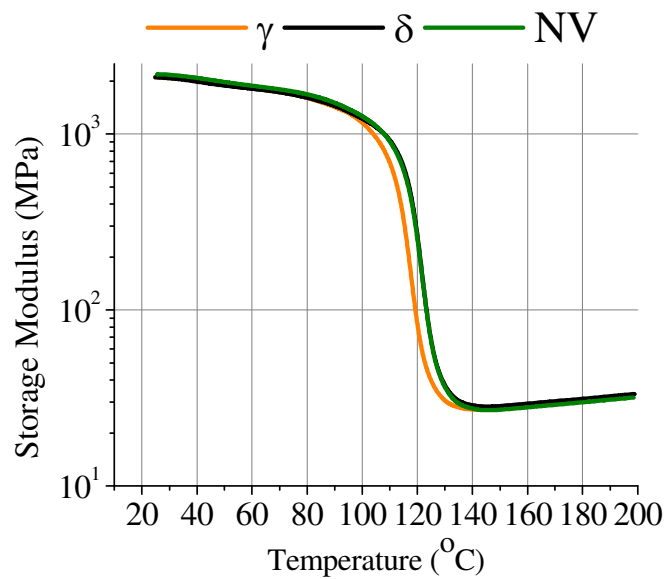


Figure 95. Storage modulus versus temperature of various cure profiles.

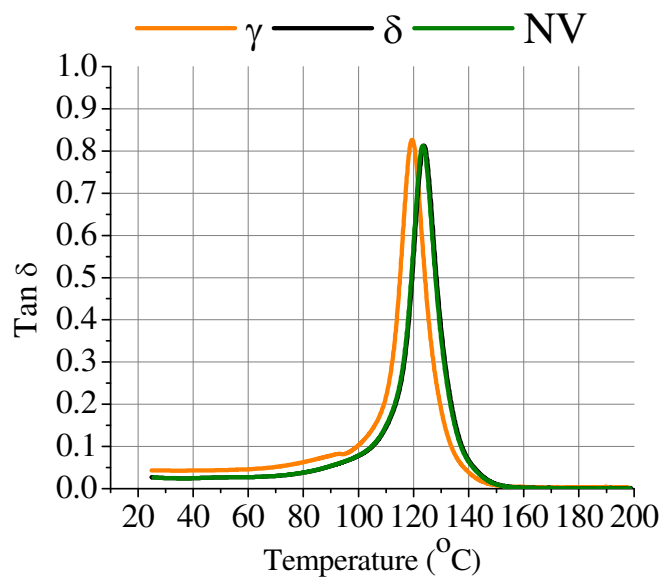


Figure 96. Tan δ versus temperature of various cure profiles.

Table 22

NIR Epoxide Conversion with Thermal Cure Profiles and Measured T_g

Thermal Cure	Conversion ^a	T_g (°C) ^b	$G' - T_g$ (°C) ^c	Tan $\delta - T_g$ (°C) ^d
α	0.69	48.1 ^e	---	---
β	0.86	83.9 ^e	---	---
γ	0.99 ^f	114.5±0.7	110.8±0.7	120.0±0.6
δ	0.99 ^f	119.4±0.8	114.0±0.5	122.6±0.8
NV	0.99 ^g	116.2±1.4	114.1±0.1	123.4±0.1

^a Epoxide conversion measured using the peak area of the epoxide NIR overtone at 4530 cm⁻¹ in combination with molar absorptivities reported in Table one. ^b Glass transition temperature determined by DSC heat flow midpoint analysis. ^c Glass transition temperature measured by DMA storage modulus onset. ^d Glass transition temperature measured by DMA peak tan δ . ^e T_g calculated through previously published T_g conversion relationships for DGEBA and 2-methyl-1.5-diaminopentane.^{16,17} ^f The epoxide overtone peak at 4530 cm⁻¹ is non-detectable, thus conversion is assigned to be greater than 0.99. ^g Based on NIR conversion values of γ/δ thermal profiles and glass transition temperatures, conversion is reasonably assumed to be greater than 0.99.

The weight fraction of monomer species can be calculated using equations developed by Flory.^{18,19} These equations were originally developed for step-growth condensation polymerizations and assume equal reactivity of functional groups. This assumption is not completely valid as there are potential reactivity differences between the primary and secondary amines. This is demonstrated in that Flory's model (Equation 13) predicts elimination of finite species at conversion values exceeding 0.7 as shown in Figure 97. However, from the NIR data in Figure 92 and Table 22, primary amine was still detected at conversion values greater than 0.7. This potentially indicates that the

secondary amine reaction between an epoxide group is faster than that of the primary amine.

In Equation 13, ρ is defined as the ratio of non-branched units to the total units of the mixture. N_a is the mol of branched monomer and its functionality f_a . N_b is the mol of non-branched monomer and its functionality f_b .

$$\rho = \frac{N_b f_b}{N_a f_a + N_b f_b}$$

Equation 13. Ratio (ρ) of non-branched units to the total units of the reaction mixture.

If $r=1$ and the conversion of $p_a=p_b=p$, then the critical branching coefficient α is given in Equation 14. Here, it is assumed that the conversion of epoxide is equal to the conversion of amine hydrogens, N-H.

$$\alpha = \frac{p^2 \rho}{1 - p^2(1 - \rho)}$$

Equation 14. The critical branching coefficient α as a function of conversion (p) and the ratio of non-branched units to the total units of the mixture (ρ).

The weight fraction of finite species, w_x , is given in Equation 15. The variable x is the degree of polymerization and f is the functionality of the branching species 2-methyl-1,5-diaminopentane, which is equal to 4.

$$w_x = \left[\frac{(fx - x)! f}{(x - 1)! (fx - 2x + 2)!} \right] \alpha^{x-1} (1 - \alpha)^{fx - 2x + 2}$$

Equation 15. Weight fraction of finite species.

The consumption of finite species in Figure 97 at conversion values equal or exceeding 0.7 correlates well to the vitrification of the epoxy-amine thermoset in Figure 93 and the NIR calculated conversion of 0.69 from Table 22.

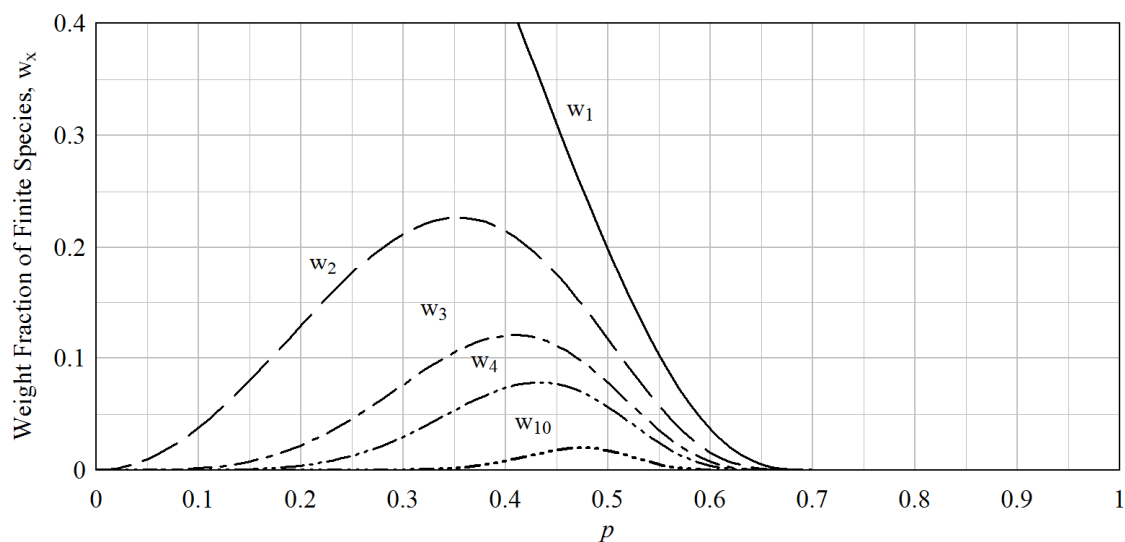


Figure 97. Weight fraction of finite species calculated using Flory's statistical equations.¹⁸⁻²⁰

Morphology

Atomic force microscopy was used to probe fracture surfaces of DGEBA - 2 methyl-1,5-diaminopentane throughout conversion to full cure. Observations revealed nodule morphology similar to that reported by other authors.⁶⁻⁹ Sahagun and Morgan showed that these structures began to develop at the rheological gel point until vitrification of the material.⁴ Since the monomers used in this current study are liquid at room temperature, the epoxy-amine reaction continues until vitrification at ambient temperature preventing pre-vitrification measurement. Fracture surfaces were imaged corresponding to the various thermal cure profiles in Figures 98 and 99.

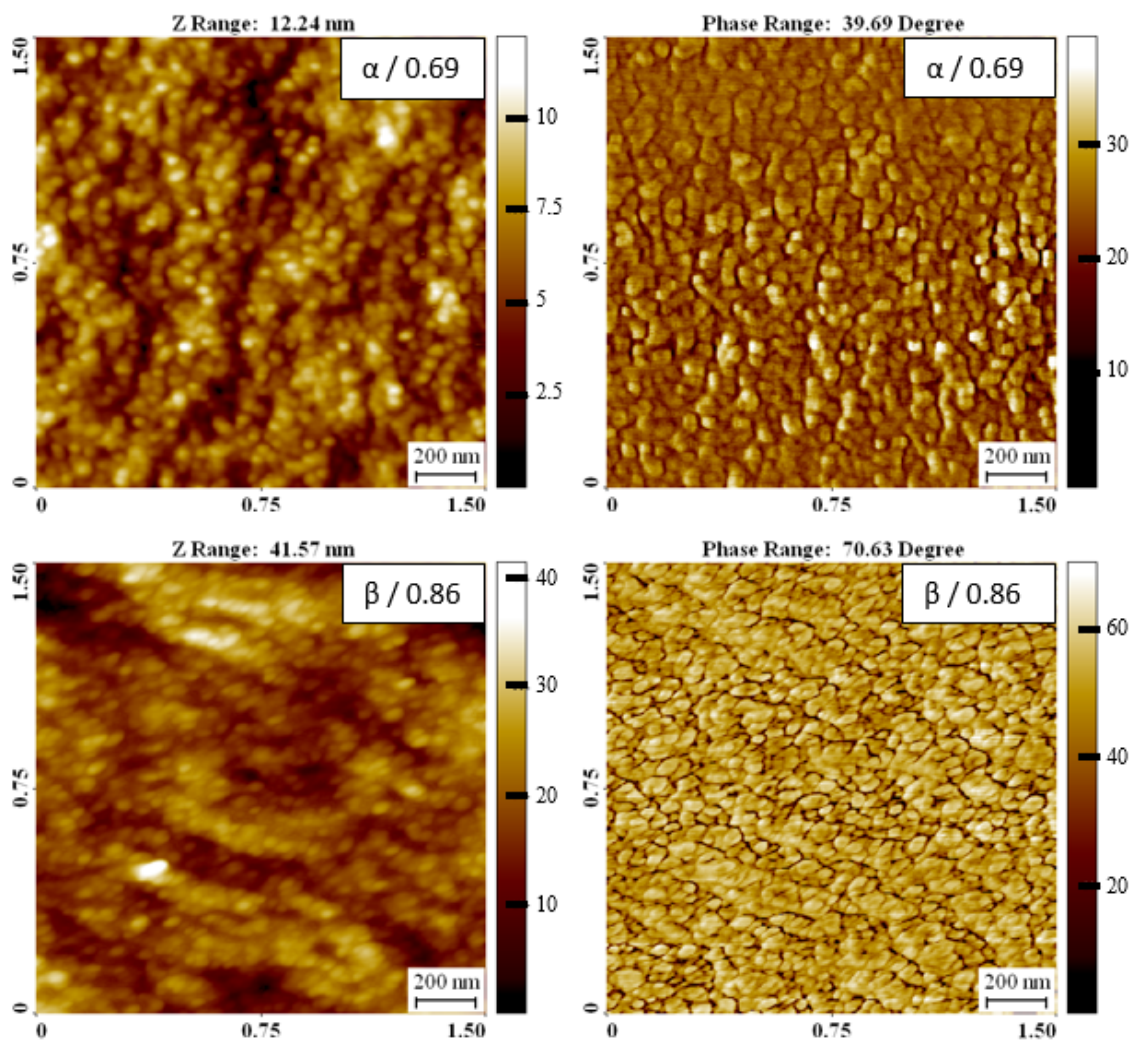


Figure 98. AFM images of DGEBA - 2 methyl-1,5-diaminopentane resulting from cure profiles α and β with conversion values listed. Images in the left column are height images whereas the images in the right column are phase images.

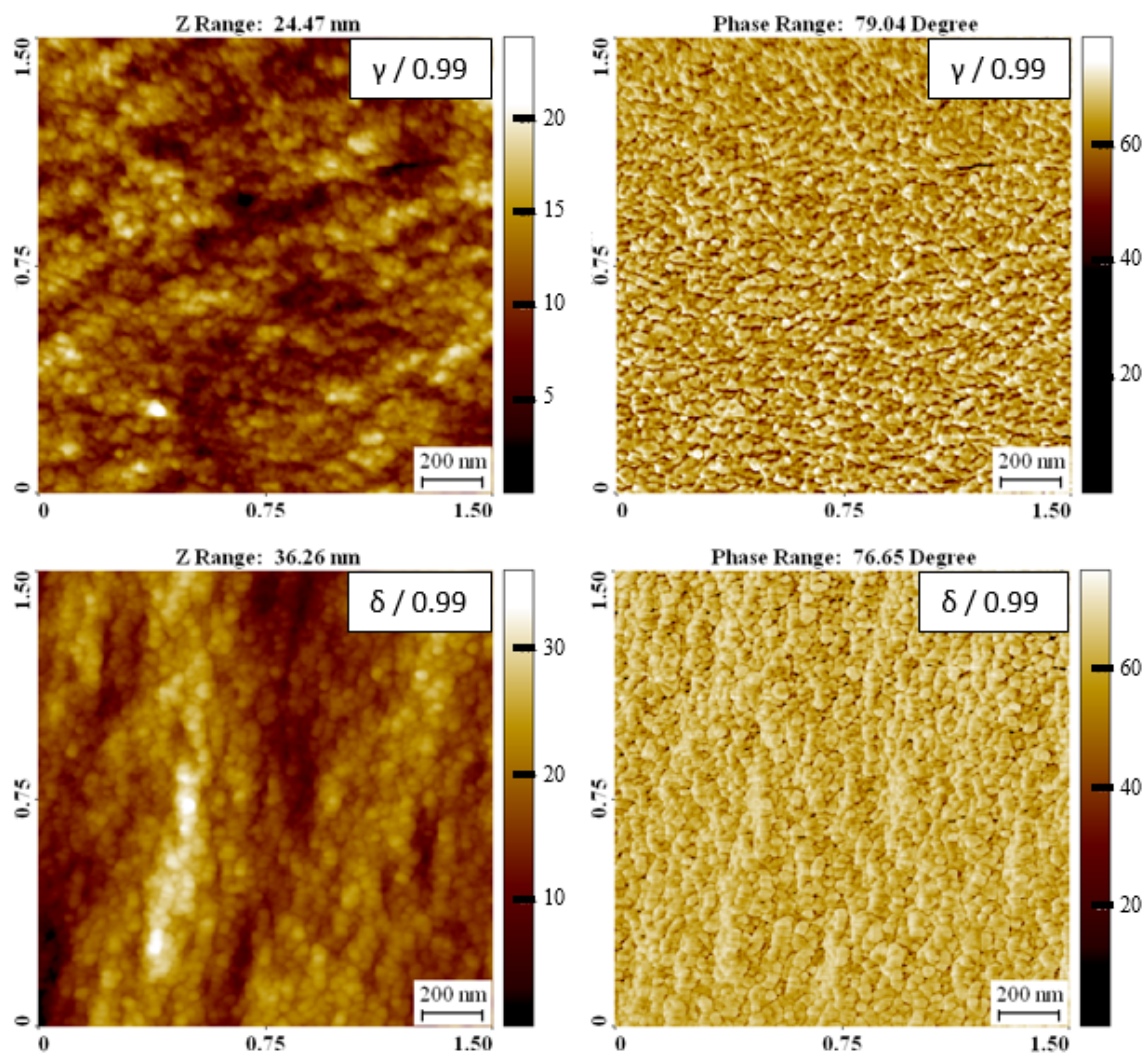


Figure 99. AFM images of DGEBA - 2 methyl-1,5-diaminopentane resulting from cure profiles γ and δ with conversion values listed. Images in the left column are height images whereas the images in the right column are phase images.

Fracture surface morphology showed consistent structure sizes independent of post-vitrification conversion. The consistent structure size was most evident within the height imaging of the α/β cure profiles versus the γ/δ cure profiles as shown in Figures 98 and 99. The AFM phase imaging results correlated well with SEM images in Figures 100 and 101. The phase image of the α cure profile closely matched the corresponding α SEM image in Figure 100.

The SEM images of the polymer fracture surfaces are shown in Figures 100 and 101 as a function of cure profile. The size domains of the microstructure morphology, measured through AFM and SEM, were determined to be in the 50 nm range. The SEM images indicate little, if any, difference in shape and size upon comparing α/β thermal cures versus those of γ/δ . Once the morphology was formed, additional increases in the extent of the reaction exerted minimal effect on the size and shape. These results are in agreement with the findings of Sahagun and Morgan from the AFM fracture surface images of a DGEBA and 3'-3' diaminodiphenyl sulfone system prior to the gel point and through post-vitrification.⁴ The correlation of both AFM and SEM images indicate the existence and separation between the nodule morphology. This strongly supports the existence of nodules as opposed to results of imaging artifacts reported by Haba.¹² The post-vitrification morphology size and structure are constant with increasing conversion. Therefore, changes in mechanical properties must be due to traditional explanations of changing intermolecular forces.²

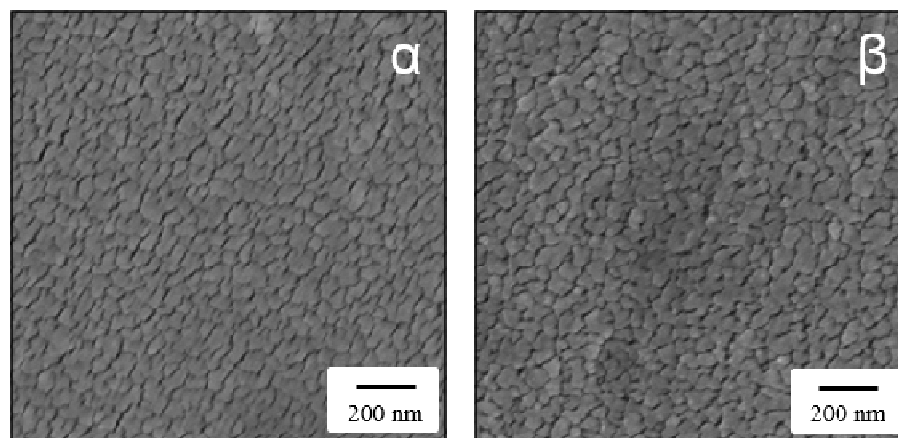


Figure 100. SEM images of DGEBA / 2 methyl-1,5-diaminopentane resulting from cure profiles α and β .

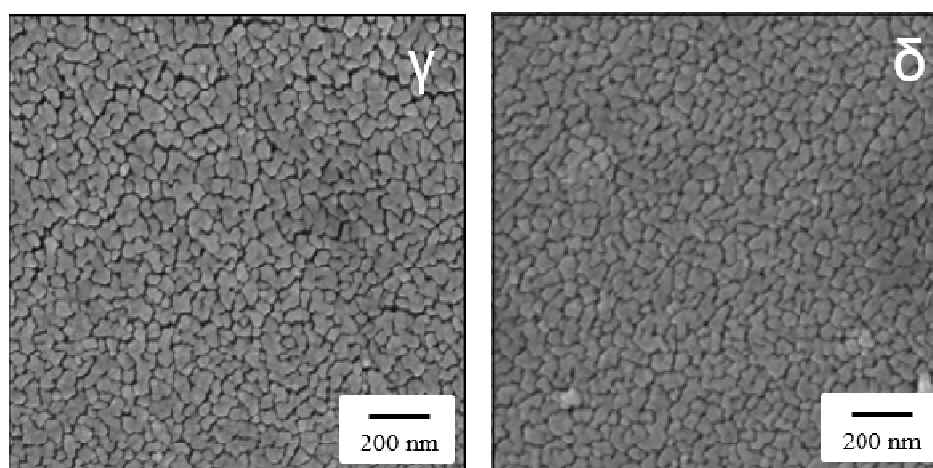


Figure 101. SEM images of DGEBA / 2 methyl-1,5-diaminopentane resulting from cure profiles γ and δ .

Mechanical Testing

Stress-strain curves (Figure 102) indicate distinctive mechanical differences between the various thermal cure profiles of DGEBA - 2 methyl-1,5-diaminopentane. Thermal profile α generated brittle samples that could not be secured in the MTS fixtures for analysis. Samples subject to full conversion in cure profiles γ/δ exhibited loss of mechanical properties and supports previously observed results by Marks.² Increase in

conversion from 0.86 for β to > 0.99 for γ/δ resulted in $\sim 25\%$ decrease in modulus (Table 23). Thermal cure profiles γ/δ had minimal mechanical differences, which indicate minimal differences in degree of conversion.

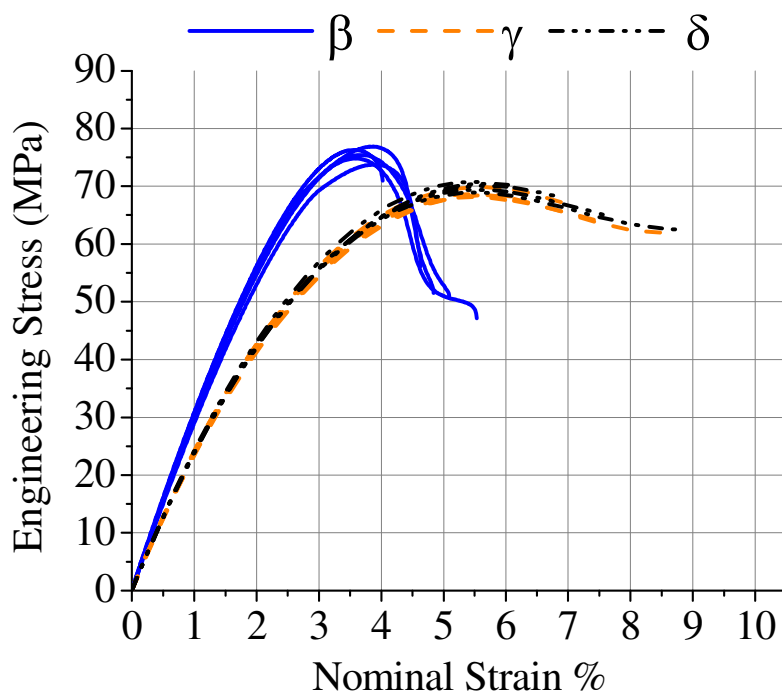


Figure 102. Tensile stress-strain curves of DGEBA - 2 methyl-1,5-diaminopentane at various stages of cure. For each cure profile, $n = 5$.

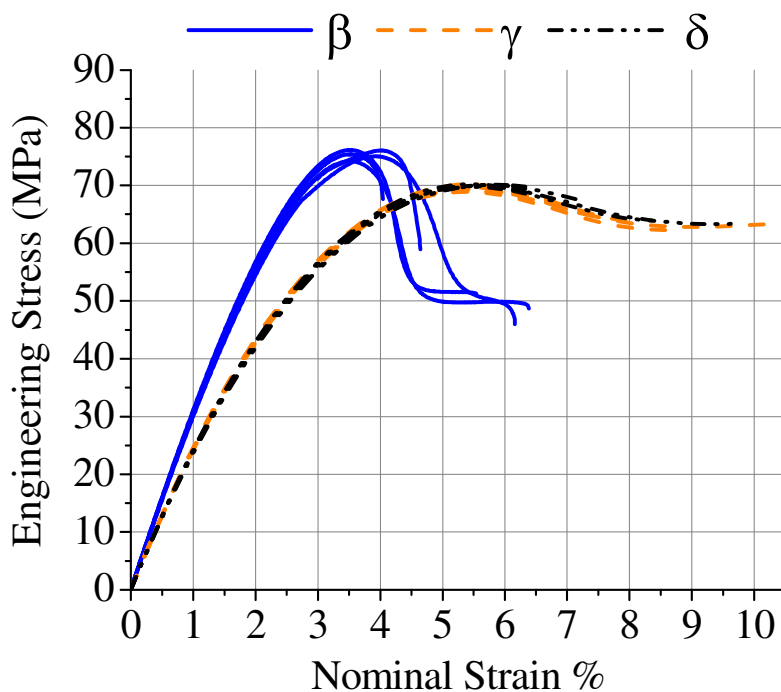


Figure 103. Tensile stress-strain curves of DGEBA - 2 methyl-1,5-diaminopentane at various stages of cure. Samples were sputter-coated for digital imaging. For each cure profile, $n = 5$.

In Figures 102 and 103, the stress-strain curves revealed atypical yield behavior in tension testing for the epoxy-amine thermoset. Odegard and Bandyopadhyay stated that fully cured glassy epoxy thermosets lacked the ability to yield in monotonic tension testing.²¹ Researchers have noted this atypical behavior without explanation reporting yield in tension at testing temperatures within 20 °C below the T_g ,^{13,22,23} incomplete cure of the epoxy-amine thermoset,²⁴ and reduced strain rates outside of the recommended time of failure in ASTM D-638-10.²⁴ To specifically counter the known causes for yield in tension, mechanical testing was conducted at 80 °C below the T_g . NIR analysis of this sample indicated full cure, no solvents were used in synthesis of the thermosets, and at a crosshead speed of 0.75 mm/min, the time-to-failure for all type V samples were within the recommended 0.5 - 5 min timeframe recommended by ASTM D-638-10.

The digital strain map of the Aramis system reveals localized strain in excess of 30% (Figure 104). The sample imaged in Figure 104 was the sample exhibiting strain hardening behavior at nominal strains above 10% in Figure 103. Digital image correlation experiments were used to resolve fracture formation with respect to the strain map tensile deformation. Smooth mirror surface fracture formations resulted at localized strains higher than 25%. Fractures in regions at lower strains resulted in mirror-mist-hackle topographies. These data further support the hypothesis for alignment of structure through plastic flow and strain deformation to be necessary for smooth fracture to occur through the specimen.

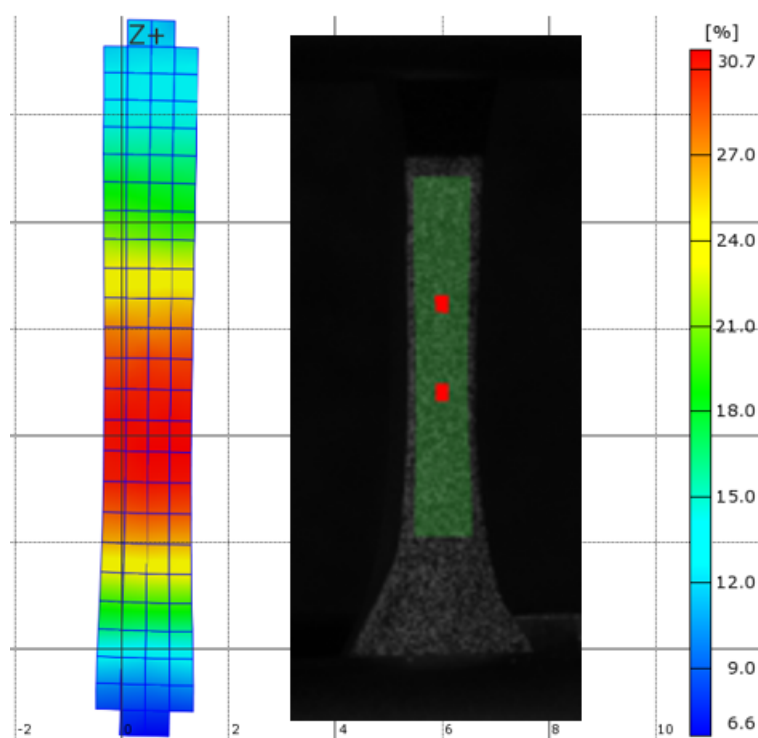


Figure 104. Strain map of sample surface calculated through digital image correlation. Inset photograph shows mounted sample with green highlights indicating the strain map zone, red squares indicating starting regions for facet field generation.

Fracture toughness data paralleled with Young's modulus trends (Table 23). K_{IC} decreased by more than 50% as the material approached > 0.99 conversion. No

significant mechanical differences were observed between the γ/δ cure profiles further indicating minimal or no increased conversion at extended times above T_g . Young's modulus decreased by approximately 25% as conversion increased from 0.86 to > 0.99 (Table 23). The decrease in Young's modulus with conversion agreed with reported epoxy-amine thermoset data.² The average Poisson's ratio was shown to increase with conversion. However, reproducibility was insufficient for firm conclusions to be made.

Table 23

Thermal Cure Profiles and Mechanical Properties

Conversion ^a	K_{IC} (MPa m ^{0.5})	LVDT Modulus (GPa) ^b	Modulus (GPa) ^c	Poisson's ratio
β - 0.86	2.14 ± 0.14	3.15 ± 0.05	3.82 ± 0.11	0.367 ± 0.014
γ - 0.99	1.04 ± 0.08	2.56 ± 0.04	2.98 ± 0.32	0.375 ± 0.002
δ - 0.99	1.05 ± 0.06	2.58 ± 0.02	2.79 ± 0.22	0.382 ± 0.021

^a Cure profile α samples were too brittle to load in mechanical test fixtures. ^b Linear variable displacement transducer (LVDT) modulus determined from slope of nominal strain versus engineering stress. ^c Modulus calculated from bonded strain gauge data.

Microscopy

Reproducible and uncharacteristic tensile stress-strain behaviors of cured glassy epoxy-amine networks were observed to produce distinctive fracture surfaces. Test specimens exhibiting plastic flow resulted in mirror-like finishes whereas samples that failed during yield or strain softening regions possessed notably rough surfaces.²⁵ Mirror-like fracture surfaces were noted within samples experiencing nominal strain values above 7.5% in the plastic flow region (Figure 105). Fracture at nominal strain

values below 7.5% resulted in typical mirror-mist-hackle topography. These types of fracture surfaces and mechanical behavior were present in both thermal profiles γ/δ . Tensile fracture surfaces of the complete mirror zone in Figure 105 have not been reported as yet. Researchers who reported yield in tension testing of epoxy-amine thermosets did not report fracture surfaces of samples experiencing plastic flow.^{13,22-24} The samples experiencing plastic flow, like those imaged in Figure 105, were not observed to fail by necking through traditional ductile failure. The mirror fracture surfaces were flat and sample halves could be refitted with opposing halves.

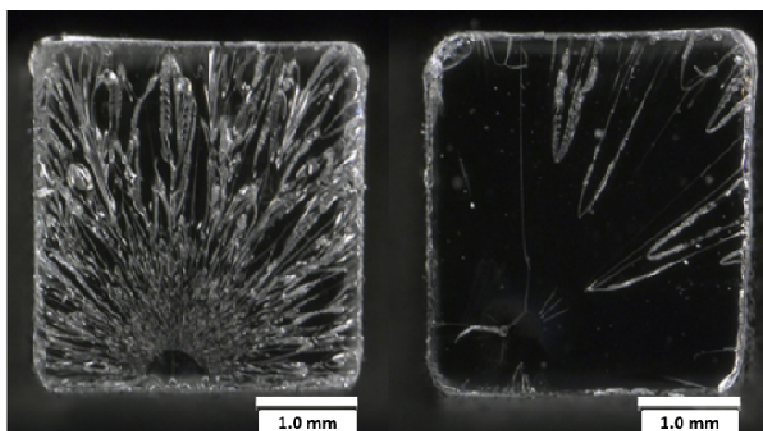


Figure 105. Microscopy images of pull-to-break fracture surfaces of Type V ASTM D-638 dogbone samples. Image on the left is typical mirror-mist-hackle fracture topography.²⁶ Image on the right is atypical mirror surfaces formed from samples experiencing plastic flow at nominal strains $> 7.5\%$.

Crack initiation begins in the mirror region and propagates outwards increasing in speed and roughness, and the increasing size of the mirror region correlates with increasing toughness.²⁶ In thermoplastic terms, plastic flow represents chain reorientation and flow in the direction of extension eventually leading to strain hardening.²⁷ On the other hand, a glassy crosslinked thermoset lacks chain mobility to flow and reorient itself. The plastic flow behavior in Figures 102 and 103 was definitive viscous movement. However, the question remains, what is the source of the viscous

behaviour? It is hypothesized that the differentiation between the two fracture topographies is a result of structure alignment with the strain direction allowing planar fracture to propagate through the sample without macroscopic deviation resulting in a complete mirror surface.

Controlling Morphology / Mechanical Properties through Thermal Cure Staging

The gel point as defined through rheology is a liquid transitioning into the solid state. The epoxy-amine reaction begins in the liquid state with small monomer molecules that react to form larger molecules eventually reaching infinite molecular weight, which is accompanied by transition from the liquid state to the solid state. Sahagun and Morgan used dynamic rheology combined with AFM to show that during epoxy-amine thermoset polymerization, nodule morphologies emerged at the gel point and continued evolving in shape and size until vitrification occurred.⁴

It is hypothesized that the heterogeneous structures originate from the disparity in sizes of molecules arising from step-growth chemistry. The polydisperse domains increase in size until the apparent T_g of the domain reaches that of the cure temperature initiating vitrification. This causes a glassy state phase separation to occur in which the larger domains become a glass while the smaller domains continue to react until their apparent T_g reaches cure temperature. This process is depicted in Figure 106. This glass phase separation is responsible for the formation of heterogeneous nodular structures seen in Figures 98 - 101.

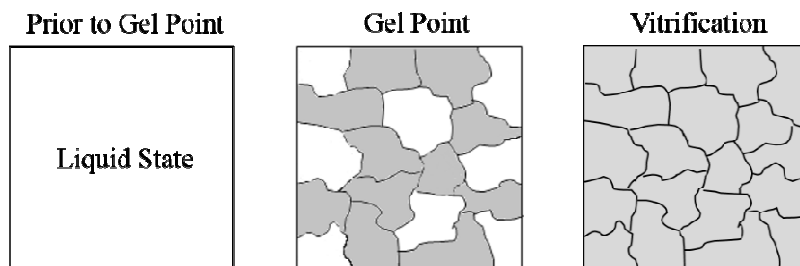


Figure 106. Depiction of isothermal phase transition from liquid state to vitrified glass for a step-growth thermoset. Areas colored white indicate liquid fraction and areas shaded grey indicate solid domains.

We further hypothesize that phase separation effects can be avoided by removing the vitrification event while epoxy-amine conversion is still taking place. We expect that the material will result in a more continuous morphology, which will eliminate the capacity for plastic flow behavior.

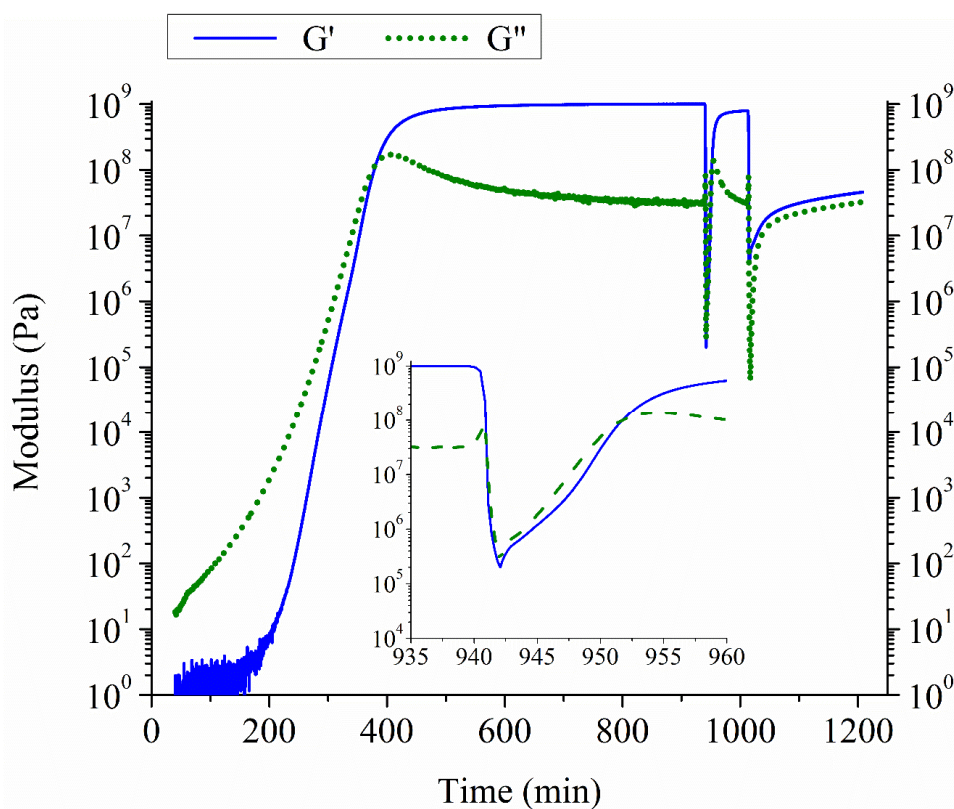


Figure 107. Rheology profile of the DGEBA - 2 methyl-1,5-diaminopentane epoxy-amine reaction. The inset graph details initial time points for 60 °C stage.

Using the rheological data from Figure 107, a thermal cure profile was designed to avoid vitrification, produce sufficient conversion at each thermal stage to prevent subsequent volatilization of the amine monomer, and produce full conversion of the epoxy-amine reaction. Staging the reaction using decreased times at ambient temperature and 60 °C avoids vitrification and keeps the physical state of the thermoset polymerization in either the liquid state or the rubbery state until full conversion is reached. The non-vitrification cure profile (NV) was selected to be 4 hours at ambient, 20 minutes at 60 °C, and 3 hours at 120 °C.

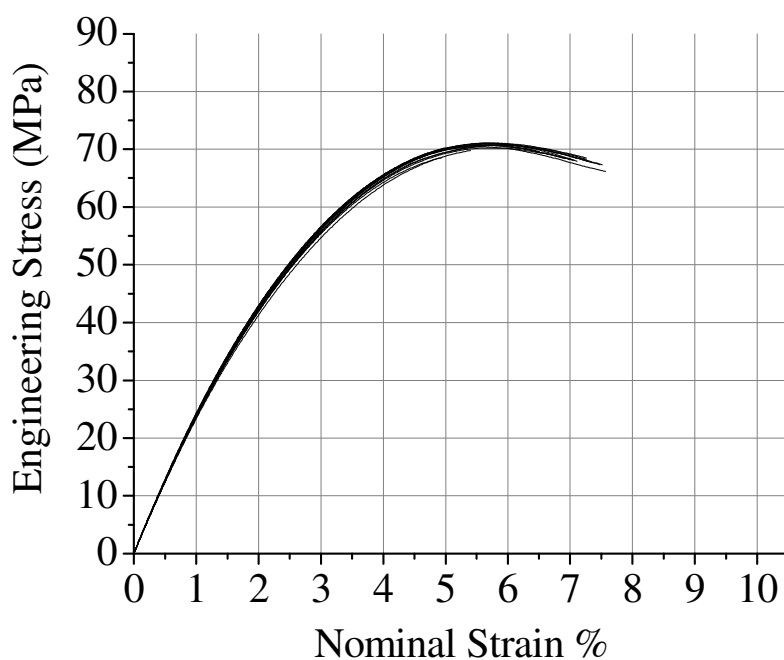


Figure 108. Tensile stress-strain curves of DGEBA - 2 methyl-1,5-diaminopentane with staged thermal cure (NV) to avoid vitrification during polymerization. For cure profile NV, $n = 14$.

Samples prepared with the modified thermal cure procedure were monitored gravimetrically to ensure that the amine did not volatilize during polymerization. Mechanical testing of 14 samples made with the modified cure procedure did not

demonstrate plastic flow behavior (Figure 108). All the specimens failed prior to 7.5% nominal strain and exhibited mirror-mist-hackle fracture topography patterns (Figure 105, left image). The LVDT modulus was determined to be 2.57 ± 0.03 GPa, which is identical to the LVDT modulus of γ/δ samples in Table 23. This observation is significant in that the morphology reported in Figure 109 impacts the strain-at-failure and not the initial elastic region or yield stress.

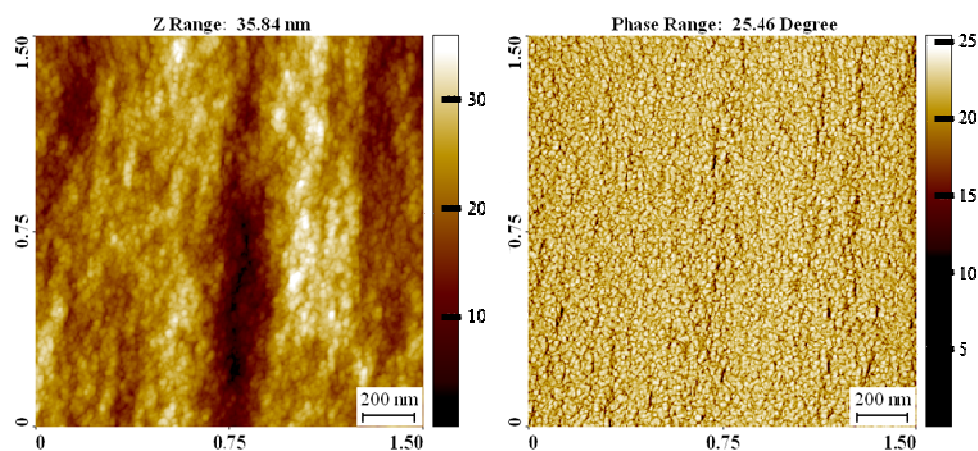


Figure 109. AFM images of DGEBA - 2 methyl-1,5-diaminopentane resulting from non-vitrification cure profile, left column (height image), right column (phase image).

In Figure 109, the non-vitrification cure profile did not completely eliminate the nodule morphology but resulted in greater amounts of a more continuous phase. The size domains of the nodules had decreased significantly, potentially promoting covalent connectivity between domains. The continuous morphology inhibited mobility as predicted and caused a reduction in propensity to yield for mechanical testing (Figure 108). Tuning morphology using thermal cure profiles has the potential to impart thermoplastic-like failure mechanisms within glassy thermosets without the loss of modulus, thermal stability, or chemical resistance.

Conclusions

This chapter has shown the various mechanical properties that an epoxy-amine thermoset can achieve at various stages of conversion. Although literature claims that glassy epoxy-amine thermosets do not yield in tension, this study showed that fully cured epoxies exhibited plastic flow and strain hardening during tensile testing. This unusual mechanical behavior for glassy thermosets also produced atypical complete mirror fracture surfaces for samples experiencing plastic flow. It is hypothesized that the plastic flow and fracture surfaces resulted from the deformation and alignment of structures within the thermoset.

Although nodule morphology in the 50 nm range can result from tip convolution artifacts, the existence of nodule morphology within epoxy-amine fracture surfaces was confirmed through two correlating techniques, AFM and SEM. Post-vitrification, the nodule morphology changes little in size and structure with increasing conversion. However, by removing the vitrification process during synthesis through thermal cure design, the nodule morphology can be reduced in size or eliminated, and the bulk mechanical properties of the material remain unchanged. However, the capacity of the material to yield in tension through plastic flow was eliminated.

It is hypothesized that the formation of heterogeneous structures originate from the disparity of network sizes arising from step-growth chemistry. The poly disperse domains increase in size until the apparent T_g of the larger domains reaches that of the cure temperature initiating vitrification. The vitrification of the large domains result in a glassy/liquid phase separation in which the larger domains become a glass while the smaller semi-liquid domains continue to react until their apparent T_g reaches cure

temperature and subsequently vitrify. This glass phase separation causes the formation of uniform modulus, but heterogeneous structures were observed via AFM and SEM. This understanding of morphology development in epoxy-amine conversion may indicate a way in which thermoplastic type failure mechanisms may be incorporated into glassy epoxy thermosets.

REFERENCES

1. D.W. Van Krevelen & K. Te Nijenhuis. *Properties of Polymers: Their correlation with chemical structure; Their numerical estimation and prediction from additive group contributions*. (Elsevier, 2009).
2. M.J. Marks & R.V. Snelgrove. Effect of Conversion on the Structure–Property Relationships of Amine-Cured Epoxy Thermosets. *ACS Applied Materials & Interfaces* **1**, 921-26, (2009).
3. M. Pramanik, E.W. Fowler & J.W. Rawlins. Another look at epoxy thermosets correlating structure with mechanical properties. *Polym. Eng. Sci.* **54**, 1990-2004, (2014).
4. C.M. Sahagun. *Molecular Network Development of a Thermosetting Epoxy-Amine Polymer*. The University of Southern Mississippi. (2012).
5. C.M. Sahagun & S.E. Morgan. Thermal Control of Nanostructure and Molecular Network Development in Epoxy-Amine Thermosets. *ACS Applied Materials & Interfaces* **4**, 564-72, (2012).
6. J.L. Racich & J.A. Koutsky. Nodular structure in epoxy resins. *J. Appl. Polym. Sci.* **20**, 2111-29, (1976).
7. J. Mijovic & J.A. Koutsky. Correlation between nodular morphology and fracture properties of cured epoxy resins. *Polymer* **20**, 1095-107, (1979).
8. R.J. Morgan & J.E. O'neal. The microscopic failure processes and their relation to the structure of amine-cured bisphenol-A-diglycidyl ether epoxies. *J. Mater. Sci.* **12**, 1966-80, (1977).
9. H. Kishi, T. Naitou, S. Matsuda, A. Murakami, Y. Muraji & Y. Nakagawa. Mechanical properties and inhomogeneous nanostructures of dicyandiamide-cured epoxy resins. *J. Polym. Sci., Part B: Polym. Phys.* **45**, 1425-34, (2007).
10. E.H. Erath & R.A. Spurr. Globular formations in thermosetting resins. *J. Polym. Sci.* **35**, 391-9, (1959).
11. K. Dusek. Are cured thermoset resins inhomogeneous? *Angew. Makromol. Chem.* **240**, 1-15, (1996).
12. D. Haba, J. Kaufmann, A.J. Brunner, K. Resch & C. Teichert. Observation of elastic modulus inhomogeneities in thermosetting epoxies using AFM – Discerning facts and artifacts. *Polymer* **55**, 4032-40, (2014).

13. M. Sharifi, C.W. Jang, C.F. Abrams & G.R. Palmese. Toughened epoxy polymers via rearrangement of network topology. *J. Mater. Chem. A* **2**, 16071-82, (2014).
14. E.W. Fowler, M. Pramanik & J.W. Rawlins. Near IR cure kinetics of a (DGEBA)-based epoxy prepolymer with various crosslinkers. *Int. SAMPE Tech. Conf.* **43**, Fowler1/1-Fowler1/14, 14 pp., (2011).
15. M. Pramanik, J.A. Scott, S.K. Mendon & J.W. Rawlins. Epoxy matrix architecture and connectivity characterization. *Int. SAMPE Tech. Conf.* **42**, a18/1-a18/19, (2010).
16. J. Pascault & R. Williams. Glass transition temperature versus conversion relationships for thermosetting polymers. *Journal of Polymer Science Part B: Polymer Physics* **28**, 85-95, (1990).
17. M. Pramanik, E.W. Fowler & J.W. Rawlins. Cure kinetics of several epoxy-amine systems at ambient and high temperatures. *J. Coat. Technol. Res.* **11**, 143-57, (2014).
18. P.J. Flory. Molecular size distribution in three-dimensional polymers. I. Gelation. *J. Am. Chem. Soc.* **63**, 3083-90, (1941).
19. P.J. Flory. Fundamental principles of condensation polymerization. *Chem. Rev.* **39**, 137-97, (1946).
20. G. Odian. *Principles of Polymerization*. (John Wiley and Sons, Inc., 2004).
21. G.M. Odegard & A. Bandyopadhyay. Physical aging of epoxy polymers and their composites. *J. Polym. Sci., Part B: Polym. Phys.* **49**, 1695-716, (2011).
22. T. Scherzer. Characterization of the molecular deformation behavior of glassy epoxy resins by rheo-optical FTIR spectroscopy. *J. Polym. Sci., Part B: Polym. Phys.* **34**, 459-70, (1996).
23. T. Scherzer. FTIR-rheo-optical characterization of the molecular orientation behavior of amine cured epoxy resins during cyclic deformation. *Polymer* **37**, 5807-16, (1996).
24. S.G. Miller, G.D. Roberts, J.L. Bail, L.W. Kohlman & W.K. Binienda. Effects of hydrothermal cycling on the chemical, thermal, and mechanical properties of 862/W epoxy resin. *High Performance Polymers*, (2012).
25. S.F. Foster, E.B. Williams & J.W. Rawlins. Influence of sub-T_g physical aging of a glassy epoxy thermoset on tensile plastic flow and fracture morphology in *ANTEC 2014 Technical Conference & Exhibition*. (April 28-30, 2014). Las Vegas, Nevada.

26. D. Hull. *Fractography: Observing, Measuring and Interpreting Fracture Surface Topography*. (Cambridge University Press, 1999).
27. Z. Bin Ahmad & M.F. Ashby. Failure-mechanism maps for engineering polymers. *J. Mater. Sci.* **23**, 2037-50, (1988).

CHAPTER VIII

SUMMARY

Overview

The overall goal of this research was to understand the molecular mechanisms of why thermoset polymers fail from mechanical fatigue. It was hypothesized that the degradation of mechanical performance and subsequent failure of glassy thermoset polymers originate from the accumulation of chain scission events. This dissertation presented research findings on this subject, focusing on detecting chain scission events through measuring nitroxyl radical populations with EPR spectroscopic analysis. The purpose of this chapter is to review the findings shared within this document and draw conclusions to guide future investigation of thermoset failure.

Summary of Results

The specific findings of this research were presented in the previous chapters with the goals to:

- 1) Successfully incorporate a nitroxyl radical probe molecule within an epoxy-amine thermoset and verify that the epoxy-amine reaction chemistry is not adversely affected by such incorporation
- 2) Subject nitroxyl radical loaded epoxy-amine thermosets to varying levels of fatigue and analyze the samples via EPR spectroscopy to detect loss of nitroxyl radicals and, therefore, chain scission events
- 3) Investigate through physical aging the relationship of plastic flow and mirror fracture surfaces occurring within a highly crosslinked glassy epoxy-amine thermoset

- 4) Understand the contributions to mechanical properties that nodule morphologies impart to glassy epoxy-amine networks

In Chapter III, we investigated the incorporation of nitroxyl radicals into the epoxy matrix. Compared to the control (no additive), variations in gel points and ultimate epoxy conversion were observed in systems containing blocked isocyanates based on *N*-methyl aniline and ϵ -caprolactam. However, no significant variation was detected with the 4-hydroxy TEMPO blocked isocyanate. The kinetic rate of the epoxy-amine reaction, measured by NIR decreased by $0.0015 \text{ mol} \cdot \text{kg}^{-1} \cdot \text{min}^{-1}$ for every 5 wt% of additive within the matrix.

Chemorheological techniques confirmed the chemical and mechanical compatibility of the epoxy-amine matrix system with blocked isocyanate additives and nitroxyl radicals. Reduction in kinetic rates of the ϵ -cap-b-IPDI and NMA-IPDI formulations are consistent with dilution effects from higher additive loadings. These formulations also exhibited a plasticization effect from the presence of small molecules that did not directly participate in network formation. The observed plasticization effects elicited higher levels of conversion (supported by both FT-NIR and rheological data) in systems containing NMA-IPDI and ϵ -cap-b-IPDI owing to postponement of vitrification. The system containing bis-TEMPO-IPDI did not display a statistically significant change in gelation time when compared to the control but did exhibit a reduction in kinetic rates in the isothermal regime studies. The consistent loss of reaction rates with increasing additive concentration suggests that the effect on kinetic rate is due to decreasing concentration of reacting functional groups and was not attributed to the presence of a competing mechanism.

In Chapter IV, nitroxyl radicals were incorporated into an epoxy matrix to detect mechanically produced homolytic chain scission events resulting from fatigue. The epoxy-amine matrix was subject to 30% UTS and 50% UTS fatigue studies with subsequent EPR and FTIR spectroscopic methods to detect changes in nitroxyl radical populations and epoxy-amine functional groups. Although mechanical property decreases and fatigue failure of specimens were observed in the 50% UTS study, decreases in nitroxyl populations relative to controls were not observed. This indicates that chain scission events were not detected. No changes in properties or functional groups within the epoxy-amine matrix were observed in the 30% UTS study. However, both control and fatigue conditions resulted in increases of nitroxyl radical population. This is attributed to the Denisov cycle significantly affecting nitroxyl populations within the 27 hour time frame of the study.

Non-detection of chain scission events can be attributed to several reasons. The viscosity of the glassy state is relatively high and can impede diffusion of the radical chain end to a BT-IPDI molecule. Also, it is unknown whether fatigue produces chain scission events prior to failure. Radicals are known to be capable of migration based on hydrogen abstraction. If radicals were known to be produced through mechanical destruction of the sample, it could then be determined experimentally if reactions could take place between the mechano-radicals and BT-IDPI within the glassy state. This would help elucidate if the physical barrier of the glassy state impedes both physical migration and chemical migration of mechano-radicals during strain.

In Chapter V, mechanically formed radicals were produced by grinding epoxy-amine thermosets. The characteristics of the mechano-radicals match what is reported in

literature. The Boltzmann statistics model was used to predict temperature dependent EPR signal decreases and distinguish between irreversible losses of radical population due to recombination versus reversible decreases in signal resulting from temperature changes. Modulated EPR was used to determine if reactions between nitroxyls and mechano-radicals occurred. The modulated experiment showed that mechano-radicals decrease in population due to recombination but did not detectably react with the nitroxyl radicals of BT-IPDI. Particle size analysis from light scattering revealed the deficit in potential population of surface broken bonds versus that of nitroxyl radicals in the bulk.

Future experiments could increase the potential for success through finer grinds to maximize the mechano-radical to nitroxyl ratio. In these experiments, it was assumed that the radical species is either a carbon-centered radical that, by itself or upon destabilization, forms products that can react with BT-IPDI similar to the Denisov cycle. It is possible that the liquid nitrogen possessed sufficient liquid oxygen to contaminate the radical products and create peroxy radicals, which cannot directly react with nitroxyl radicals. Ball milling under both high vacuum and liquid nitrogen temperatures would have to be performed with transfer to an EPR tube also under these conditions. The equipment to investigate this experimentally would involve cryo-grinding through specially manufactured equipment that is not commercially available as of yet.

In Chapter VI, reproducible and uncharacteristic tensile stress-strain behavior of cured glassy epoxy-amine networks were observed to produce distinctive fracture surfaces. Test specimens exhibiting plastic flow resulted in mirror-like finishes, whereas samples that failed during yield or strain softening regions possessed notably rough surfaces. We hypothesized that viscous deformation was required to form the atypical

complete mirrored fracture surfaces. By using physical aging as an investigative tool, we were able to eliminate the capacity of the epoxy-amine network for viscous deformation without adversely altering the polymer structure through chemical means. The elimination of plastic flow, resulted in the elimination of smooth fracture surfaces thus correlating the relationship between the atypical mechanical behavior and atypical fracture surfaces. The results indicate the potential existence of a structural feature capable of viscous deformation. AFM and SEM images revealed wormlike nodule type structures at the 50 nm size scale. It is hypothesized that these structures, as seen in Figures 90 and 91, are the underlying cause of the unusual mechanical yield behavior and atypical mirror fracture surfaces.

The research in Chapter VII showed the various mechanical properties that an epoxy-amine thermoset can achieve at various stages of conversion. Although literature claims that glassy epoxy-amine thermosets do not yield in tension, this study showed that fully cured epoxies exhibited plastic flow and strain hardening during tensile testing. This unusual mechanical behavior for glassy thermosets also produced atypical complete mirror fracture surfaces for samples experiencing plastic flow. It is hypothesized that the plastic flow and fracture surfaces resulted from the deformation and alignment of structures within the thermoset.

Although nodule morphology in the 50 nm range can result from tip convolution artifacts, it was confirmed through two correlating techniques, AFM and SEM, the existence of nodule morphology within epoxy-amine fracture surfaces. Post-vitrification, the nodule morphology changes little in size and structure with increasing conversion. However, by removing the vitrification process during synthesis through thermal cure

design, the nodule morphology can be reduced in size or eliminated. Although the bulk mechanical properties of the material remain unchanged, the capacity of the material to yield in tension through plastic flow was eliminated.

It is our hypothesis that the formation of heterogeneous structures originates from the disparity of network sizes arising from step-growth chemistry. The poly disperse domains increase in size until the apparent T_g of the larger domains reaches that of the cure temperature initiating vitrification. The vitrification of the large domains result in a glassy/liquid phase separation in which the larger domains become a glass while the smaller semi-liquid domains continue to react until their apparent T_g reaches cure temperature and subsequently vitrify. This glass phase separation causes the formation of uniform modulus but heterogeneous structures observed via AFM and SEM. This understanding of morphology development in epoxy-amine conversion may indicate a way in which thermoplastic type failure mechanisms may be incorporated into glassy epoxy thermosets. Future work will ascertain the degree of development and control of morphology through thermal staging.

Future Research Considerations

The work reported here in Chapters IV and V used a principal of measurement in which an existing population of radicals was monitored for slight decreases. This makes the confirmed detection more difficult in that it places a requirement of how many events must occur before confidence of a positive result is obtained. Using a large population of radicals would increase the ratio between nitroxyls and potential chain scission events favoring reaction probability but would eliminate the possibility of EPR detection as the small loss of signal would be outside the reproducibility of measurement.

Error is associated in this experimental technique due to the removal and replacement of the sample within the EPR cavity. At 9.8 GHz, a standing microwave possesses a wavelength of approximately 3.2 cm. This means that spatial placement of the sample to the exact point within the cavity is important for the magnitude of signal detected by the instrument. Since the fatigue treatment to the sample occurs outside of the cavity, spectra before and after treatment are taken, and placement back into the cavity for the second spectra will result in errors in signal of at least $\pm 7\%$.

Experimentally, it is easier to detect signal in the complete absence of overlapping or conflicting sources. Extremely low concentrations of radicals can be detected in fracture events, however, this case differs in that before the event, there was no EPR detectable source of radicals. Therefore, detecting signal where before there was none is more facile experimentally. Lengthy fatigue studies lasting for times in excess of 24 hours are complicated through the Denisov cycle affecting the population of radicals.

Future experiments could avoid these problems by developing a technology that incorporates a blocked nitroxyl radical within the elastic backbone of the thermoset (Figure 110). In this approach, the initial state of the epoxy-amine matrix would be absent of nitroxyl signals allowing fatigue cycles to be applied to the sample to detect if the nitroxyl radical forms from breakage of the N-O-R group. The breakage of this bond would form an unstable radical and a stable nitroxyl radical increasing the possibility of detection. This approach would seek detection of a positive signal in the absence of initial signal, a more facile experimental method than those mentioned previously. Although the N-O-R bond is relatively weak (32 kcal) compared to C-C bonds (80 kcal), this technique would allow for the first time detection of broken covalent bonds in glassy

polymers from fatigue. While this monomer unit would be relatively expensive, due to the sensitivity of EPR, very small concentrations would be needed. By incorporating only 1% of the repeat units as this structure, EPR detection limits used in these studies could positively detect 0.001% of the backbone structures forming nitroxyl radicals.

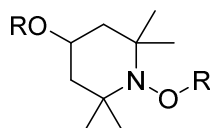


Figure 110. Elastically active nitroxyl probe created from 4-hydroxy-TEMPO.

In chapters VI and VII, unusual yield and fracture behavior of glassy epoxy-amine thermosets was reported. These observations were coupled with measurement of nodule morphologies through AFM and SEM. It was indicated that the formation of the nodules was due to phase separation through vitrification during polymerization. By removing the vitrification from synthesis, the size of the nodules was greatly reduced or even eliminated. This eliminated the capacity of plastic flow behavior and smooth fracture surfaces from tensile failure.

Future investigations should promote vitrification during cure as a potential toughening mechanism that does not detrimentally impact modulus. Several samples investigated within this study demonstrated strain hardening, an even more unusual behavior for glassy thermosets. It is unknown currently what the limiting strain-to-failure is for these types of systems, but performing tensile experiments with uniform cross-sectional shapes, such as square or circle patterns, that are polished to remove edge defects can explore the upper strain-to-failure boundary. This has the potential to increase the base toughness properties of thermoset materials before even toughening additives are incorporated. These thermoplastic type failure mechanisms coupled with

thermoset ease of processing, thermal properties, and chemical resistance would be advantageous to composite technology.

APPENDIX A

This Agreement between Stephen Foster ("You") and John Wiley and Sons ("John Wiley and Sons") consists of your license details and the terms and conditions provided by John Wiley and Sons and Copyright Clearance Center.

License Number	3493251009101
License date	Oct 20, 2014
Licensed Content Publisher	John Wiley and Sons
Licensed Content Publication	Polymer Engineering & Science
Licensed Content Title	An experimental study of uniaxial fatigue behavior of an epoxy resin by a new noncontact real-time strain measurement and control system
Licensed Content Author	Gang Tao,Zihui Xia
Licensed Content Date	Apr 30, 2007
Pages	9
Type of use	Dissertation/Thesis
Requestor type	University/Academic
Format	Print and electronic
Portion	Figure/table
Number of figures/tables	3
Original Wiley figure/table number(s)	Figure 6, Figure 8, Figure 11
Will you be translating?	No
Title of your thesis / dissertation	MECHANOCHEMICAL INVESTIGATION OF A GLASSY EPOXY-AMINE THERMOSET SUBJECTED TO FATIGUE
Expected completion date	Dec 2014
Expected size (number of pages)	200

APPENDIX B

This is a License Agreement between Stephen Foster ("You") and Springer ("Springer") provided by Copyright Clearance Center ("CCC"). The license consists of your order details, the terms and conditions provided by Springer, and the payment terms and conditions.

All payments must be made in full to CCC. For payment instructions, please see information listed at the bottom of this form.

License Number	3520400637411
License date	Dec 01, 2014
Licensed content publisher	Springer
Licensed content publication	Kolloid-Zeitschrift und Zeitschrift für Polymere
Licensed content title	ESR-Messung von Kettenbrüchen in mechanisch beanspruchtem Polyamid
Licensed content author	U. Johnsen
Licensed content date	Jan 1, 1973
Volume number	251
Issue number	11
Type of Use	Thesis/Dissertation
Portion	Figures
Author of this Springer article	No
Order reference number	None
Original figure numbers	Figure "Concentration of free radicals and uniaxial stress in step-temperature test as a function of temperature and time for polycaprolactam fibers "
Title of your thesis / dissertation	MECHANOCHEMICAL INVESTIGATION OF A GLASSY EPOXY-AMINE THERMOSET SUBJECTED TO FATIGUE
Expected completion date	Dec 2014
Estimated size(pages)	200

APPENDIX C

This Agreement between Stephen Foster ("You") and John Wiley and Sons ("John Wiley and Sons") consists of your license details and the terms and conditions provided by John Wiley and Sons and Copyright Clearance Center.

License Number	3493260844780
License date	Oct 20, 2014
Licensed Content Publisher	John Wiley and Sons
Licensed Content Publication	Journal of Applied Polymer Science
Licensed Content Title	The estimation of mechanical properties of polymers from molecular structure
Licensed Content Author	J. T. Seitz
Licensed Content Date	Mar 10, 2003
Pages	21
Type of use	Dissertation/Thesis
Requestor type	University/Academic
Format	Print and electronic
Portion	Figure/table
Number of figures/tables	1
Original Wiley figure/table number(s)	figure 11
Will you be translating?	No
Title of your thesis / dissertation	MECHANOCHEMICAL INVESTIGATION OF A GLASSY EPOXY-AMINE THERMOSET SUBJECTED TO FATIGUE
Expected completion date	Dec 2014
Expected size (number of pages)	200

APPENDIX D

Defense and Permission



Inbox x



Stephen Foster <stephen.foster@eagles.usm.edu>
to Kfazen2 ▾

12/12/14 ☆



Kylee,

How are you doing? My defense data is January 20th right after Martin Luther King Day. I would like permission to reprint your photographs and depictions of the syringe pump injection molding setup. You do own the copyright according to USM.



Kylee Fazende <kfazen2@tigers.lsu.edu>
to me ▾

12/12/14 ☆





Hi Stephen!


You absolutely have permission to use whatever figures, photographs, etc you need to use from my thesis! I'll see you on January 20. Have a great Christmas!



Kylee

APPENDIX E

[Home](#) [Account Info](#) [Help](#)

**ACS Publications** Most Trusted. Most Cited. Most Read.

Title: Clarifying the Mechanism of the Denisov Cycle: How do Hindered Amine Light Stabilizers Protect Polymer Coatings from Photo-oxidative Degradation?

Author: Jennifer L. Hodgson, Michelle L. Coote

Publication: Macromolecules

Publisher: American Chemical Society

Date: May 1, 2010

Copyright © 2010, American Chemical Society

Logged in as:
Stephen Foster
Account #:
3000790658

[LOGOUT](#)

PERMISSION/LICENSE IS GRANTED FOR YOUR ORDER AT NO CHARGE

This type of permission/license, instead of the standard Terms & Conditions, is sent to you because no fee is being charged for your order. Please note the following:

- Permission is granted for your request in both print and electronic formats, and translations.
- If figures and/or tables were requested, they may be adapted or used in part.
- Please print this page for your records and send a copy of it to your publisher/graduate school.
- Appropriate credit for the requested material should be given as follows: "Reprinted (adapted) with permission from (COMPLETE REFERENCE CITATION). Copyright (YEAR) American Chemical Society." Insert appropriate information in place of the capitalized words.
- One-time permission is granted only for the use specified in your request. No additional uses are granted (such as derivative works or other editions). For any other uses, please submit a new request.

APPENDIX F

This Agreement between Stephen Foster ("You") and John Wiley and Sons ("John Wiley and Sons") consists of your license details and the terms and conditions provided by John Wiley and Sons and Copyright Clearance Center.

License Number	3532130656538
License date	Dec 18, 2014
Licensed Content Publisher	John Wiley and Sons
Licensed Content Publication	Journal of Polymer Science Part B: Polymer Physics
Licensed Content Title	Why is understanding glassy polymer mechanics so difficult?
Licensed Content Author	Robert S. Hoy
Licensed Content Date	May 23, 2011
Pages	6
Type of use	Dissertation/Thesis
Requestor type	University/Academic
Format	Print and electronic
Portion	Figure/table
Number of figures/tables	1
Original Wiley figure/table number(s)	Figure 1
Will you be translating?	No
Title of your thesis / dissertation	MECHANOCHEMICAL INVESTIGATION OF A GLASSY EPOXY-AMINE THERMOSET SUBJECTED TO FATIGUE
Expected completion date	Dec 2014
Expected size (number of pages)	200